WITS
UNIVERSITY

MAGNETOTRANSPORT PROPERTIES OF RARE EARTH ELEMENT MODIFIED CARBON NANOTUBES

Siphephile Ncube

A thesis submitted to the Faculty of Science, University of the Witwatersrand, Johannesburg, in fulfilment of the requirements for the degree of Doctor of Philosophy.

UNIVERSITY OF THE WITWATERSRAND
Johannesburg

Declaration

I declare that this thesis is my own unaided work. It is being submitted for the Degree of Doctor of Philosophy at the University of the Witwatersrand, Johannesburg. It has not been submitted before for any degree or examination in any other University.

_____
(Signature of candidate)

_____day of_____20___in_____.

Abstract

Functionalization and filling of carbon nanotubes has been tailored over years to modify the exceptional properties of the 1-dimensional (1D) conductor for magnetic properties based applications. Hence such a system exploits the spin and charge property of the electron, analogous to a quantum conductor coupled to magnetic impurities which poses an interesting scenario for the study of Kondo physics and related phenomena. A study of the low temperature electronic transport and magnetic properties of carbon nanotubes modified with gadolinium derivatives is presented in this thesis. The methods of modification used are chemical functionalization and capillary filling. The presence of gadolinium in the nanostructures extends the functionality of the nanotubes from conventional electronics to spintronics. Filled and functionalized multiwalled carbon nanotubes are characterized as well as filled double walled carbon nanotubes. This system gives a chance to study the interaction of a ballistic conductor with magnetic impurities.

Multiwalled carbon nanotubes functionalized with a gadolinium based supramolecular complex show enhanced magnetic properties and unexpected electronic behaviour that has not been observed in this material before. A newly developed synthesis technique has been employed for the synthesis and it is found that the functionalization method of the nanocomposite enhances the strength of magnetic interaction leading to a large effective moment of $15.79\,\mu_B$ and non-superparamagnetic behaviour unlike what has been previously reported. Saturating resistance at low temperatures is fitted with the numerical renormalization group formula verifying the Kondo effect for magnetic impurities on a metallic electron system. Magnetoresistance shows that devices fabricated from aligned gadolinium functionalized MWNTs exhibit spin-valve switching behaviour of up to 8%.

The electronic transport properties of MWNTs filled with $GdCl_3$ nanomagnets clearly shows the co-existence of Kondo correlation and cotunelling within the superparamagnetic limit. The Fermi liquid description of the Kondo effect and the interpolation scheme are fitted to the resistance-temperature dependence yielding the onset of the Kondo scattering temperature and a Kondo temperature for this nanocomposite, respectively. Cotunneling of conduction electrons inhibiting a Kondo type interaction has been verified from the exponential decay of the intensity of the fano shaped non zero bias anomalous conductance peaks which also show strong resonant features observed only in $GdCl_3$ filled MWNT devices. Hence these features are explained in terms of magnetic coherence and spin-flip effects along with the competition

between the Kondo effect and co-tunneling. The properties of doublewalled carbon naotubes filled with GdCl$_3$ are also presented. They show superparamagnetic behaviour and zero bias anomalies similar to what was observed in Gd filled MWNTs.

This work is the first on such lanthanide modified CNT hybrid bundle devices. The study raises a new possibility of tailoring magnetic interactions for spintronic applications in carbon nanotube systems. It highlights the possibility of enhancing magnetic interactions in carbon systems through chemical modification. Furthermore, the study demonstrates the rich physics that might be useful for developing spin-based quantum computing elements based on 1D channels.

Dedication

In memory of Robert and Zulu…

Acknowledgements

Table of Contents

Abbreviations and Formulae

0D	0 Dimensional
1D	1 Dimensional
2D	2 Dimensional
3D	3 Dimensional
AFM	Atomic Force Microscopy
AFM	Antiferromagnetic
CMOS	Complementary metal–oxide–semiconductor
CNT	Carbon nanotube
CVD	Chemical vapour deposition
DWNT	Double walled carbon nanotube
DEP	Di-electrophoresis
DRAM	Dynamic Random-Access Memory
DTPA	Diethylene triamine Penta acetic acid
Dy	Dysprosium
E_F	Fermi energy
EDX	Elemental Dispersive X-Ray spectroscopy
FC	Field cooled
FWHM	Full width half maximum
FM	Ferromagnet
FS	Ferromagnetic Semiconductors
FTIR	Fourier Transform Infrared Spectroscopy

Gd   Gadolinium

GdCl$_3$ Gadolinium trichloride

Gd – DTPA   Gadopentetic acid

Gd-Fctn-MWNT Gadolinium functionalized multiwalled carbon nanotubes

GMR   Giant magnetoresistance

Ho   Holmium

HRTEM   High Resolution Transmission Electron Microscopy

HDD   Hard Disk Drive

IBM   International Business Machines Corporation

IC   Integrated Circuit

ICP - OES   Inductively Coupled Plasma Optical Emission Spectrometry

IPA   Isopropanol

MFM   Magnetic force microscopy

MRI   Magnetic resonance imaging

MRAM   Magnetoresistive Random-Access Memory

MTJ   Molecular tunnel junction

MWNT   Multiwalled carbon nanotube

NFM   Non-Ferromagnetic

RAM   Random access memory

Oe   Oersted

PMMA   Poly(methyl methacrylate)

PLA   Pulsed laser ablation

RKKY   Ruderman, Kittel, Kasuya and Yoshida

SEM   Scanning Electron Microscopy

SMM	Single Molecular Magnet
SQUID	Superconducting Quantum Interference Device
STM	Scanning Tunnelling Microscopy
STS	Scanning Tunnelling Spectroscopy
SWNT	Single walled carbon nanotube
TFA	Triflouroacetic acid
TEM	Transmission Electron Microscopy
VTI	Variable Temperature Insert
ZFC	Zero Field Cooled
μ_B	Bohr Magneton
μ_{eff}	Effective magnetic moment

List of Figures

1. General Introduction

At the time of writing (2018), we are living in a digital age undergoing an intense technological revolution controlled by information technology and social networks. At the rate at which the technology is transitioning by 2020 we will practically be living in the technology. In the present time wearable technology is being introduced and chips can now be inserted into the human body for various functions. Just a decade ago it was very difficult to share information over continents but now information is shared in a fraction of a second via web broadcasts and large amount of this information can be stored in portable devices enabled by technological development.

'More than Moore" [**1**] has been the pushing factor in the nano-electronics industry for the past decades with scientists and engineers putting numerous efforts in proposing alternative materials and device concepts as alternatives for silicon based technologies which are fast approaching their physics limit [**2**] as the technological demands of the modern world areincreasing on a daily basis. To put it plainly researchers are looking for ways to build chips 'with sensational functions'. To date the electronics industry has been coping with the demands of technology for improved performance by shrinking the size of the integrated circuits (IC) currently at 5 nm [**3**] and smaller sizes are envisaged for the future. The electron spin can be exploited and utilized to meet some of the needs of technology like speed and low power consumption. The *International Technology Roadmap for Semiconductors* has identified the electron's spin as a new state variable which should be explored for use beyond CMOS. This requires the expertise of chemists and physicists to tailor device capability from synthesis to fabrication.

One of the main focus areas of technology is high performance computing and mobile devices with video cameras, where large volumes of information is created and stored. This is conceivable owing to the progress in the storage and memory technologies. In the 1980s hard disk drives (HDDs) with a capacity of 10 MB were sold for about USD 5300 and were out of reach for most people during the Apple and IBM PC era. Presently, HDDs with 12 TB capacity (a million times larger capacity) are available. The growth in the memory of the computer is close to a million-fold with the common computers having 8 GB random access memory (RAM) compared to the ones in the 1980s which had a memory of a few 100 kB. Even mobile

devices have a dynamic random-access memory (DRAM) capacity of about 4 GB, at the time of writing.

The thriving technologies in this generation, have built the Si (IC) industry and the data storage industry. For ICs, the quantity of transistors on a chip doubles about every 18 months adhering to Moore's law [4]. For magnetic hard disk drive technology, a typical desk-top computer drive today has a 40 GB per disk capacity, whereas in 1995 this capacity was 1GB per disk. Since 1991, the overall bit density on a magnetic head has increased at an annual rate of 60–100%. The integrated circuits operate by controlling the flow of carriers through the semiconductor by applied electric fields. The key parameter therefore is the charge on the electrons or holes. For the case of magnetic data storage, the key parameter is the spin of the electron, as spin can be thought of as the fundamental origin of magnetic moment [5]. Most electronic devices operate on the charge property of the electron which utilizes one degree of freedom. Spin originating from orbital magnetic moment of the electron [6] can also be utilized for charge transfer facilitating extended functions in contrast to conventional electronic devices [7].

This work focuses on the magneto-transport properties of magnetic nanoparticle modified carbon based nanomaterials, i.e., carbon nanotubes which are known to be good candidates for electronic transport [8] [9] [10] due to the high mobility of the electrons in these materials facilitated by their physical properties. A lot of research has been done on these pristine nanomaterials with functional electronic devices successfully fabricated [11] [12] but there is still room for improvement.

1.1. Background

Research in a new era of electronics called electron spin-based electronics, or 'spintronics", has a universal goal to develop applications for electron spin in a broad range of electronics and strives to produce low power consumption nanoscale devices [13] [14]. This is a new technology that emerged in the 1980s [15] [16] and recently gained lots of attention as Albert Fert and Peter Grünberg were awarded the Nobel prize in 2007 for their discovery of giant magnetoresistance (GMR) that has contributed immensely to the data storage industry. They discovered that it was possible to use electron spin to increase the rate at which information could be read from a hard disk drive and developed ground-breaking technology to harness this feature. Spin injection and efficient detection through semiconductors is an important initial step in the development of spintronic devices [14] [17] [18]. The primary goal of spin injection is to create a highly spin polarized population of electrons inside a semiconductor for study,

characterization, and manipulation. One of the pioneering experiments (1970) in spin polarization was on electrons tunneling from ferromagnetic metals through aluminium oxide into superconducting aluminium metal under an external magnetic field [18]. It was found than the spin polarization of the electrons was dependent on the orientation of the ferromagnetic contacts which could be controlled through an external magnetic field.

 The resistance in a typical nonmagnetic conductor is determined by how much the electrons scatter regardless of the spin of the electron. In a ferromagnetic conductor the electrons scatter dependent on the spin orientation; strongly for spin up and weakly for spin down. Conventional methodologies to utilizing spin are founded on the alignment of a spin relative to a reference [18] [20] (an applied magnetic field or magnetization orientation of a ferromagnetic material). The inherent devices function through electrical current which depends on the degree of the spin alignment. Major challenges in this field of spintronics that are addressed by experiment and theory include the optimization of electron spin lifetimes, the detection of spin coherence in nanoscale structures, transport of spin-polarized carriers across relevant length scales and heterointerfaces, and the manipulation of both electron and nuclear spins on sufficiently fast time scales [14] [18] [21] [22]. Recent advances in new materials engineering hold the promise of realizing spintronic devices soon [23] with magnetic material at the top of the list.

Carbon based spintronics [24] refers mainly to injection of spins and their transport through carbon nanomaterials and organic materials. Earlier studies involved the use of ferromagnetic electrodes for spin injection into carbon systems [25] [26]. Progress has been made over the past two decades on devices with local and non-local configurations [27] [28] along with utilization of highly sensitive characterization techniques [29] to study the spin transport properties of carbon nanomaterials in addition to theoretical studies [30]. CNTs possess remarkable electronic properties which can be translated to their composites offering great intellectual challenges and the potential for novel applications.

1.2.   Aims and Objectives

This research aims to build new hybrid carbon-based devices incorporating single molecular nanoscale magnets and a carbon system and to characterize their magnetotransport properties. CNTs modified using different techniques namely filling and functionalization are characterised in this work. The first experiment incorporates a single molecular magnet (SMM) onto multiwalled carbon nanotubes by chemical functionalization. The second incorporates nanomagnets into the CNTs by encapsulation/filling procedure. The success of the

nanocomposite is measured through the prominence of the SMM/nanomagnet properties at low temperatures. The desired composite possesses properties exhibiting spin polarized currents and other related phenomena which distinguishes the pristine CNTs from the modified one. This is investigated through the low temperature electronic transport properties of devices fabricated from magnetic nanoparticle modified CNTs. The complimentary magnetic properties of these devices are also studied in addition to the structural properties. This work will find application in the design of operable molecular spintronic devices using the quantum effects of individual SMMs. For this realisation the steps below are followed;

- CNT modification; functionalization and filling
- Structural characterization
- Magnetic characterization of the composite material
- Modified CNT composite device fabrication
- Device characterization (magnetic field dependent electronic transport)

1.3.   Motivation

As the size of the transistor and other components in electronic circuits is reduced further a lot of challenges have arisen, hence another quantum property of the electron known as spin can be explored for an additional degree of freedom. Electronic devices can be improved by making use of both the charge and the intrinsic spin of an electron to create what is known as spin-electronic better is known as spintronics devices [13] [14]. It utilizes the spin degree of freedom on traditional charge based electronic devices or the unaided spin based on the interaction of the charge carriers and the magnetic entities resulting in new and improved functionalities of electronic devices. The main differences between electronic and spintronic devices is summarized in Table 1-1. These devices have an advantage of providing conventional microelectronic device properties as well as an additional degree of freedom brought about by the presence of spin in the electron transport. This new generation of devices has the potential advantages of non-volatile charge transfer, increased data processing speed, reduced electric power consumption, and improved integration densities compared with typical semiconductor devices [31]. To successfully incorporate spins into existing semiconductor technology, one must resolve technical issues such as efficient injection, transport, control, manipulation and detection of spin polarization as well as spin-polarized currents. This can be achieved through selection of a 1D conductor like carbon nanotube, that possesses exceptional electron transport as well physical properties [32] that are retained in different environments, such that they can

be coupled to a spin polarizer and merged into a device with an architecture that supports maximum detection of spin polarized currents.

Table 1-1 Comparison of electronic and spintronic devices properties

Parameter	Electronic Devices	Spintronic devices
Basis	Based on charge properties of the electron	Based on intrinsic property spin of electron
Theory	Classical theory	Quantum theory
Operation	Controlled by an external electric field in modern electronic	Controlled by an external magnetic field
Materials	Conductors and semiconductors	Ferromagnetic materials
Bit (1 or 0)	Based on the number of charges and their energy	Two basic spin states spin up and spin down
Speed	Speed is limited	Based on direction of spin and spin relaxation, high speed
Power dissipation	High	Low

Progress in spintronics requires a deeper understanding of the basic spin interactions in solid state materials as well as the roles of dimensionality, defects, and semiconductor band structure in tailoring these dynamics. If the control of the spin degree of freedom in semiconductors, semiconductor heterostructures, and ferromagnets, can be understood, the possibilities for high-performance spin-based electronics will be endless. Hence in this work we are motivated to pursue a study of how the electronic transport properties of CNTs nanocomposite polarized by the presence of magnetic entities are generated and can be controlled and apply this towards the development of information technologies.

1.4.   Thesis outline

Chapter 1 is the general introduction to the study of magneto transport features in rare earth element modified carbon nanotubes giving a brief background, aims and objectives and a motivation for the study.

Chapter 2 is the literature review focusing on the electronic transport properties of carbon nanotubes and the move from electronics to spintronics. Additionally, the theory of magnetism at the nanoscale and related phenomena are discussed in the literature review as well as the rare earth elements with a focus on gadolinium.

Chapter 3 is the experimental section presenting a detailed synthesis technique of the gadolinium functionalized MWNT method and a brief description of the filling of MWNT with gadolinium. The device fabrication technique as well as the experimental facilities in the Nanoscale Transport Physics Laboratory which were utilized is this work are also presented.

Chapter 4 focuses on the magnetotransport features of gadolinium functionalized MWNT adapted from a manuscript that has been accepted for publication titled 'Kondo effect and enhanced magnetic properties in gadolinium functionalized carbon nanotube supramolecular complex'. A step by step investigation of the structural properties is followed to verify the successful functionalization of the nanomagnets onto the CNT surface and magnetic properties of the nanocomposite are presented. To study the electronic transport, differential conductance studies are carried out and as well as the magnetoresistance. The overall results are summarized to give a description of the magnetotransport studies of the MWNT functionalized with gadolinium nanomagnets.

Chapter 5 presents the magnetotransport features of MWNT filled with gadolinium chloride adapted from a paper that has been submitted for review titled, 'Observation of strong Kondo like features and co-tunnelling in superparamagnetic $GdCl_3$ filled 1D nanomagnets'. Structural characterization and a detailed electronic transport analysis are presented.

Chapter 6 is a presentation of the magnetotransport properties of $GdCl_3$ filled double walled NT (DWNT) which is subject to further analysis.

Chapter 7 is a discussion of the magnetotransport properties of Gd functionalized and Gd filled CNTs. It gives an overall view of the mechanisms involved and compares these properties.

Appendix A shows how the Variable Range Hopping model is not applicable to the observed electrical transport of gadolinium fuctionalized MWNTs.

Appendix B discusses the magnetic property control studies.

Appendix C presents a detailed description of the Numeriacl Renormalization Group formula calculation

Appendix D is additional measurement on the Gd-Filled MWNTs.

1.5. References

1   G.Q. Zhang and A. Roosmalen. More than Moore: Creating High Value Micro/Nanoelectronics Systems (1st ed.) Springer Publishing Company, Incorporated, 2009.

2   A.D. Franklin, M. Luisier, S. Han, G. Tulevski, C.M. Breslin, L. Gignac, M.S. Lundstrom and W. Haensch. Nano. Lett, 12, 758 (2012).

3   M.Irving. IBM's new 5nm architecture crams 30 billion transistors onto fingernail-sized chip. https://newatlas.com/ibm-5-nm-transistors-chip/49872/ (2017).

4   G.E. Moore. Cramming More Components onto Integrated Circuits, 38, 114 (1965).

5   J. Yamauchi. Fundamentals of Magnetism. In Nitroxides: Applications in Chemistry, Biomedicine and Materials Science. Wiley, 2008.

6   T. Shinjo. Nanomagnetism and Spintronics. Elsevier, 2014.

7   A. Hoffmann and S.D. Bader. Phys. Rev. Applied, 4, 047001 (2015).

8   E.A. Laird, F. Kuemmeth, G.A. Steele, K. Grove-Rasmussen, J. Nygård, K. Flensberg and L.P. Kouwenhoven. Rev. Mod. Phys, 87, 703 (2015).

9   A. Phaedon. Acc. Chem. Res, 35, 1026 (2002).

10   A. Phaedon, Z. Chen and V. Perebeinos. Nat. Nanotech, 10, 2, 605-615 (2007).

11   R. Seidel, A.P Graham, E. Unger, G.S. Duesberg, M. Liebau, W. Steinhoegl, F. Kreupl, W. Hoenlein and W. Pompe. Nano. Lett, 4, 831 (2004).

12   D. Zhang, K. Ryu, X. Liu, E. Polikarpov, J. Ly, M.E Tompson and C. Zhou. Nano. Lett, 6, 9, 1880 (2006).

13   A. Fert. Reviews of Modern Physics, 80, 1517 (2008).

14   S.A. Wolf, D.D. Awschalom, R.A. Buhrman, J.M. Daughton, S. von Molnár, M.L. Roukes, A.Y. Chtchelkanova and D.M. Treger. Science, 294, 1488 (2001).

15   M.N. Baibich, J.M.Broto, A.Fert. F.N. Nguyen Van Da, F. Petroff, P. Etienne, G. Creuzet, A. Friederich and J. Chazelas. Phys. Rev. Lett, 61, 2472 (1988).

16   G. Binash,.P. Grünberg. F. Saurenbach and W. Zinn. Phys. Rev, B, 39, 4828 (1989).

17   B.T. Jonker, O.M. J. van 't Erve, G. Kioseoglou, A.T. Hanbicki, C.H. Li, M. Holub, C. Awo-Affouda and P.E. Thompson. Silicon spintronics: Spin injection, manipulation and electrical detection. (2009 IEEE International Electron Devices Meeting (IEDM)).

18   D.D. Awschalom and M. E. Flatté. Nat. Phys, 3, 153 (2007).

19   R. Tedrow, P.M and Meservey. Phys. Rev. B, 7, 318 (1973).

20   L. You, R.C. Sousa, S. Bandiera, B. Rodmacq and B. Dieny. Appl. Phys. Lett, 17, 172411 (2012).

21   B.T. Jonker. Proceedings of the IEEE, 91, 727 (2003).

22   D.D. Awschalom, D. Loss and N. Samarth. Semiconductor spintronics and quantum computation. Springer Science & Business Media, 2013.

23   A. Hirohata, H. Sukegawa, H. Yanagihara, I. Zutic, T. Seki, S. Mizukami and R. Swaminathan. Magnetics, IEEE Transactions, 51, 1 (2015,).

24   Zhang, P. Chen and G. Science China Physics, Mechanics and Astronomy, 56, 207 (2013).

25   J. Maassen, W. Ji and H. Guo. Nano. Lett, 11, 151 (2010).

26   S. Gardelis, C.G. Smith, C.H.W. Barnes, E.H. Linfield and D.A Ritchie. Phys. Rev. B, 60, 7764 (1999).

27   L.X Xiaohua, C. Adelmann, S.A. Crooker, E.S. Garlid, J. Zhang, K.S.M. Reddy, S.D. Flexner, C. J. Palmstrøm, and P. A. Crowell. Nat. Phys, 3, 197 (2007).

28   N. Atodiresei, J. Brede, P. Lazić, V. Caciuc, G. Hoffmann, R. Wiesendanger and S. Blügel. Phys. Rev. Lett, 105, 066601 (2010).

29   T.W Odom, J.L- Huang, C.L. Cheung and C.M. Lieber. Science, 290, 1549 (2000).

30   L. Balents and R. Egger. Phys. Rev. Lett, 85, 3464 (2000).

31   G.H. Fecher and C. Felser and Spintronics: from materials to devices. Springer Science & Business Media (2013).

32   R. Saito, G. Dresselhaus and M.S. Dresselhaus. Physical properties of carbon nanotubes. Imperial College Press, (1998).

2.Literature review

2.1.   Carbon Nanotubes

Carbon nanotubes (CNTs) are hollow cylinders of carbon atoms with nanoscale dimensions which were discovered by Iijima in 1991 [1]. They can be thought of as graphene sheets seamlessly wrapped into cylindrical shells considered as one of the allotropes of carbon amongst diamond, graphite and fullerene [2]. There are three classes of CNTs namely single, double and multiwalled carbon nanotubes. They differ in the number of walls from one to multiple respectively determined by the synthesis method and conditions. Typical diameters are 0.4–2 nm for single walled (SWNTs), 2.5 to 3.5 nm double walled (DWNTs) and 10–100 nm for multiwalled (MWNTs) [3]. Due to their high aspect ratio arising from a very small diameter and micrometre length they possess very interesting physical, chemical properties and electronic properties.
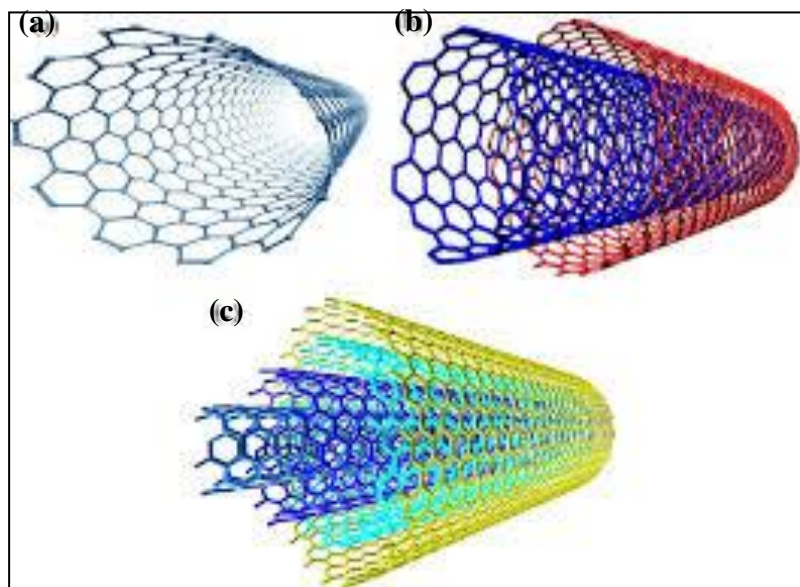
Figure 2-1 Different types of carbon nanotubes showing the seamless concentric cylinders with different number of layers namely (a) SWNT, (b) DWNT and (c) MWNT depending on the number of shells Image adapted from adapted from Exploration of Epoxy Resins, Hardening Systems, and Epoxy/Carbon Nanotube Composite Designed for High Performance Materials (2016).

2.2.   Synthesis techniques

CNTs can be synthesized using different methods as described below [**4**]. The choice of the synthesis technique usually depends on the intended application as the different methods give different CNT types and purity levels. Recently the synthesis has been improved to grow either semiconducting or metallic CNTs with a controlled chirality which was a long-standing challenge ever since the material was discovered [**5**]. Arc discharge was the first method used to produce CNTs [**1**] but later chemical vapour deposition (CVD) and pulsed laser ablation (PLA) were introduced.

2.2.1. Arc discharge

Arc discharge was the first technique used to produce MWNTs [**1**] and later SWNTs [**6**]. The experimental setup for arc discharge is shown in figure 2-2 along with the different CNTs types produced. In this technique two graphite electrodes of high purity are used as the anode and cathode. To produce CNTs the graphite electrodes are vaporized by passing a DC current (100 A) in the presence of an inert gas at low pressure, to produce soot at the cathode which is the CNTs. If pure graphite is used for the electrodes MWNTs are produced. Addition of a metal catalyst to the graphite electrodes results in the production of SWNTs. The quantity and quality such as lengths, diameters, purity etc of the nanotubes obtained depend on various parameters
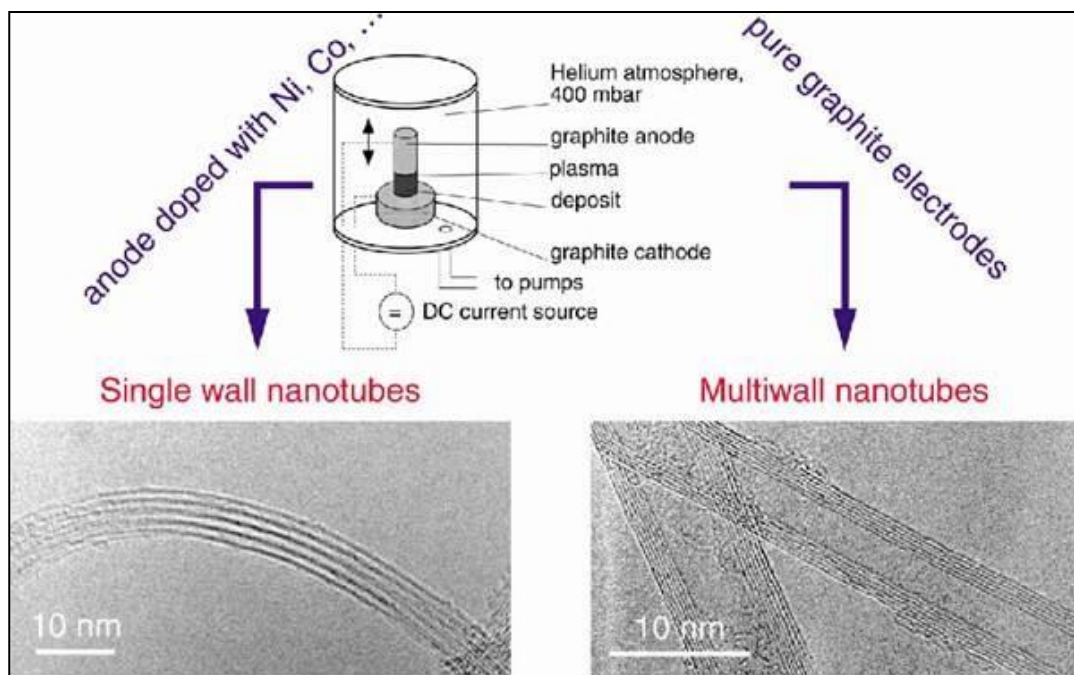
Figure 2-2 Arc discharge experimental setup and TEM images of resulting CNTs depending on the presence and absence of a catalyst.

Adapted from; http://kazuli.com/UW/4B/ME%20541/Nano%20Tubes.htm

11

such as the metal concentration, inert gas pressure, type of gas, plasma arc, temperature, the current and system geometry [**7**].

2.2.2. Pulsed Laser ablation

Pulsed laser ablation (PLA) discovered by Guo *et al* at Rice University [**8**] is a commonly used technique to synthesis SWNTs. It consists of a laser source (Nd:YAG laser), pulse generator, optics (prism and lens), I-CCD OES detector, mass flow controllers, inert gas carrier and a graphite target in a quartz tube within a furnace as shown in figure 2-3. The technique utilizes a laser beam to ablate a solid graphite target containing small amounts of metal catalyst at elevated temperatures (800 -1200 K). An inert carrier gas is used to mobilise the atomic plume from the point of ablation to the cold region where it condenses and then self assembles around the metal centre to form SWNTs [**9**]. Low defect (90% purity), highly crystalline SWNT can be grown through this method. The quality and quantity of SWNTs grown can be controlled by the choice and ratio of catalyst, gas flow rate, pressure, temperature, and laser parameters [**7**].
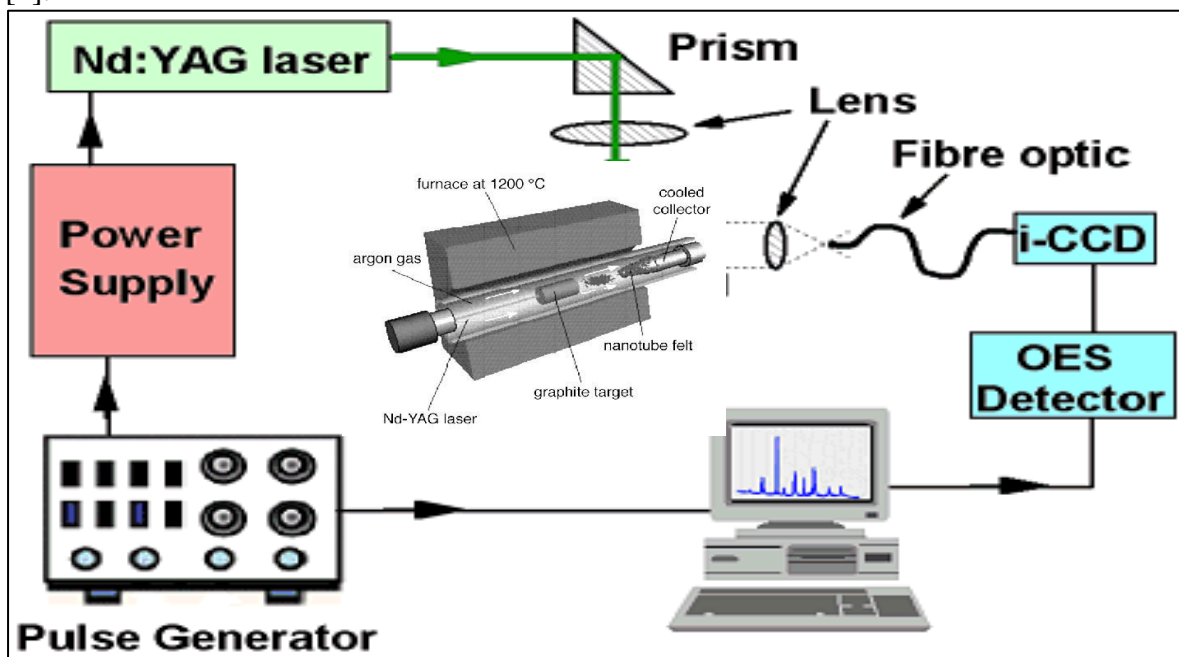
Figure 2-3 Pulsed laser ablation setup

2.2.3. Chemical vapour deposition

In principle, CVD is the catalytic decomposition of hydrocarbon feedstock with the aid of supported transition metal catalysts. CVD uses a precursor gas at lower temperatures in comparison to PLA temperatures (500 − 1100 K) to produce CNTs. It is the most versatile method for producing CNTs as it can be modified in many ways [**10**]. It consists of a furnace
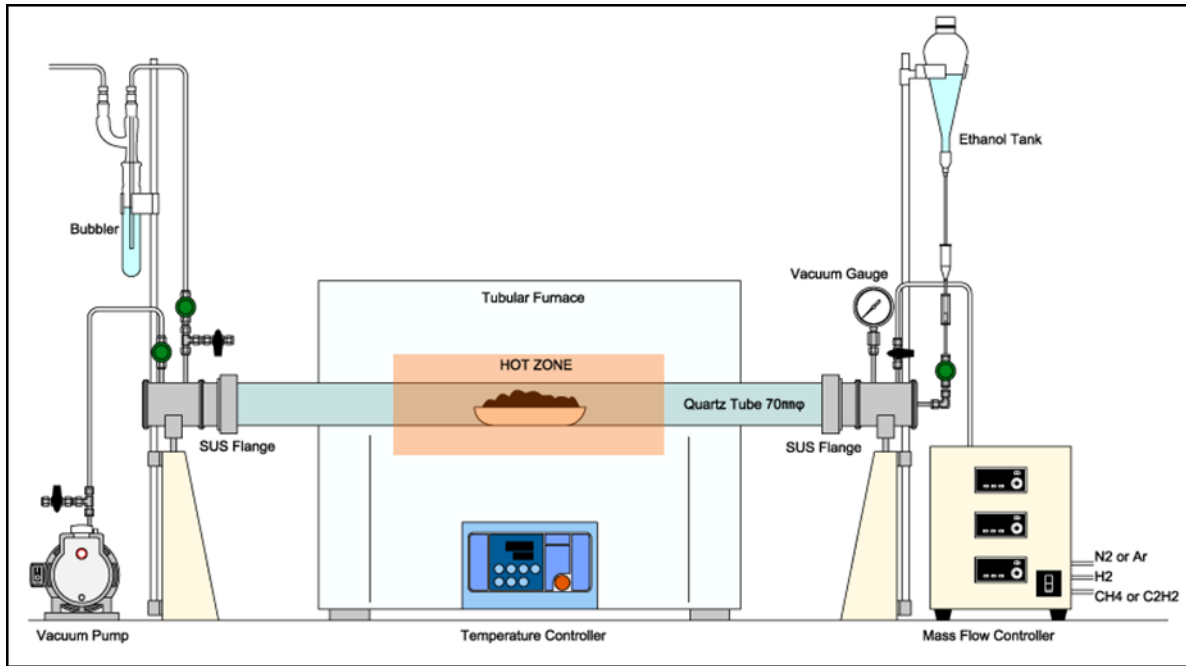
Figure 2-4 CVD setup

operating from 400 - < 1000 K, a temperature controller, mass flow controllers and quartz reaction tube as shown in figure 2-4. The gases one of which is carbon based; (ethylene, acetylene, methane) is broken down in an oven to form the CNTs. Pre-patterned substrates and can be used for growth of aligned CNTs where the size is determined by the diameter patterned catalysts as well as other methods. Most CVD processes produce MWNT and DWNT. The difference is determined by the catalyst used and the conditions of the reaction. SWNT can also be produced by CVD.

2.3.   Electronic Properties

As mentioned in Section 2.1, SWNTs can be regarded as a graphene sheet wrapped into a cylindrical shape. Due to their microscopic nature the electronic properties of SWNTs are determined by the way the graphene sheet is wrapped [11]. There are a number of ways in which the graphene sheet can be wrapped during the formation of SWNTs. The honeycomb lattice of graphene can be wrapped in an armchair, zigzag or chiral direction to determine the chirality of the resulting SWNT as shown in figure 2-5, depending on the primitive translation vector *n,m.* The chirality of the SWNTs determines its diameter hence its overall properties; electronic, optical and mechanical.

Hence SWNTs can be defined by their diameter and chirality given by,

$$C_h = n_1 a + n_2 b \qquad (2\text{-}1)$$

where (n_1, n_2) are the relative vectors of the pair of atoms on the graphene strip *a* and *b* are the unit vectors of the honeycomb lattice as shown in figure 2-5.

Figure 2-6 is a schematic representation of the electronic density of states (DOS) of (a) metallic and (b) semiconducting SWNTs which gives the number of available states for a given energy interval. For a 1D conductor the DOS is not a continuous energy function like in the 3D case, but it descends gradually and then increases in a series of discontinuous spikes known as Van Hove singularities (VHSs) as shown in figure 2-6. It is given by;

$$g(E)_{1D} = \frac{1}{\hbar\pi}\sqrt{\frac{m^*}{2(E-E_c)}} \qquad\qquad (2\text{-}2)$$

where the effective electron mass is given by m^* and E_c denotes the kinetic energy of the electron and E is the energy related to the system. Experimentally the DOS can be investigated using techniques like scanning tunnelling microscopy (STM) which probes the atomic structure through the electronic properties. Theoretically tight binding calculations can be used to model the electronic structure of CNTs [12] to come up with the DOS. The energy difference between
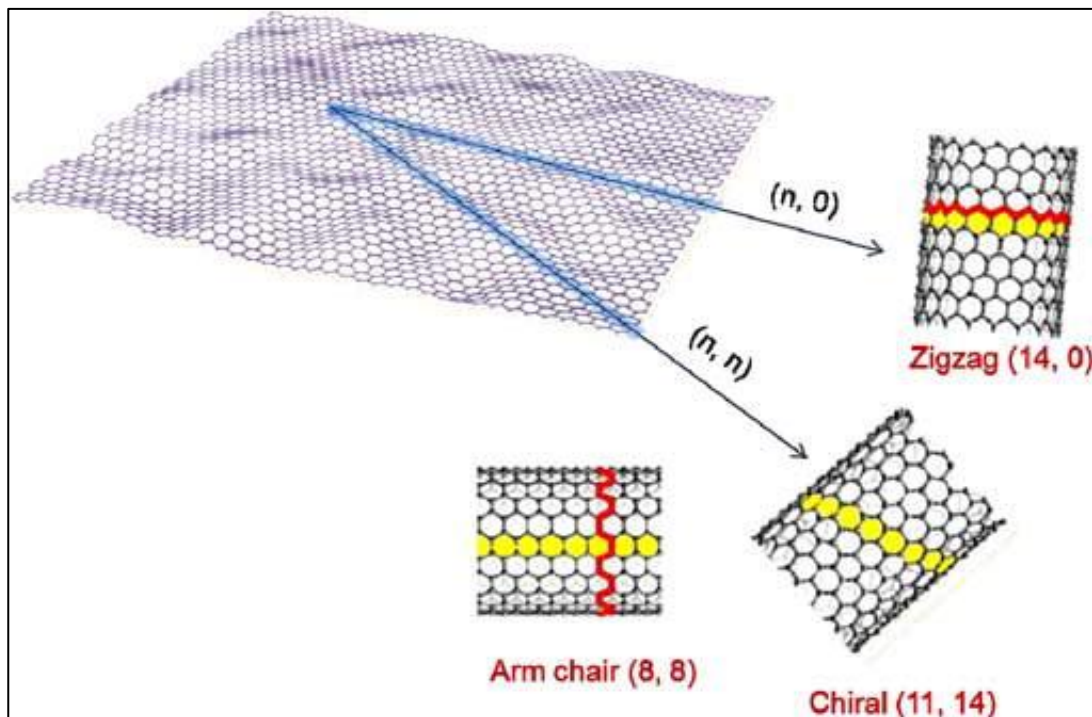
Figure 2-5 The honeycomb lattice of graphene. The way the graphene sheet is "rolled" determines the electronic properties of the resulting nanotube. Three different types of SWNTs can be formed, namely zigzag, armchair and chiral. Image adapted from adapted from Exploration of Epoxy Resins, Hardening Systems, and Epoxy/Carbon Nanotube Composite Designed for High Performance Materials (2016).

the peaks in the DOS of the VHS can be shown to first order to be related to the tube diameter based on the band folding approach
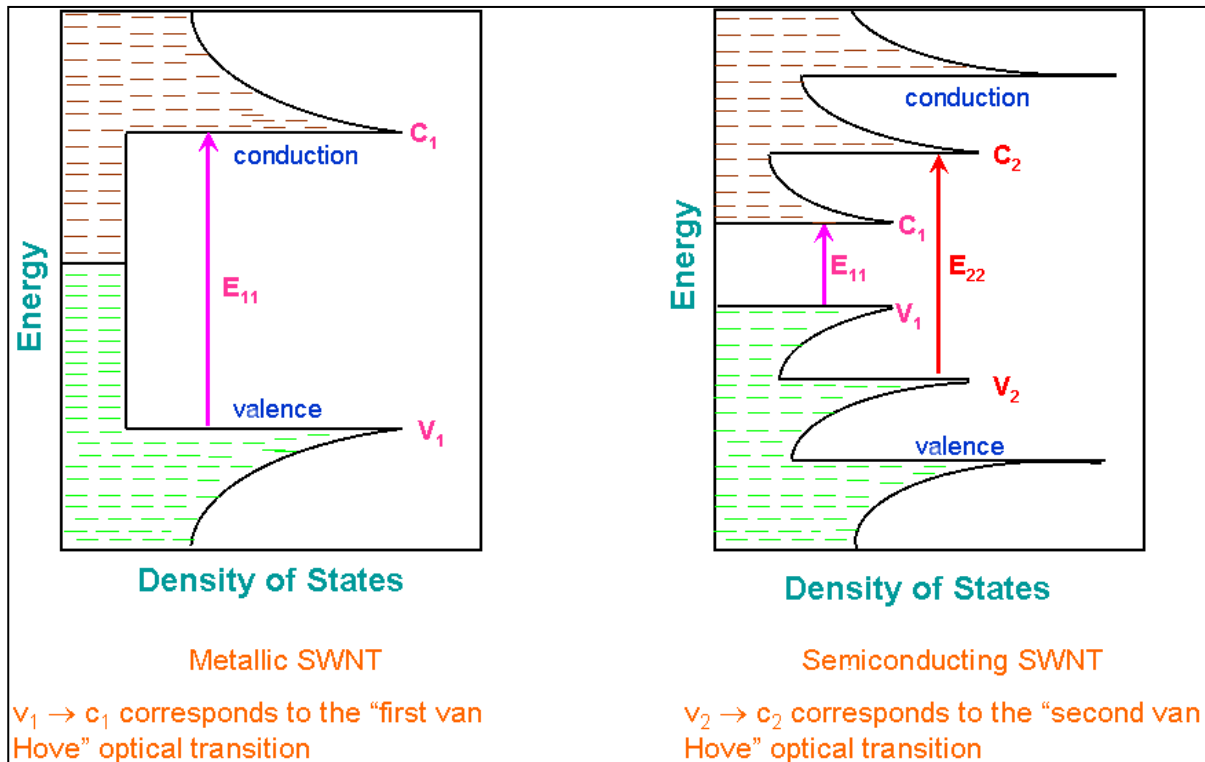
Figure 2-6 Schematic of the band structure and density of states of a metallic SWNTs carbon nanotube (left) and semiconducting SWNT. (Right).

2.3.1. Nanoscale electron transport

When the dimensions of a device are small enough for Ohm's law to be inapplicable then the device is referred to as a nanoscale/mesoscopic. The macroscopic performance of nanoscale devices depends mainly on the characteristics length scales of the electron carriers that prevail at low temperatures. The mesoscopic regime is defined by the quantum coherence of the one-electron wave-functions across the sample [13]. It is subjected to characteristic length scales relative to the motion of the electron.

The Fermi wavelength denoted by λ_F, is the electron wavelength at the Fermi energy which makes it the lowest wavelength present in a system. It is strongly dependent on the total number of electrons in a system. In the presence of an impurity the electrons tend to move away from or accumulate around the impurity causing its potential to disappear with respect to electron a distance away, a process known as screening. For impurities with a potential higher than $1/\lambda_F$ screening is not possible as λ_F is the shortest characteristic wavelength.

The mean free path denoted by λ_M, is the average distance that an electron travels before it loses it momentum due to boundary scattering. In metals, the mean free paths of electrons are

15

in the order of nm, while in pure semiconductors in the order of micron at mK temperatures. Below this scale, the electron transport becomes ballistic and classical concepts i.e. the diffuse motion of electrons will be no longer applicable. The third important length scale in mesoscopic electron transport is the phase relaxation length, denoted by λ_φ, defined as the average distance that an electron travels before it experiences inelastic scattering which destroys its initial coherent state. Typical scattering events, such as electron-phonon or electron-electron collisions, change the energy of the electron and randomize its quantum-mechanical phase. Impurity scattering may also contribute to phase relaxation if the impurity has an internal degree of freedom so that it can change its state. For example, magnetic impurities have an internal spin that fluctuates with times. The mesoscopic transport varies depending on which of the length scales mentioned above exceeds the device dimension as well as the conditions (temperature and magnetic field) the device is subjected to and the materials used.

The different length scales result in different regimes of electronic transport in semiconductor nanostructures. Ballistic transport regime occurs when scattering of the electron by impurities is negligible. This is possible when the dimensions of the sample are smaller than the electron mean free path, λ_M. In this regime only, the conductance is responsible for the electronic transport, not the conductivity as it is sample size independent. When the dimensions of the sample are larger than the mean free path, W, L>λ_M , where W and L are the width and length respectively, the electron enters the diffusive transport regime. The intermediate transport regime is called the quasi- ballistic, $W< \lambda_M < L$, when the boundary scattering, and internal impurity scattering are of equal importance.

2.3.2. Electronic transport properties of carbon nanotubes

CNTs are highly conductive materials. Studying their electronic transport properties gives an idea of their response to external probes for their potential integration into real devices. SWNTs are known to be quasi 1D crystals that display both ballistic and diffusive [**14**] transport properties depending on the helicity determined by synthesis method, purification, device architecture and other conditions that affect the overall defects. They can be either metallic or semiconducting depending on the band structure as shown in figure 2-6.

The electronic properties of individual SWNTs depend on which type is being characterized as they display both semiconducting and electronic transport conditions from synthesis of both types. Short low defect SWNTs behave like molecular wires which show ballistic conductance

16

[15]. At very low temperature they exhibit Coulomb blockade (CB) effects characterized by quantized conductance features which can be readily seen in gated structures. At higher temperatures the CB effects are overcome by thermal effects and the CNTs display power law dependencies like the Luttinger liquid behavior in the differential conductance [16]. Individual SWNTs show non-linear current voltage (*I-V*) characteristics on gated structures, where the current can be modulated through a gate source voltage.

SWNTs networks of varying thicknesses show a range of transport phenomena depending on the thickness consistent with the hopping conduction model. The thinnest SWNT network behaves like single semiconducting SWNTs, since generally from synthesis two thirds are semiconducting [9]. As the network gets thicker the Ohmic nature of the metallic SWNTs dominates the conductance which can be modelled by interrupted metallic behaviour [17]. Thermal fluctuation assisted tunneling is observed if the barrier length is thin. Very thick SWNT networks comprising a freestanding film exhibit more metallic behavior with *I-V* characteristics which are more linear without a gate-voltage effect which probably arises from zone boundary in-plane phonon scattering [18].

Individual MWNTs which consist of a number of concentric shells as shown in figure 2-1(c) are surprisingly more metallic than individual as well as a network of SWNTs at very low temperatures [19] but at higher temperatures there is no conversion to metallic temperature. This is consistent with a model of conduction that states that the transport of electrons is via the outer shells as the inter-shell transfer reduces the effects of quasi-1D-suppression of backscattering. The conduction is limited by fluctuation assisted tunneling in MWNTs.

2.3.3. Applications

CNTs have found diverse applications in different industries as shown in Figure 2-7 due to their exceptional 1D properties [20]. In electronics, they have been incorporated in functional circuits for transistors and conductive transparent thin films. They have also been used in biomedical application for drug delivery, manufacture of biosensors and cell cultivating. They are also used for probing the structures of nanostructure as tips of scanning probe microscopes. Electronic conductive paste in a resin can be produced for use in mechanical and aeronautical engineering where they are used as fibre reinforcement to steel. In chemistry they are used for water treatment and catalysis. In the energy sector they are incorporated into fuel cells and capacitors.
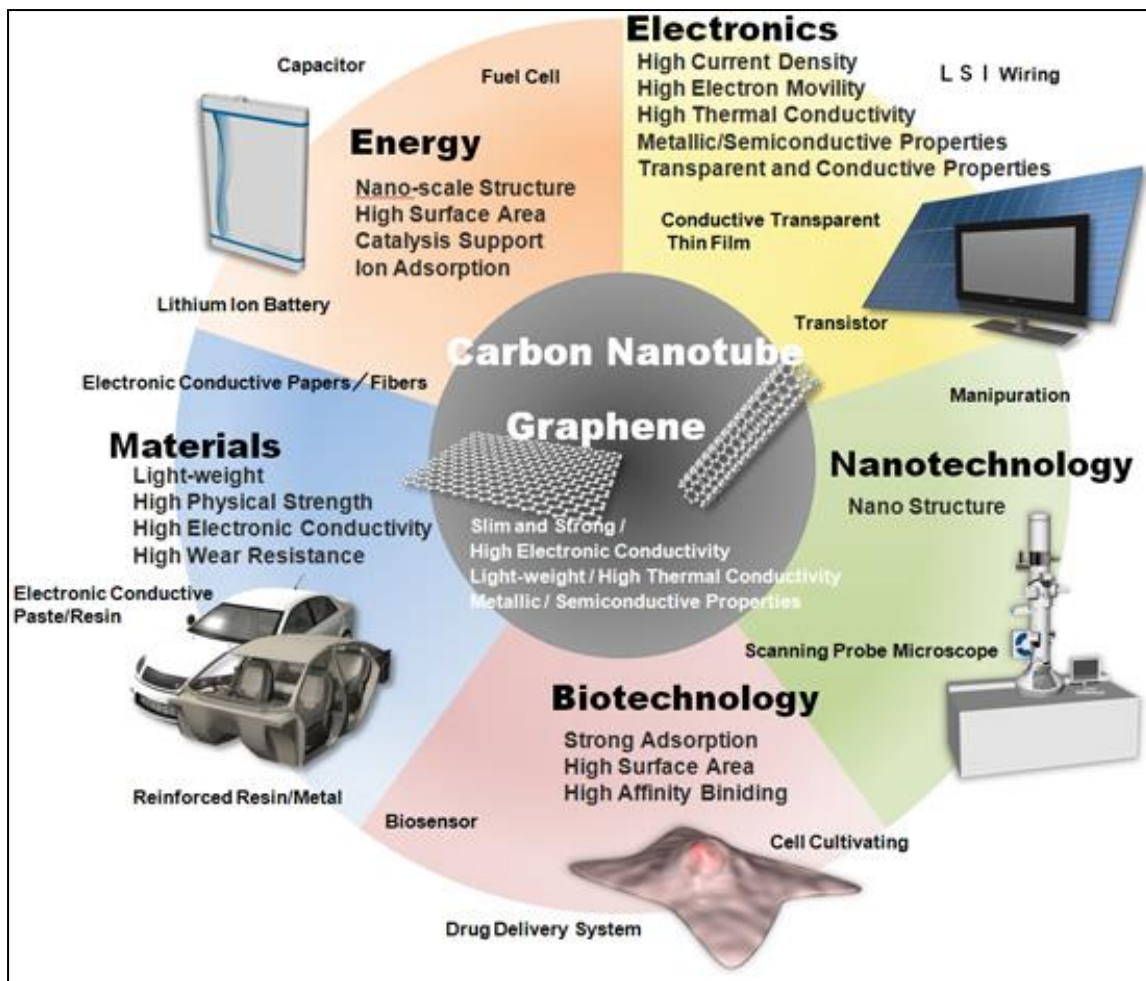
Figure 2-7 Diversity of the applications of CNTs ranging from Materials,, Biotechnology, Nanotechnology, Electronics and Energy. Image adapted from *http://www.meijo-nano.com/en/applications/use.html*

2.4.   Electronics to Spintronics

Spintronics is a new, fast emerging field of science and technology, which deals with relationships responsible for specific features of the spin interactions in metals, semiconductors doped with transition or rare-earth elements, and heterostructures that ensure unique properties of these materials. The word **spintronics** is a *portmanteau* coined from spin transport electronics. Spintronics is a field that has expanded into so many areas of industry with major applications in different fields and major technologies. In spintronics the intrinsic spin of the electron is utilized for charge conduction which brings about new capabilities and functions in electronic circuits [21]. It introduces another degree of freedom i.e spin control to the gate dependent current of the conventional transistor. Hence spintronics can be explored in materials that are ferromagnetic conductors [22]. The discovery in 1988 of the giant magnetoresistance

(GMR) is considered as the beginning of the new era of electronics; spintronics [**23**] [**24**] for the utilization of spin degree of freedom in magnetic nanostructures.

"An I.B.M. research fellow largely unknown outside a small fraternity of physicists, Mr. Parkin puttered for two years in a lab in the early 1990s, trying to find a way to commercialize an odd magnetic effect of quantum mechanics he had observed at super cold temperatures. With the help of a research assistant, he was able to manipulate the alignment of electronics to alter the magnetic state of tiny areas of a magnetic data storage disc, making it possible to store and retrieve information in a smaller amount of space. The huge increases in digital storage made possible by giant magneto-resistance, or GMR, made consumer audio and video iPods, as well as Google-style data centers, a reality" adapted from ref [**25**].

Stuart Parkin and his colleagues made a breakthrough that transformed the magnetic data storage industry when they discovered the "spin valve", a device with the ability to alter the magnetic state of materials at atomic level which resulted in a significant increase in the storage capacity. This discovery facilitated to pave the way for some of the currently trending devices and online applications. These huge increases in storage capacity enabled the development of giant data centers in the "cloud." Above all, the capability to store and access huge amounts of data in worldwide networks helped form the information-based world we live in today [**26**].

2.4.1. Spintronics timeline
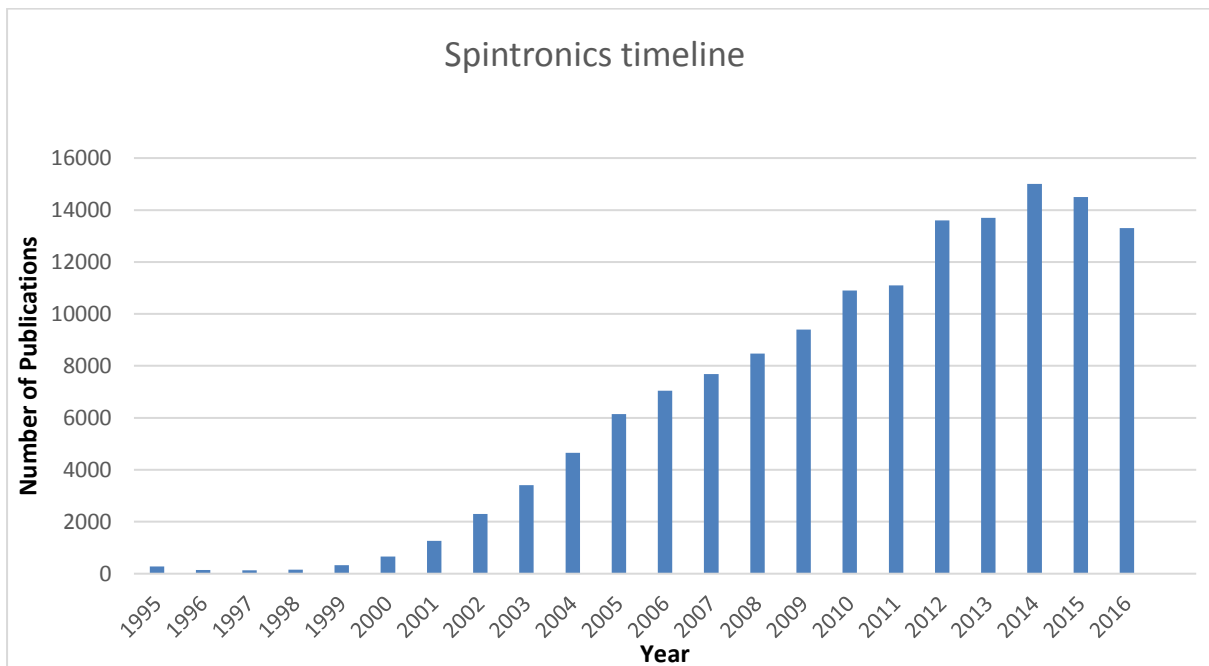
Figure 2-8 Timeline for spintronics showing how the research interests have grown over the years

The early 90s spintronic studies were pioneered on layered structures [27] [28],shown in figure 2-8 as most of the articles published durng this time were based on this material. The studies progressed to manganites, ferrites, diluted magnetic semiconductors and other related materials. Since 2007, after the discovery of the spin valve there has been a gradual increase in spintronics studies within the science community. Spintronics research rose significantly due to its application in read heads of HDDs. The high-density storage afforded by spintronics contributed immensely to the information technology industry which led to the HDD technology being extended to consumer electronics. The research done in the field of spintronics before the discovery of GMR explored some topics that only came into the limelight of spintronics recently like the spin Hall Effect (SHE) and quantum spin Hall Effect (QSHE) [29] [30]. From intensive research efforts other phenomena related to control and manipulation of spin polarized currents were unveiled. To date the field of spintronics is still expanding with other promising developments like the manipulation of magnetic moments and the generation of microwaves by spin transfer leading to single electron spintronics for quantum computing [31] as well as the invention of the spin transistor [32] .

In the past 22 years we have seen how spintronics has revolutionized the data storage industry in HDD technology which has been extended to mobile appliances like phones, tablets, video recorders, iPod and other appliances which have been extended to the automotive industry and the biomedical industry. The RAM of computers have reached sizes of 16 GB for the low end and 64 GB for the high-end devices due to advancements in data storage brought about by spintronics. This field of spintronics is still young and very promising for much bigger developments that will take us to a new era of electronics of low power high speed charge transfer.

2.5. Magnetism

Modern technology would be unthinkable without magnetic materials and magnetic phenomena [33]. It is a universal and generally an overlooked component of the technology supporting modern life. Magnetic materials, recording media, heads and sensors constitute a market worth over $30 billion per year. It should be stated at this point that magnetism at nanoscale is quite different from the magnetism macroscale which makes the study of magnetism at nanoscale is quite exciting for material scientists. Faraday was the first to classify the different magnetic orders that exist in solids as diamagnetic, paramagnetic or ferromagnetic, according to their response to a magnetic field. These magnetic properties are

mainly a result of the electrons in the atom, which possess a magnetic moment due to their motion. The nucleus similarly has a small magnetic moment, but it is inconsequential in comparison to that of the electrons, and it does not affect the overall magnetic properties.

One of the key resources for our day to day lives, electricity, is produced by the movement of conductors in a magnetic field. Magnetism is a property that is found all matter- it can even be found in vacuum. Basic elements of audio visual equipment, telephones, kitchen machines and the microwave oven are magnetic. Electrical consumer goods, which are operated through mechanical switches, customarily involve impermanent or permanent magnets. Powerful medical imaging depends on magnetic resonance. Magnetic sensors offer contactless monitoring of position or velocity. Mindboggling amounts of information are stored and retrieved from magnetic discs in (computers and servers throughout the world even some non-volatile memory is magnetic. Magnetic properties of a compound arise from the spin and orbital angular momentum of the electrons specific to a compound. The different magnetic properties are discussed in the sections that follow.

2.5.1. Giant Magnetoresistance effect

Like other magnetoresistive effects, GMR is the change in electrical resistance in response to an applied magnetic field. It is a quantum mechanical effect in thin films effect observed in thin film structures composed of alternating ferromagnetic and nonmagnetic layers.as shown in figure 2-9. It was discovered in the late 1980s by Peter Gruenberg and Albert Fert [23] [24]. It originates from the spin dependent electronic transport inherent to magnetic metal systems. It is understood by using the Mott model which was proposed to understand the increase in resistivity of ferromagnetic metal above its Curie temperature [34]. It assumed the electrons in a magnetic metal traverse in two independent channels coinciding to spin up and spin down states hence the conduction occurs in parallel within two spin channels. The second assumption is that the electron scattering for the spin up and spin down is independent so that the DOS at the Fermi level is not the same. Hence the resistivities are different for electrons with different spins as shown in figure 2-9. Hence by using Mott's argument the GMR is explained by stating that electrons with a spin anti-parallel to the external **B** field are strongly scattered and weak for electrons with a spin parallel to the applied field **B** which results in a low and high resistance corresponding to the scattering rates respectively as shown in figure 2-9. There are different types of GMR effects namely multilayer, spin valve, pseudo-spin and granular. The magnetic layers are separated by very thin (few nm) insulating layers in GMR devices. The GMR effect
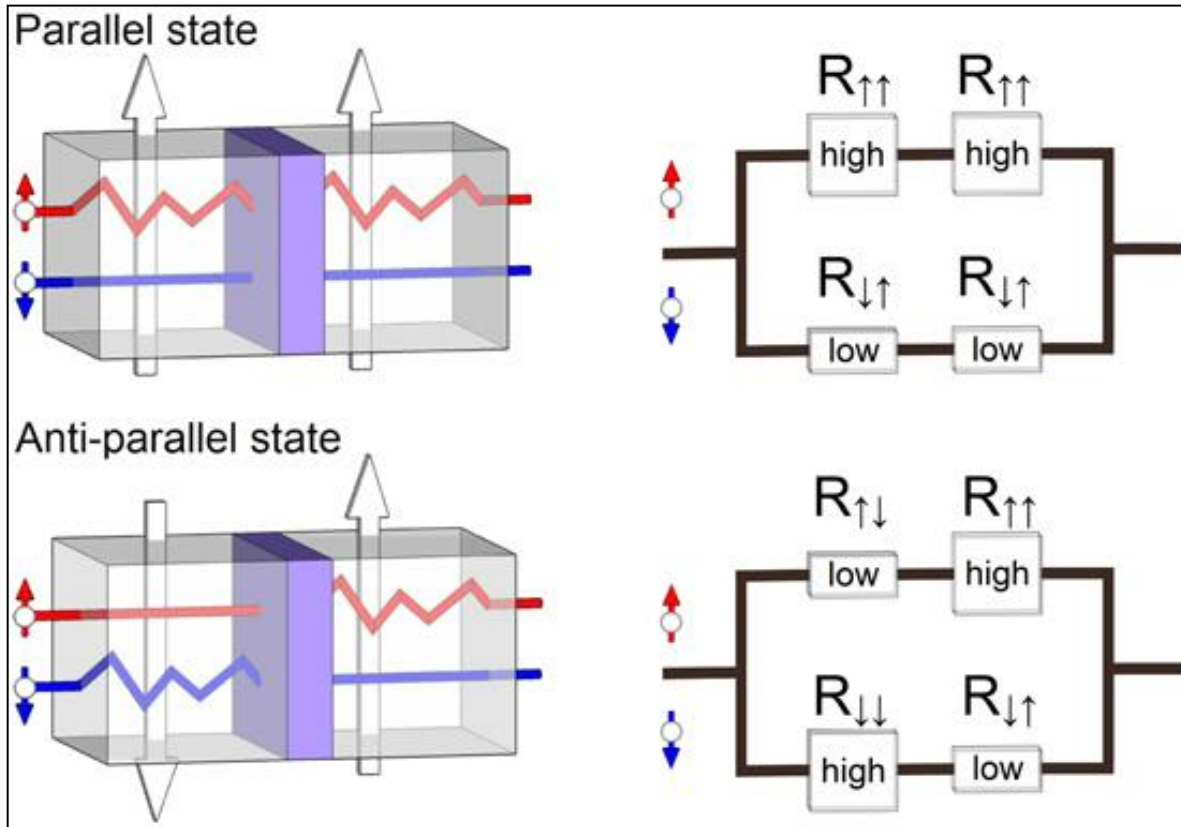
Figure 2-9 Schematic representation of the Giant magnetoresistance effect

is used mainly for the development of HDDs along with magneto-resistive random-access memory (MRAM).

2.5.2. Tunnelling magnetoresistance effect

Tunneling magnetoresistance (TMR) is defined as a change in the electrical resistance of a magnetic tunnel junction (MTJ) due to an external magnetic field. A MTJ consists of two magnetic metals which are the electrodes separated by a nonmagnetic barrier metal as shown in figure 2-10. TMR occurs when the magnetization in the respective electrodes changes between the parallel and anti-parallel state. It depends strongly on the choice of electrode and barrier metal in addition to fabrication technique which determines the quality of the interface formed. Over the years TMR has been interpreted in terms of the Bardeen's approach [**35**] of tunnelling as being driven by overlap of wavefunctions penetrating the barrier with the electrodes with a small transmission probability. An application of Bardeen's model to TMR yields the Julliere's model given by;

$$TMR = \frac{G_P - G_{AP}}{G_{AP}} = \frac{2G_p G_{AP}}{1 - G_p G_{AP}} \qquad (2\text{-}3)$$

where G_P and G_{AP} are the conductance's of the parallel and antiparallel states. The TMR is defined as the ratio between the differences in the conductance of the parallel an anti-parallel
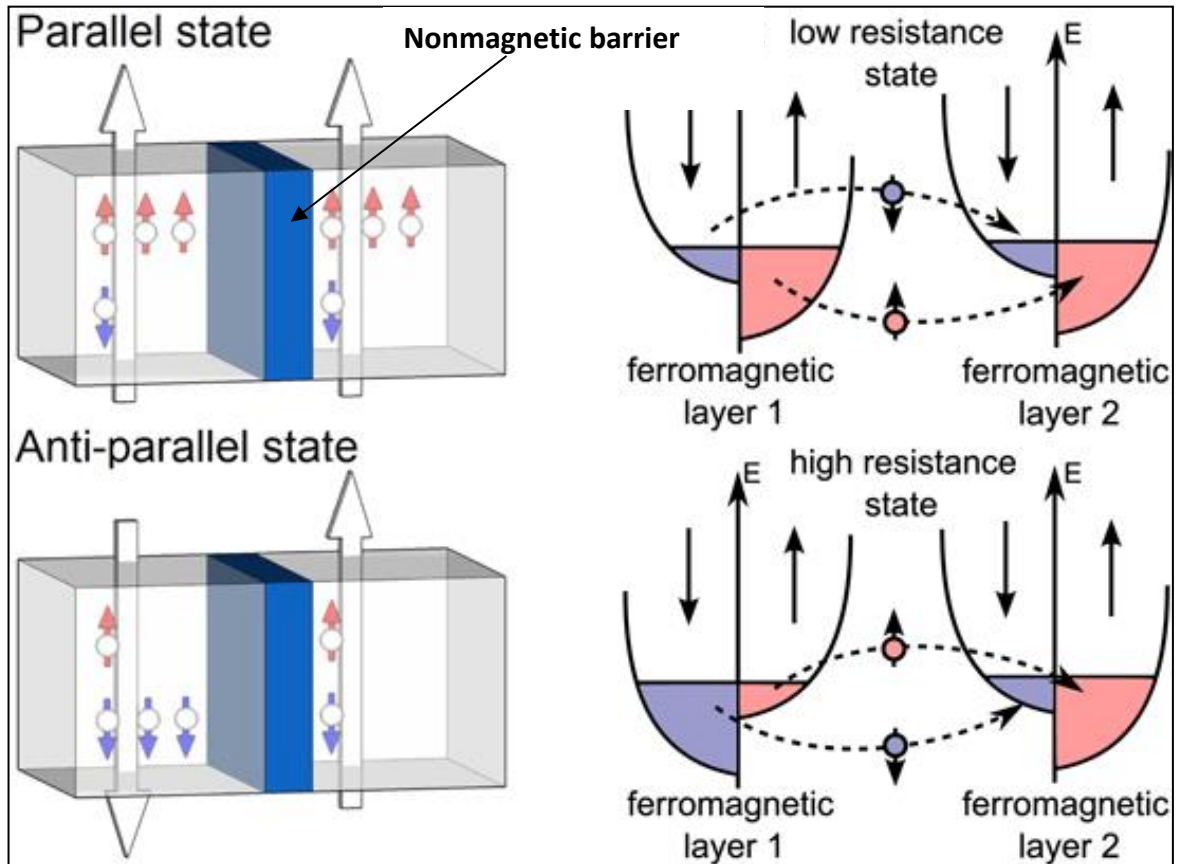
Figure 2-10 Schematic representation of the tunnel magneto resistance effect

state normalized by the anti-parallel conductance. Assuming the tunnelling of spin up and down processes are two independent processes and the matrix elements are the same for all single particle states.

2.5.3. Magnetic Susceptibility

Susceptibility is defined as the measure of the propensity of a material to be magnetized when placed in a magnetic field. The susceptibility arises due to the interactions of electrons and nuclei with the externally applied magnetic field, B and with each other. Susceptibility is given by a symbol, χ. If permeability of a material is ignored. It signifies how sensitive a material is to the applied magnetic field and it can be given per unit mass or volume of sample, if either quantity is known. Using SI units, the magnetic induction **B** is related to **H** the magnetic field intensity by amd M is the magnetization.

$$\bar{B} = \mu_0(\bar{H} + \overline{M}),$$

where μ_0 is the vacuum permeability and $1 + \chi_v$ is the relative permeability of the material. Thus the volume magnetic susceptibility χ_v and the magnetic permeability μ are related by the following formula:

$$\mu = \mu_0 (1 + \chi_v)$$

There are two other measures of susceptibility namely the mass susceptibility and molar susceptibility given by

$$\chi_{mass} = \frac{\chi_v}{\rho}$$

$$\chi_{mol} = M\chi_{mass} = M\frac{\chi_v}{\rho} \qquad (2\text{-}4)$$

Solid state NMR can also be scaled to give a susceptibility. SQUID and nuclear magneto resonance (in solution) techniques can be used to measure the susceptibility. The inverse susceptibility is used to determine the exchange interaction for the material. It is related through the Curie Weiss law given by,

$$\chi = \frac{C}{T - T_c} \qquad (2\text{-}5)$$

Where C is a constant known as the Curie constant and T_c is a constant with the units of temperature read off from the x-intercept of the inverse susceptibility curve. Exchange interaction usually occurs in clusters and infinite clusters resulting in ferromagnetism, antiferromagnetism or ferrimagnetism depending on the relative orientation of the individual spins. The effective magnetic moment m of an ion can be calculated if the g factor and the J value are known using the equation below.

$$m = g\mu_B \left(\sqrt{J(J + 1)}\right) \qquad (2\text{-}6)$$

2.5.4. Ferromagnetism

Ferromagnetism is the most striking phenomena of magnetism which is demonstrated in the spontaneous magnetization of atoms in materials such as iron (Fe), nickel (Ni), cobalt (Co) and magnetite (FeO_4). This natural magnetization results from the parallel alignment of the magnetic moments of the individual atoms as shown in figure 2-11. In 1906 Pierre Weiss made significant progress in understanding ferromagnetism and hypothesized a theory known as the molecular field [36] leading to the Curie Weiss law that most paramagnets also obey given by;

$$\chi(T \gg T_c) = \frac{C}{T - T_c} \qquad (2\text{-}7)$$

According to the Weiss theory ferromagnetism is instigated by a prevailing molecular field that aligns the magnetic moments known as exchange forces. It is this exchange force that makes ferromagnetism present in some metals and absent in others. In the susceptibility curve the ferromagnet is typified by a Curie temperature T_c as shown in the equation 2-7. All ferromagnetic substances become paramagnetic above their Curie temperatures. In an ideal FM the spins are completely polarized with a correlation length $\rightarrow \infty$, where the χ is temperature independent and the m is B field independent in a simple FM.
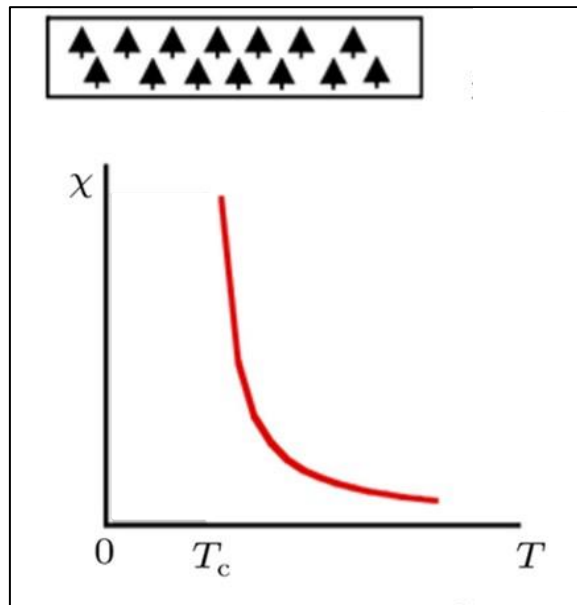
Figure 2-11 Demonstration of the alignment of spins in a ferromagnetic substance and the resulting susceptibility curve

2.5.5. Antiferromagnetism

$$\chi(T \gg T_N) = \frac{C}{T + T_c} \qquad\qquad (2\text{-}8)$$
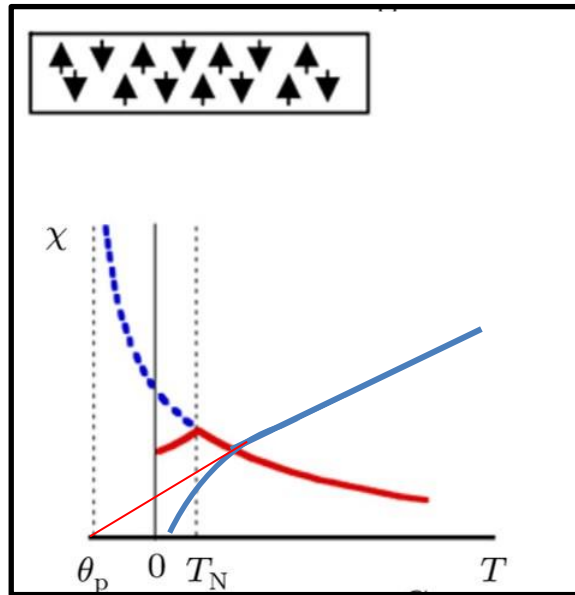
Figure 2-2-12 Demonstration of the alignment of spins in an antiferromagnetic substance and the resulting susceptibility curve

The magnetic moments (dipoles) are called antiferromagnetic if the arrangement of the atomic sublattices is in an antiparallel manner i.e. opposite direction as shown in figure 2-12. In the susceptibility curve the antiferromagnetic transition is typified by the Neel temperature, T_N [37]. Most antiferromagnetic substances do not obey the Curie Weiss law. At sufficiently large magnetic fields an antiferromagnet can be changed into a ferromagnet, known as a metamagnetic transition. An antiferromagnetic exchange interaction is given by a negative weiss temperature T_c, in the inverse susceptibility curve. Antiferromagnetism plays a crucial role in the GMR effect.

2.5.6. Para-magnetism
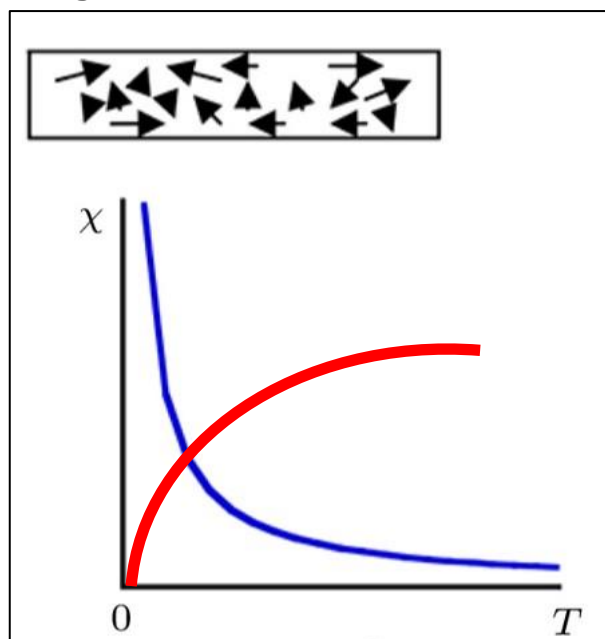
Figure 2-13 Demonstration of the paramagnetic effect and the corresponding magnetic susceptibility curve

Paramagnetism arises due to the presence of unpaired spins in a substance as shown in figure 2-12 is characteristic of atoms with incompletely filled atomic orbitals. They are characterized by randomly oriented dipoles that do not interact in the absence of B field. When a field is applied the dipoles align with the B field resulting in net magnetic moment. Most elements with incomplete shells like the transition metal (excluding Fe, Ni and Co) and rare earth elements exhibit this sort of magnetic behaviour at ambient conditions arising from a large net magnetic moment. The paramagnetic elements usually obey the Curie law given by;

$$\chi = \frac{C}{T} \qquad (2\text{-}10)$$

or the Curie Weiss law with small values of T_c. The rare earth elements are strongly paramagnetic and the effective moment (μ_{eff}) varies with the atomic number with dysprosium (Dy) having a value of 10.6 Bohr Magneton (μ_B). Paramagnetism is also observed in ferromagnetic substances above the T_c and antiferromagnetic substances above their Neel's temperature.

2.5.7. Superparamagnetism

Superparamagnetism is a form of magnetism which appears in small ferromagnetic or ferrimagnetic nanoparticles. In sufficiently small nanoparticles, magnetization can randomly flip direction under the influence of temperature. The typical time between two flips is called

the Neel relaxation time. In the absence of an external magnetic field, when the time used to measure the magnetization of the nanoparticles is much longer than the Neel relaxation time, their average value of magnetization appears to be zero: they are said to be in the superparamagnetic state. In this state, an external magnetic field can magnetize the nanoparticles, similar to a paramagnet. However, their magnetic susceptibility is much larger than that of paramagnets. It is different from this standard transition since it occurs below the Curie temperature of the material. Superparamagnetism occurs in nanoparticles which are single domain, i.e., composed of a single magnetic domain. This is possible when their diameter is below 3–50 nm, depending on the materials. In this condition, it is considered that the magnetization of the nanoparticles is a single giant magnetic moment, the sum of all the individual magnetic moments carried by the atoms of the nanoparticle.

2.5.8. Diamagnetism

Diamagnetic substances contain no unpaired electrons and possesses no net magnetic moment. The atoms are magnetically polarized in a direction opposite the applied magnetic field and repelled. It was first presented by the French physicist Paul Langevin [36]. Most gases, and covalent and ionic solvents are diamagnetic as well as superconductors under certain conditions. For diamagnetic substances the mass susceptibility is not dependent on the temperature and converges to zero at low temperatures.

2.5.9. Exchange mechanisms
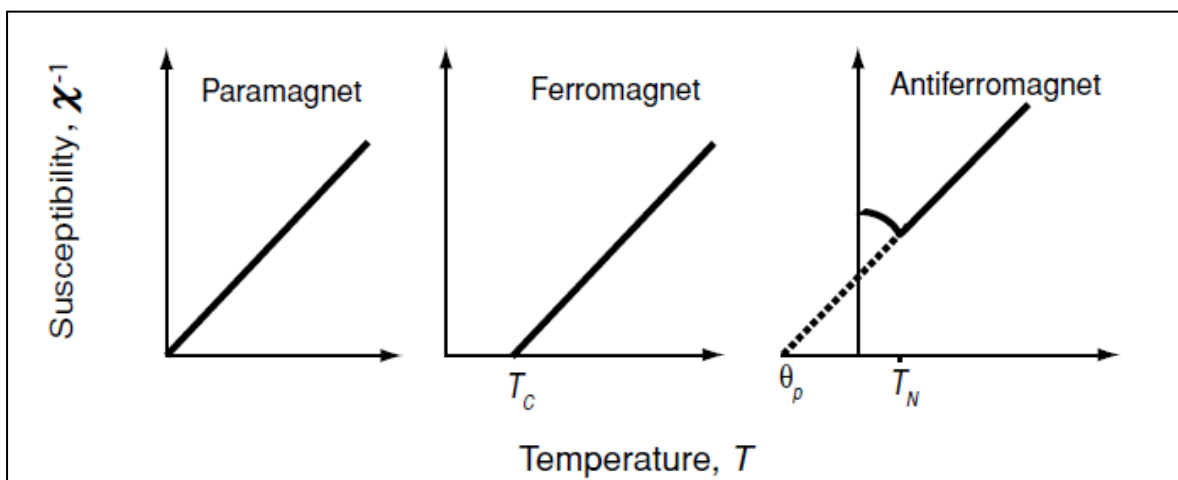
Figure 2-14 Inverse susceptibility plots shown for the different types of magnetism inferring to the exchange mechanism.

Exchange interactions are an example of long range ordering in magnetic systems. The inverse susceptibility gives the characteristic exchange mechanism for a paramagnetic substance. Exchange between neighbouring dipoles occurs if there is sufficient energy causing ferromagnetic or antiferromagnetic interaction depending on whether the dipoles are aligned or misaligned respectively. A pure paramagnet with no net interaction will intercept at 0 K. For a ferromagnetic interaction the T_c is positive given by an intercept more than zero. For an antiferromagnetic the exchange interaction is negative given by a negative $T_c(\theta_P)$.

2.5.10.   Electrical Spin Injection and Spin Transport

The extensive range of spin-dependent phenomena in semiconductor systems entails reliable and proficient techniques for electrical injection of strongly spin polarized currents in the direction opposite to the magnetic field, in addition to electrical detection of such spin currents [38].This detection could conceivably ensue either within the semiconductor or upon the current generated from the semiconductor system, depending on the device design. Consequently, efforts of electrical spin injection and detection following the proposal of Datta-Das transistor [39], have concentrated on developing devices that can assimilate spintronics within the current semiconductor (SC) technology. For practical applications it is unquestionably extremely desirable that the generation, injection, and detection of the spin currents be realised needing the use of small magnetic fields and that these practices be applicable at or above room temperature. The use of ferromagnetic (FM) metallic electrodes appears to be fundamental in a lot of real-world all-electrical spin-based devices until other ferromagnetic-semiconductor (FS) configurations can be explored [21].

2.5.11.   Ohmic injection

In a FM metal the electrical conductivity of the majority spin (↑) deviates considerably from that of the minority spin (↓) resulting from a spin-polarized electric current. Creation of an Ohmic contact is the most straightforward technique to achieve spin injection between a FM and a semiconductor, consequential to a spin-polarized current in the conductor. However, spin flip scattering and diminished polarization results from characteristic metal-semiconductor Ohmic contacts that are fabricated from heavily doping a semiconductor surface.

Subsequent to previous studies [40] of diffusive spin transport [41], the fundamental problem in Ohmic spin injection across ideal FM-non-ferromagnet (NFM) interfaces is that the efficiency of the spin injection is subject to the ratio of the spin dependent conductivities of the ferromagnetic and non-ferromagnetic electrodes. For efficient and substantial spin injection to

occur the NFM electrode has to be preferably a metal, if it is a semiconductor the spin injection is not efficient. Hence for diffusive spin transport the conduction electrons through the ferromagnet should be almost 100% spin polarized to achieve efficient spin injection. An approach that may overcome this problem of spin injection in the Ohmic contact experiments is the change in orientation of the ferromagnetic electrodes as suggested in the work done in [42].

2.5.12.　　Tunnel injection.

An STM vacuum tunnelling process has been successfully used to inject spin into a semiconductor with a ferromagnetic tip [43]. It has been suggested that tunnelling injection is more effective than Ohmic injection due to the observation of conservation of spin polarization during tunnelling from FM-insulator-FM tunnel junctions with high magnetoresistance. Quantitative advances in the understanding of the proposed usefulness of the tunnel junction have been made from the theoretical work by Rashba [44] and Flatte and co-workers [45]. The transport across an interface is determined by a spin dependent DOS of the electrodes involved in the tunnelling process provided the impedance of a barrier at the interface is high enough. Hence the current through the barrier is then sufficiently small for the electrodes to remain in equilibrium and the relative (spin-dependent) conductivities of the electrodes play no substantial role in defining or limiting the spin-dependent transport across the interface.

2.5.13.　　Ballistic electron injection.

The ballistic regime is the alternative way for tunnel injection is spin injection across FS interfaces, where the difference between the two-spin conduction subbands of the FM metal and the conduction band of the semiconductor determine the spin-dependent interfacial ballistic electron transmission probability. The ballistic transmission and reflection probabilities of the interface are determined using the assumption that the transverse momentum of an incident electron is conserved [46]. The other assumption is that once a spin-polarized electron goes into the semiconductor electrode, the probability that it will be elastically scattered back into the ferromagnetic injector is very low. Transport through the semiconductor region is completely ballistic if the design of the device comprises, the spin-dependent capture of an injected carrier by another ferromagnetic electrode. For specifically efficient spin injection, a 3D ballistic point contact between a ferromagnet and a semiconductor should be effective [47].

2.5.14.   Hot electron injection.

An additional spin injection technique involves the use of spin-polarized "hot" electrons having energies that are much greater than E_F by tunnel-injecting electrons into a ferromagnetic layer at energies E_F [48]. As the majority-spin and minority-spin electrons have much different inelastic mean free paths, hot electron passage through, for example, a 3-nm Co layer, is sufficient to result in a ballistic electron current that is more than 90% polarized. This highly polarized hot-electron current can then continue to an underlying metal semiconductor interface where a portion of the beam will enter the semiconductor, with the transmission probability being determined by energy and momentum constraints imposed by the band structure difference between the semiconductor and metal at the interface. If there is no substantial spin-flip scattering at the interface, then the ballistic electron current entering the semiconductor will be also very highly polarized (.90%) and the injection energy, relative to the bottom of the semiconductor conduction band, tunable through the tunnel injection bias. The disadvantage of hot electron injection is that the overall efficiency is low.

2.5.15.   Spin detection

The most obvious approach to the electrical detection of spin populations in semiconductors is to use the spin dependent transport properties of semiconductor-ferromagnet interfaces. Experimental efforts with this spin-valve detection scheme have used Ohmic contacts for the spin collection electrode. But the same difficulties discussed above apply to spin collection, and it appears that for effective spin collection/detection, either a ballistic contact or a tunneling contact from the semiconductor to a ferromagnet will be required. If, however, for reasons of signal-to-noise, an efficient spin dependent extraction of the injected spin polarized current is required, then the tunnel barrier has to be sufficiently thin that (spin dependent) tunneling transport into the ferromagnetic electrode is more probable than spin relaxation within the semiconductor [44]. An alternative spin detection technique is a potentiometric measurement, with a ferromagnetic electrode, of the chemical potential of the nonequilibrium spin populations [49]. With respect to the complete spin transistor device, an extensive analysis by Tang et al. has concluded that only for the case of ballistic transport throughout the device structure will the desired, electrical field-tunable spin precession be detectable as polarized electrons transit through the semiconductor region. Moreover, they conclude, in accord with the initial suggestion of Datta and Das [50], that a very narrow, single- or few-electron channel device structure will be required.

2.5.16. Spin transport

Of interest to the spin transport theory in semiconductor systems has been the question as to whether quasi-independent electron model can adequately account for the experimental results, or whether many-body, or correlated-electron processes are important. Flatte et al. [45] have extensively examined this issue in the diffusive transport regime and have concluded that an independent electron approach is quite capable of explaining measurements of spin lifetimes, particularly the room temperature measurements. Sham and colleagues [51] have been focusing on the very low temperature regime where collective electron processes may well be important in determining the spin relaxation rates and spin lifetimes, although experimental results in this regime are quite limited. On the device front, Flatte and Vignale [52] have considered the possibility of constructing unipolar electronic devices by using ferromagnetic semiconductor materials with variable magnetization directions. They have shown that such devices should behave very similarly to p-n diodes and bipolar transistors and suggest that they could be applicable for magnetic sensing, memory, and logic.

2.5.17. Spin transfer

Spin transfer describes the process by which the orientation of the magnetic layer in a MTJ or spin valve can be modified using a spin polarized current. Experiments have demonstrated that if a spin-polarized current passes from a thick fixed ferromagnetic layer, through a nonmagnetic layer, to another thin film "free" nanomagnet by spin dependent scattering of the polarized current an angular momentum can be transferred to this layer [53] which can be used to excite oscillations in the nanomagnet [54]. In the absence of a strong external magnetic field, this spin-dependent scattering can also result in the reversal of the orientation of the magnetic moment of the free nanomagnet with the final orientation relative to the fixed layer being dependent on the direction of the current flow. This "spin-transfer" process opens up the possibility of new nanoscale devices for memory and other spin electronics applications. One application, in addition to direct current addressable magnetic memory, might be the use of spin transfer to excite a uniform spin wave in a nanomagnet and then to use this nanomagnet as a precessing spin filter to inject a coherent spin pulse into a semiconductor structure.

2.6. Kondo Effect

The word 'Kondo' means battle in Swahili. In correlated electron physics the Kondo effect is a standard model in correlated electron physics that describes the scattering of conduction electrons due to the presence of magnetic impurities resulting in a characteristic change in the

electrical resistance with temperature as shown in figure 2-15 (a) [**55**]. For normal metals the scattering of conduction electrons is reduced at low temperature resulting from a reduction in electron phonon scattering, consequently electrons propagate with less back scattering thereby lowering the resistance to a residual value as shown in Figure 2-15 (blue line) or it can become superconducting at low temperatures (green line). It was first described by Jun Kondo using the perturbation theory for dilute magnetic alloys where he hypothesized that the scattering rate of the magnetic impurity should diverge as temperature approaches absolute zero [**56**]. This is caused by the conduction electrons which tend to align their spins opposite to that of to that of a nearby impurity. At low temperatures the electron propagation is deviated by a magnetic impurity which consequently flips its spin and deflects its pathway. The delocalized electrons pair with the local electron to form a state of total spin zero: a singlet which is the cause of the dramatic change in the resistance as the temperature decreases in contrast to a decrease in resistance in pure metals at low temperatures (figure 2-15(a &b)). The temperature T_K, at which the resistance begins to decrease or saturate is called Kondo temperature. Hence in essence a battle ensues when a magnetic impurity is placed in nonmagnetic metal. The Kondo temperature is energy scale limiting the validity of the Kondo results.

The Kondo effect depends on the properties of the magnetic impurity and the nonmagnetic host and both are affected by the size of the sample and the nonmagnetic random scattering events. Hence, the Kondo effect was refined using non-perturbative theories adopted from the Anderson model and the Wilson renormalization theory that describe magnetic impurity as a single quantum state for an electron bound to a local site [**57**]. At low temperatures and low energies the interaction between the itinerant electrons and the localized magnetic impurity becomes non-perturbatively strong, a condition known as asymptotic freedom. The Anderson model describes localized f-electrons that hybridize with different itinerant electrons given by the Hamiltonian (**H**) that follows;

$$H = \overbrace{\sum_{k,\sigma} \epsilon_k \, n_{k\sigma} + \sum_{k,\sigma} V(\boldsymbol{k}) \left[c_{k\sigma}^\dagger f_\sigma + f_\sigma^\dagger c_{k\sigma} \right]}^{H_{resonance}} + \underbrace{E_{fnf} + U_{nf\uparrow nf\downarrow}}_{H_{atomic}} \qquad (2\text{-}11)$$

The virtual-bound state resonance line width is defined by

$$\Delta = \pi \sum_k |(\boldsymbol{k})|^2 \delta(\epsilon_k - \boldsymbol{\mu} = \pi V^2 p) \qquad (2\text{-}12)$$
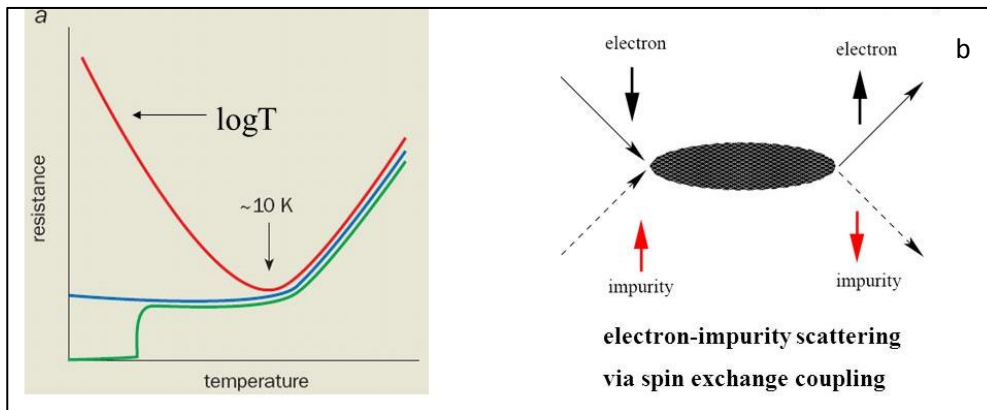
Figure 2-15 (a) Resistance-Temperature variation for a typical magnetic impurity in a metal traditional Kondo system. At low temperatures the spin scattering off the impurities enhances the resistance (red line) Blue line is a typical metal and green a superconducting metal.. Adapted from [55] (b) Demonstration of electron impurity-scattering via spin exchange [56].
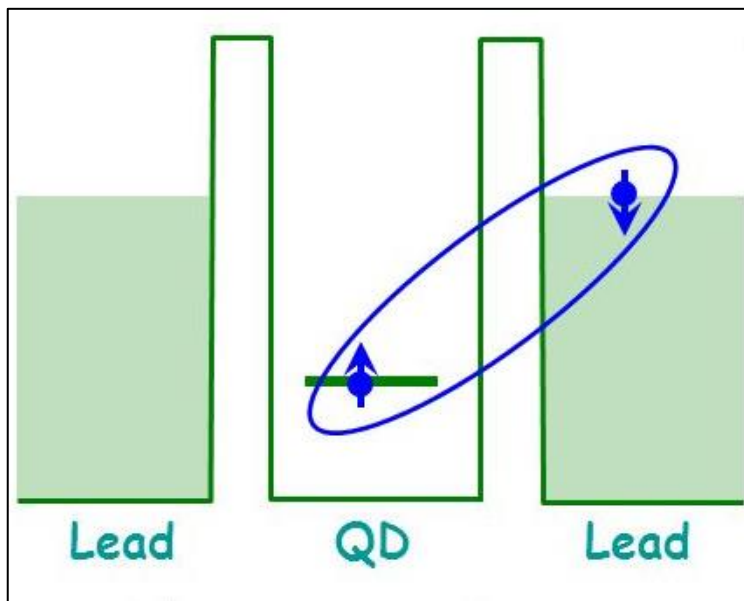
Figure 2-16 Demonstration of the Kondo effect in a 0D quantum dot system connected to electrodes which arises when an unpaired spin from the quantum dot is paired to an itinerant electron to form a Kondo system

Where the first term of the **H** is related to the itinerant electrons. The second term to the spin flipping events between the localized f electron and the itinerant electrons. The last two terms give the energy modes for the localized f electrons and consider the coulomb repulsion respectively. Δ is an expression for the full width half maximum resonances from the first two terms of the **H**.

There are two approaches of the Anderson model, the atomic picture that considers the tune hybridization picture and the adiabatic picture that considers the tune interaction strength. The discrepancy between the two pictures is resolved by considering tunnelling of local moments between spin up and spin down.

Kondo's phenomenological model was shown to emerge from Anderson's more microscopic one: the spin of delocalized electrons is opposite to that of the local electrons due to tunneling of electrons on and off the local site. It is observed not only in metals with magnetic impurities, but also in quantum point contacts. The change in resistance can be probed in greater detail in a gate-defined quantum dot nanostructures [55] [58]. More generally, Kondo effect need not involve the screening of a localized spin, but rather the screening of any localized degeneracy as the effect has also been observed when an even number of electrons occupy a quantum dot, at a singlet-triplet degeneracy [59]. The quantum dot with at least one unpaired electron is analogous to the traditional Kondo system of the magnetic impurity in a metal. It behaves as a magnetic impurity, and when the dot is coupled to a metallic conduction band, the itinerant electrons can scatter off the dot as illustrated in figure 2-16. It has also been proposed that a topological Kondo effect can be found in Majorana fermions [60] as well as quantum simulations and ultracold atoms.

2.6.1. Associated Phenomena RKKY interaction

In a rare earth metal or in atoms with magnetic alloys in a nonmagnetic host, Ruderman, Kittel, Kasuya and Yosida (RKKY) showed that a single magnetic impurity generates a nonuniform, oscillating spin polarization in the conduction band which falls off as r^{-3} [36]. This spin
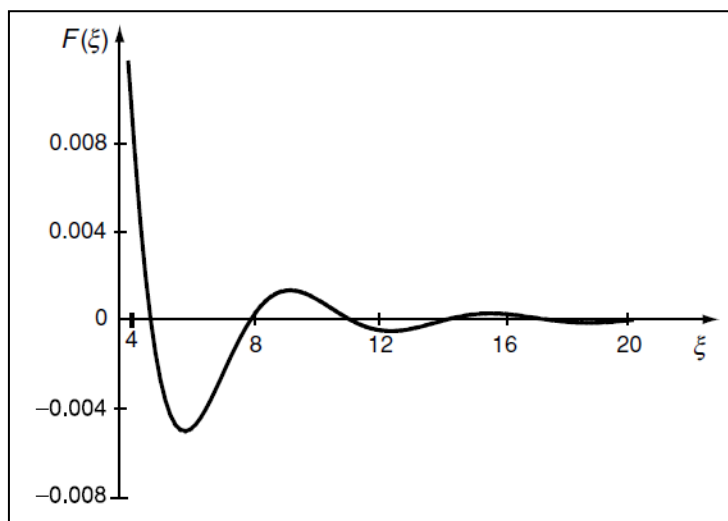
Figure 2-17 RKKY interaction schematic showing how it arises as a function of F(ξ}

polarization is related to the Friedel oscillations of charge density around the impurity which have wavelength, π/kF. The magnetic atoms are too far apart to interact directly, but they interact through the conduction electrons. The conduction electrons are spin polarized by the magnetic ions and due to their delocalization, they transfer their polarization to a nearby magnetic ion. The resulting interaction between the magnetic ions can be either ferro-antiferromagnetic depending on the distance between the magnetic ions. It leads to long-range oscillatory coupling between core spins as shown in figure 2-17 as a function of ξ.

. For free electrons, the polarization is proportional to the RKKY function

$$F(\xi) = (sin\xi - \xi cos\xi)/\xi^4 \qquad (2\text{-}13)$$

where $\xi = 2k_F\, r$, k_F being the Fermi wavevector. This oscillating spin polarization results from the different potential seen by the spin up ↑ and spin down ↓ conduction electrons at the local moment site. The RKKY interaction in the low-electron-density limit is equivalent to the s–d model which refers to coupling of the conduction electrons to the spins in a metal, with a ferromagnetic coupling. Analogous oscillatory exchange is found in ferromagnetic multilayers with nonmagnetic spacer layers. Among the rare-earth metals, only gadolinium has S as a good quantum number. The others have J as their quantum number, yet the exchange interaction couples the spins.

2.7.　　New Materials for spintronic Applications

The search for material combining properties of a ferromagnet and the semiconductor has been a long-standing goal but an elusive one because of differences in crystal structure and chemical bonding. The advantages is their potential as spin-polarized carrier sources and easy integration into semiconductor devices. The ideal FS would have Curie temperatures above room temperature and would be able to incorporate not only p-type, but also n-type dopants. The Eu chalcogenides, the most thoroughly studied early magnetic semiconductors, in which the magnetic species resides on every lattice site, failed in the practical sense, because their ferromagnetic transition temperatures, T_c, were much lower than room temperature with little hope of great improvement.

The discovery of ferromagnetic order temperatures as high as 110 K in III-V− based diluted magnetic semiconductors (DMS) (alloys in which some atoms are randomly replaced by magnetic atoms, such as Mn 21) has generated much attention. There are theoretical predictions

for T_c's above room temperature in several classes of these materials. And the discovery of electronically controlled magnetism was recently reported. To achieve large spin polarization in semiconductors, the Zeeman splitting of the conduction (valence) band must be greater than the Fermi energy, E_F, of the electrons (holes). In materials doped with high concentrated magnetic materials, this occurs easily because the net magnetization upon ordering is proportional to the concentration of magnetic species.

2.8.   The Rare earth elements

Table 2-1 Calculated and measured values of the effective moments for the rare earth elements free ions

Element	Configuration	$g\sqrt{J(J+1)}$	m/μ_B
La	$4f_0 5s_2 5p_6$	0	0
Ce^{3+}	$4f_1 5s_2 5p_6$	2.54	2.3 - 2.5
Pr^{3+}	$4f_2 5s_2 5p_6$	3.58	3.5
Nd^{3+}	$4f_3 5s_2 5p_6$	3.62	3.5
Pm^{3+}	$4f_4 5s_2 5p_6$	2.68	
Sm^{3+}	$4f_5 5s_2 5p_6$	0.84	1.5
Eu^{3+}	$4f_6 5s_2 5p_6$	0.00	3.4
Gd^{3+}	$4f_7 5s_2 5p_6$	7.94	8.0
Tb^{3+}	$4f_8 5s_2 5p_6$	9.72	9.5
Dy^{3+}	$4f_9 5s_2 5p_6$	10.63	10.6
Ho^{3+}	$4f_{10} 5s_2 5p_6$	10.60	10.4
Er^{3+}	$4f_{11} 5s_2 5p_6$	9.59	9.5
Tm^{3+}	$4f_{12} 5s_2 5p_6$	7.57	7.3
Yb^{3+}	$4f_{13} 5s_2 5p_6$	4.54	4.5

There are 15 rare earth elements ranging from Lathanum ([57]La) to Lutetium ([72]Lu). Chemically the rare earths are very similar due to the almost identical arrangement of the outer electrons. The number of the electrons in the 4f shells varies from 0 - 14 from La[57] to Lu[72] which determines the magnetic properties of the individual elements. The spin orbit coupling in rare

earth materials is very strong since rare earth elements are heavy (large number of un unpaired electrons in the f orbital); once magnetized a large magnetic field must be applied to demagnetize and reverse the field.

They are all paramagnetic at room temperature and above due to spin unbalance i.e incomplete filling of inner 4f shells. The 4f shells are located deep within the atom consequently they are shielded from the crystalline electric field hence the orbital moment is not quenched. This results in a large net magnetic moment due to the noncancellation of the spin and net spin components. These elements obey the Curie Weiss law with large T_c values due to the large magnetic moments per ion resulting in an interaction between adjacent ions. At low temperatures they are have a complex magnetic behaviour, mostly ferromagnetic. It is worth mentioning that their counterpart transition metals also have a complex magnetic behaviour. They show ferromagnetism (Fe, Ni, Co), antiferromagnetism (Cr, Mn) and the rest are either diamagnetic or paramagnetic. The rare earths possess very high effective moments compared to Fe (which is the strongest transition metal element) but due to their high atomic number their saturation magnetization are comparable to that of Fe.

2.8.1. Gadolinium Properties
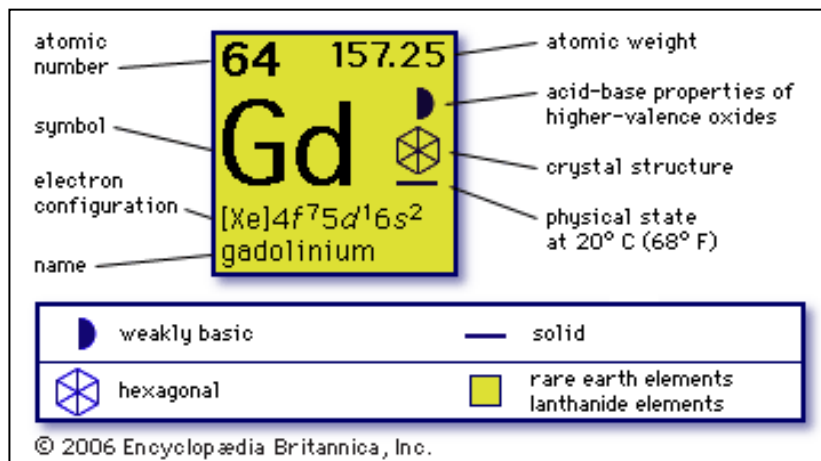
Figure 2-18 Structure and properties of gadolinium (Gd) showing that it is a weakly basic solid with a hexagonal structure

Gadolinium (Gd) was named after the Finnish chemist Johan Gadolin (1760-1852) who discovered it in Sweden in 1787. Figure 2-18 is an overall description of the properties of Gd. At room temperature, gadolinium is solid and crystallizes in the hexagonal, close-packed alpha form. It is considered as a heavy rare earth element with atomic number 64 and an atomic mass of 157.25 a.u. It consists of seven unpaired electrons in the 4f shell with parallel spins and

usually found in the form of Gd^{3+} ion. Its electronic ground state has effective moment, $\mu_{eff} = 7.94\ \mu B$. Most of the rare earth elements become ferromagnetic at very low temperatures but Gd becomes ferromagnetic just below room temperature i.e its Curie temperature is 289 K. Its counterpart in the transition element group Fe is ferromagnetic with highest $\mu_{eff} = 3.15\ \mu B$. The difference is explained by the band theory of magnetism.

References

1   S. Iijima. Nature, **56**, 354, (1991).

2   A. Hirsch. Nat. Mat, **9**, 868 (2010).

3   M.S. Dresselhaus, A. Jorio, M. Hofmann, G. Dresselhaus and R. Saito. Nano Lett, **10**, 751 (2010).

4   J. Prasek, J. Drbohlavova, J. Chomoucka, J. Hubalek, O. Jasek, V. Adam and R. Kizek. J. Mater. Chem, **21**, 5872 (2011).

5   B. Liu, F. Wu, H. Gui, M. Zhengand and C. Zhou. ACS Nano, **11**, 31 (2017).

6   S. Iijima and T. Ichihashi. Nature, **363**, 603 (1993).

7   R. Das, Z. Shahnavaz, M.E. Ali, M.M. Islam and S.B. A. Hamid. Nanoscale Res. Lett, **11**, 510 (2016).

8   T. Guo, P. Nikolaev, A.G. Rinzler, D. Tomanek, D.T. Colbert and R.E. Smalley. J. Phys. Chem, **99**, 694 (1995).

9   S. Ncube. Electronic transport properties of Single Walled Carbon Nanotubes Synthesized by Laser Ablation. MSc thesis, University of the Witwaterarnd, 2014.

10 H.O. Pierson, Handbook of Chemical vapor Deposition. Noyes Publications and William Andrew Publishing, 1999.

11 V.J. Artyukhov, E.S. Penev and B. Yakobson. Nat. Commun, **5**, 4892. (2014).

12 T.W Odom, J.L- Huang, C.L. Cheung and C.M. Lieber. Science, **290**, 1549 (2000).

13 S. Datta, Electronic Transport in Mesoscopic Systems. Cambridge university press, 1997.

14 J.C. Chalier, X. Blase and S. Roche. Rev. Mod. Phys, **79**, 677 (2007).

15 S. J. Tans, M.H. Devoret, H. Dai, A. Thess, R.E. Smalley, L.J.Geerligs, and C. Dekker. Nature, **386**, 474 (1997).

16 S. Ncube, G. Chimowa, Z. Chiguvare and S. Bhattacharyya. J. Appl. Phys, **116**, 024306 (2014).

17 A.B. Kaiser. Rep. Prog. Phys, **64**, 1 (2001).

18 V. Skákalová, A.B. Kaiser, Y.-S. Woo and S. Roth. Phys. Rev. B, **74**, 085403 (2006).

19 T.W. Ebbesen, H.J. Lezec, H. Hiura, J.W. Bennett, H.F.Ghaemi and T. Thio. (1996).

20 M.F. De Volder, S.H. Tawfick, R.H. Baughman and A.J. Hart. Science, **339**, 535 (2013).

21 S.A. Wolf, D.D. Awschalom, R.A. Buhrman, J.M. Daughton, S. von Molnár, M.L. Roukes, A.Y. Chtchelkanova and D.M. Treger. Science, **294**, 1488 (2001).

22 V.A. Ivanov, T.G. Aminov, V.M. Novotortsev and V.T. Kalinnikov. Russian Chemical Bulletin, **53**, 2357 (2004).

23 M.N Baibich, J.M. Broto, A. Fert, F.N. Nguyen Van Da, F. Petroff, P. Etienne, G. Creuzet, A. Friederich and J. Chazelas. Phys. Rev. Lett, **61**, 2472 (1988).

24 G. Binash. P. Grünberg, F. Saurenbach and W. Zinn. Phys. Rev. B, **39**, 4828 (1989).

25 S. Parkin, S.A. Wolf, J.S. Harris, S. Zhang and D.J. Smith. Redefining the Architecture of Memory. The New York Times, 2007.

26 A. Fert. Reviews of Modern Physics, **80**, 1517 (2008).

27 M.T. Johnson, P.J.H. Bloemen, F.J.A. Den Broeder and J.J. De Vrier. Rep. Prog. Phys, **59**, 1409 (1996).

28 J.C. Slonczewski. Electronic device using magnetic components. U.S. Patent, **5**, 864 (1997)

29 J.E. Hirsch. Phys. Rev. Lett., **83**, 1834. (1999).

30 T. Senthil, J.B. Marston and M.P. Fisher. Phys. Rev. B, **60**, 4245 (1999).

31 N.A. Chuang and L.L. Gershenfeld. Science, **275**, 350 (1997).

32 M.B. Johnson, and B. Mark. U.S. Patent, **5**, 695 (1996).

33 J.M.D. Coey. Magnetism and Magnetic Materials. Camridge University Press, 2010.

34 E.Y. Tsymbal and D. Pettifor. Solid State Physics, **56**, 113 (2001).

35 E.Y. Tsymbal and I. Zutic. Handbook of Spin Transport and Magnetism. Chapman and Hall/CRC, 2011.

36 C. Kittel. Introdudtion to Solid State Physics (6th ed). John Wiley and Sons, 1986.

37 L. Néel. Annales de Physique, **3**, 137 (1948).

38 Kumar, S.G. Bhata and P. S. Anil. AIP Advances, **6**, 056308 (2016).

39 S. Datta and B. Das. Appl. Phys. Lett., **56**, 665 (1990).

40 M.N. Baibich, J.M. Broto, A. Fert, F.N. Van Dau, F. Petroff, P. Etienne, G. Creuzet, A. Friederich, and J. Chazelas. Phys. Rev. Lett., **61**, 2472 (1988).

41 G. Schmidt, D. Ferrand, L.W. Molenkamp A.T. Filip, and B.J. Van Wees. Phys. Rev.B, **62,** R4790. (2000).

42 F.G. Monzon, H.X. Tang and M.L. Roukes. Phys. Rev. Lett, **84**, 5022 (2000).

43 D.W. Bullock, V.P. LaBella, Z. Ding, and P.M. Thibado. Journal of Superconductivity: Incorporating Novel Magnetism, **15**, 37 (2002).

44 E.I. Rashba. Phys. Rev. B, **62**, R16267 (2000)).

45 M.E. Flatte. J. Byers and W.H. Hau. unpublished data.

46 D. Grundler, Phys. Rev. B, **63**, 16130 (2001).

47 S.K. Upadhyay, R.N. Louie and R.A. Buhrman. Appl. Phys. Lett, **25**, 3881 (1999).

48 W.H. Rippard and R.A. Buhrman. Phys. Rev. Lett, **84,** 971 (2000).

49 P.R. Hammar, B.R. Bennett, M. J.Yang, and M. Johnson. Phys. Rev. Lett, **84**, 5024 (2000).

50 S. Datta, and B. Das. Appl. Phys. Lett, **56**, 665 (1990)).

51 L.J. Sham and T. Ostreich. J. Lumin., **87**, 179 (2000).

52 M.E. Flatte, and G. Vignale. Appl. Phys. Lett, **78**, 1273 (2001).

53 L. Berger. Phys. Rev. B, **54,** 9353 (1996).

54 E.B. Myers, D.C. Ralph, J.A. Katine, R.N. Louie and R.A. Buhrman. Science, **285,** 867 (1999).

55 L. Kouwenhoven and L. Glazman. Physics World, **14**, 33 (2001).

56 J. Kondo. Progress of Theoretical Physics, **32**, 37-49 (1964).

57 P. Anderson. Phys. Rev B, **124**, 41 (1961).

58 S.M. Cronenwett. Science, **281**, 540 (1998).

59 V.N. Golovach and D. Loss. Europhys. Lett., **62** , 83 (2003).

60 B. Béri and N.R Cooper. Phys. Rev. Lett, **109**, 156803 (2012).

3. Experimental: Synthesis of Rare Earth Modified Multiwalled Carbon Nanotubes

3.1.   Introduction to Modification techniques

MWNTs were modified with gadolinium (Gd^{3+}) using two different routes namely; chemical functionalization of the outer walls with a complex, gadolinium diethylene triamine pentaacetic acid gadolinium (III) (Gd-DTPA) and capillary filling with $GdCl_3$ salt. Commercial grade MWNTs from Sigma Aldrich with an average diameter 20 - 30 nm, chemical purity >90 % carbon and low percentage of remnant of Co catalyst (0.3%) were used for the functionalization. CVD synthesized MWNTs and DWNTs from a collaboration with Emmanuel Flahaut from CNRS,Paul Sabatier University, were used for filling in dry powder form. In this work modification of the CNT overall properties is achieved by introducing magnetic entities within the physical realm of the 1D conductors, using the two methods mentioned above. The desired spintronic function is encoded in the composite by combining the expertise of chemistry and physics. Details of the modification are given in the sections below.

3.2.   Functionalization; Gd-DTPA

Functionalization is one of the main methods used to modify CNTs to further improve their already fascinating properties providing an impetus to extend their scope of application. Their high mechanical strength, stiffness and 1D nature [1] makes CNTs to be inherently insoluble in most solvents making them ideal for harsh chemical reactions involved in functionalization. Non-covalent functionalization preserves the structure of the CNT whereas covalent functionalization interferes with the structure of the CNT thereby introducing defects [2.3]. The choice depends on the intended function of the final product. For this study which focuses on electronic transport, covalent functionalization is chosen to firmly anchor the Gd-DTPA onto the outer walls to enhance the interaction of the CNT and the magnetic nanoparticles [4]. Covalent functionalization allows for a reliable alteration of the chemical, thereby electronic properties resulting in new functions. The ideal CNT has no functional groups hence chemically inert, but due to synthesis shortfalls and the accompanying purification techniques employed this is not the case.

3.2.1. Structure of Gd chelator

Chemical formula: $C_{14}H_{20}GdN_3O_{10} \cdot xH_2O$

The chelator commonly known as gadopentetic acid consists of a Gd^{3+} ion supported by a diethylene triamine pentaacetic acid (DTPA) as shown in figure 3-1. It facilitates a strong and stable attachment of the Gd atoms onto the CNT surface. The composite has been thoroughly studied and used for magnetic resonance imaging (MRI) applications [**5.6**]. The choice of Gd^{3+} would be expected, for no other ion has seven unpaired electrons. But there is a much subtler reason it performs so well. Two other lanthanide ions, dysprosium (III) and holmium (III), have larger magnetic moments (due to orbital contributions to electron angular momentum) than that of Gd(III), but the asymmetry of these electronic states leads to very rapid electron spin relaxation. The symmetric S-state of Gd^{3+} is a more hospitable environment for electron spins, leading to a much slower electronic relaxation rate [**7**]. Apparently, the off-the-shelf ligands such as DTPA form complexes strong enough so that, for the period that the agent is in the body, there is no detectable dissociation in the case of MRI contrast agents. Gd-DTPA consists of Gd^{3+} ion in the center and $DTPA^{5-}$ as shown in Figure 3-1. The Gd^{3+} is a 9-co-ordinate surrounded by 3 nitrogen atoms and 5 oxygen atoms from the carboxylate group. The ninth coordinate site is occupied by a H_2O molecule [**8**].
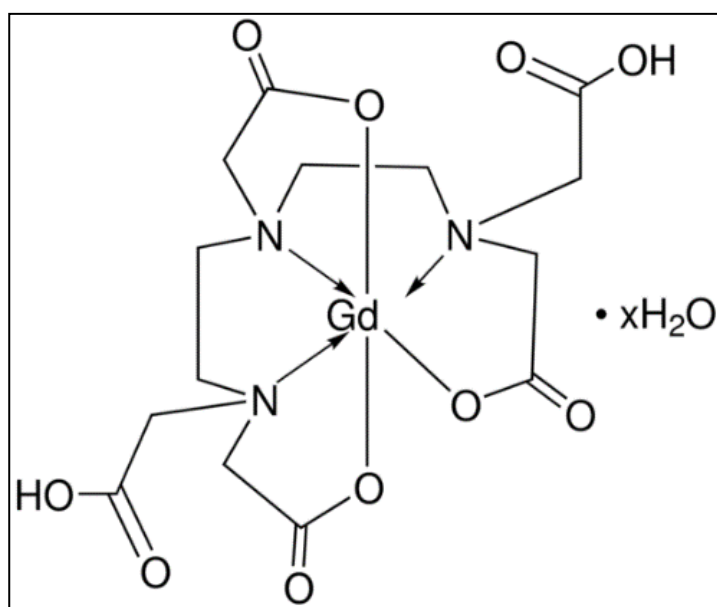
Figure 3-1 Structure of the Gadolinium- diethylene triamine pentaacetic acid (Gd-DTPA) chelator

3.2.2. Vacuum Schlenk line setup
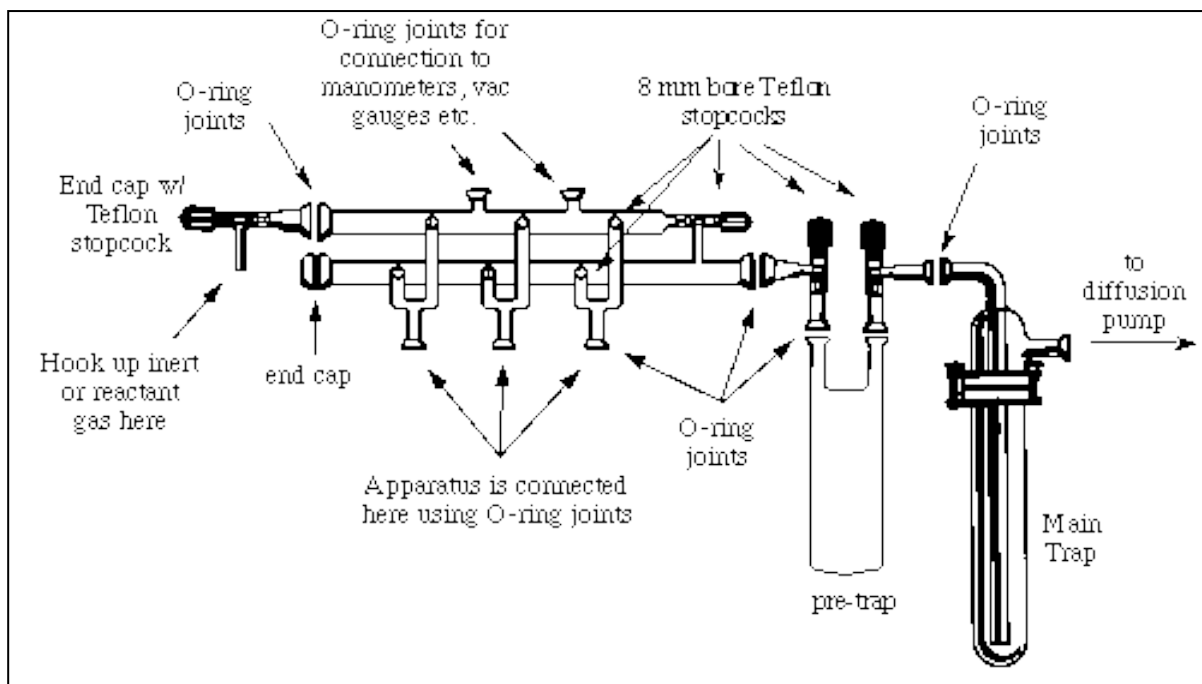
Figure 3-2 Schlenk line schematic showing how the manifold and traps are joined.
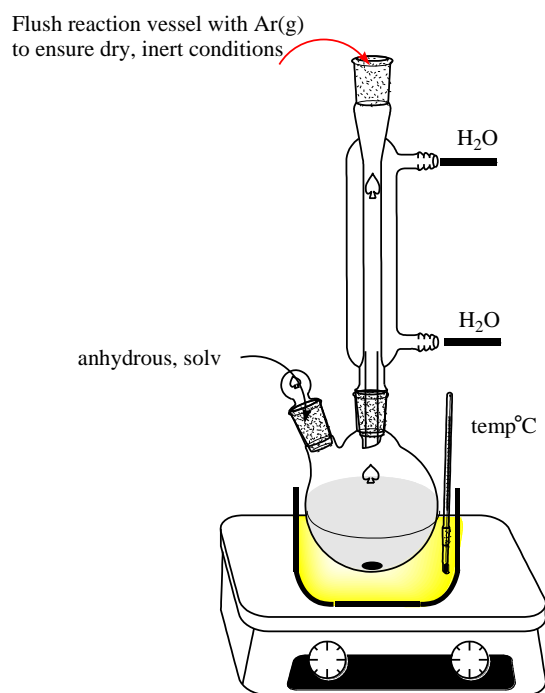
Figure 3-3 Reaction chamber (apparatus referred to in figure 3-2) vessel where the reactants are added and connected to Schlenk line.

The vacuum Schlenk line shown schematically in Figure 3-2 and the actual setup shown in Figure 3-4, also known as vacuum/inert gas manifold is used for the functionalization of the MWNT with Gd-DTPA. It is chosen for the synthesis because it is an air-free synthesis technique as some of the reactancts in this reaction like Gd^{3+} free ions are air sensitive and may react with air, oxygen, nitrogen or water. The main components of the Schlenk line is the dual manifold as shown in Fig 3-2. It has two parallel glass tubes; one connected to the inert gas supply and the other to the vacuum. Taps allow switching between the gas and the vacuum lines and a Schlenk line will generally have 3 - 6 taps to allow multiple reactions to be performed simultaneously. Figure 3-3 shows the reaction vessel that is connected to the vacuum line where all the reactants are added.

To use the manifold the steps below are followed;

1. Add the reactants to reaction chamber (2-neck round bottomed cylinder) and place in an oil bath on top of a hot plate
2. Connect the two-neck cylinder to a water-cooled condenser
3. Secure the reaction chamber on a retort stand
4. Connect the condenser to the manifold whilst isolating the unconnected ports
5. Place the cold trap in nitrogen to ensure any contaminants from the reaction vessels are trapped to protect the vacuum pump
6. Switch on the diffusion pump and evacuate the reaction vessel through the manifold
7. Isolate the reaction vessel by closing the vacuum inlet valve
8. Then flush the reaction vessel with argon to ensure dry inert conditions
9. The bubbler is used to monitor the argon flow rate
10. Start the reaction with a very low argon flow rate

3.2.3. Experimental setup

Figure 3-4 Experimental set up in the fume hood showing the complete connections for the Schlenk line

Figure 3-4 show the experimental setup in the fume hood of the vacuum line, showing the components of the vacuum line as outlined below.

1. Dual manifold
2. Inert gas inlet
3. Inert gas outlet via a bubbler
4. Connection to diffusion pump
5. Cold traps for solvents
6. Vacuum valves to switch between gas and vacuum
7. Tubing to connect apparatus to line

3.3.   Functionalization of MWNT

MWNTs with a diameter 20-30 nm were functionalized with a Gd-DPTA derivative by modifying known methods [9] using a 3-step method as shown in figure 3-5. The MWNTs are first functionalized with a mixture of nitric and sulphuric acid with a ratio of 3:1 respectively. A suspension of 452 mg of DTPA and 46 mg the -COOH functionalized MWNTs in triflouroacetic acid (TFA) (8ml) is sonicated at 30°C for 2 minutes to ensure even dispersion. The suspension is further stirred at room temperature for 20 h. This facilitates the coupling of the DTPA derivative which bears an amine function to the MWNT using TFA. After evaporation under reduced pressure, the residue is washed with diethylether, dichloromethane and methanol to neutralise the TFA and remove the remnants of DTPA. The solid residue is then dried under reduced pressure. Chelation of Gd^{3+} is achieved by dispersing 10.53 mg of MWNT- DTPA in 12 ml of a gadolinium perchlorate 40 % aqueous solution. The mixture was sonicated for 30 min and stirred at room temperature for 24 hours. Figure 3-5 is a representation of the chemical reaction for the complexation of the DTPA onto the CNT and the capture of the Gd into the centre of the DTPA ligand to form the complex. Figure 3-6 is a schematic representation of the complexation of the Gd-DTPA onto the CNT. The suspension was centrifuged and the aqueous supernatant checked for free Gd ions by colorimetric detection with xylenol orange. The reaction product was dried under vacuum to obtain Gd-Fctn MWNT. All reactions were performed under inert conditions.
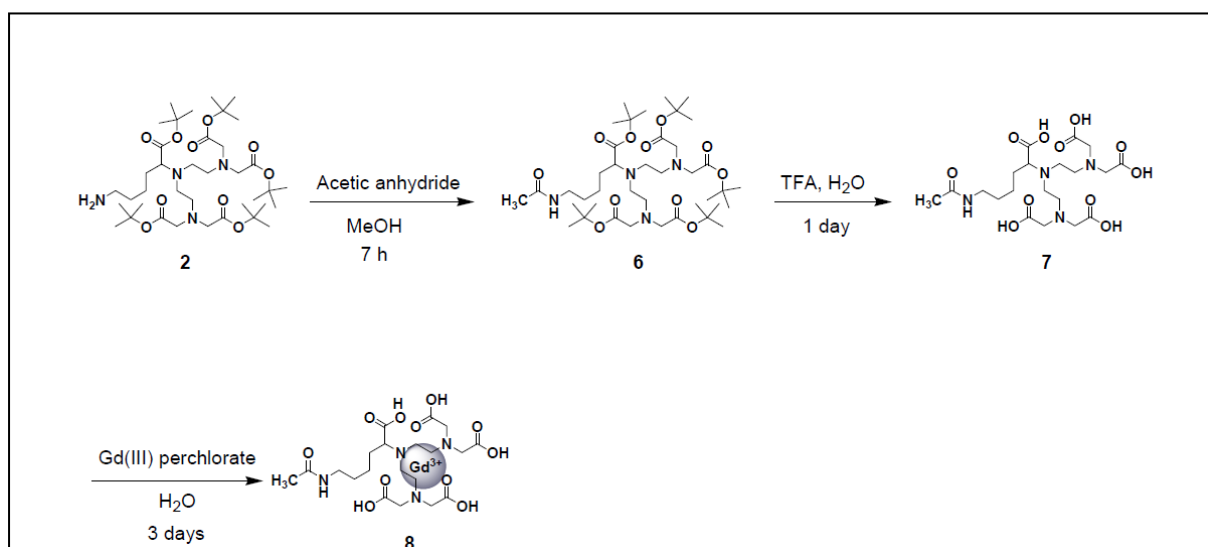
Figure 3-5 Chemical reaction for the complexation of Gd-DTPA
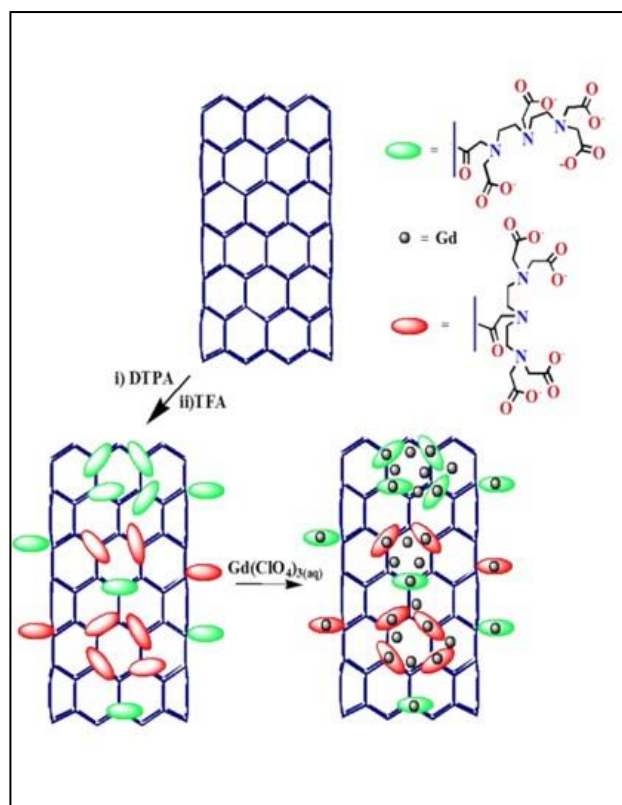
Figure 3-6 Formation of Gd-DTPA functionalized MWNTs schematic representation

3.4. Filling with GdCl₃

Figure 3.7 shows the structure of gadolinium trichloride (GdCl$_3$) which was used for filling into the core of the CNTs. It is found in the form of white crystals with a hexagonal structure as seen for other lanthanide chlorides [**54**] at ambient conditions. It is a 9-coordinate system with tricapped trigonal prismatic coordination sphere. The filling procedure is outlined below.
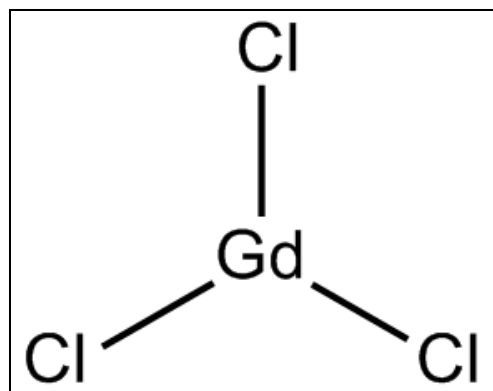
Figure 3-7 Structure of gadolinium trichloride which is a trigonal consisting of 1 gadolinium atom surrounded by 3 chlorine atoms

The GdCl$_3$ filled MWNT were prepared using a previously established methodology [**11**]. A mass of 5g of GdCl$_3$ anhydrous powder (purity 99.99%, 439770 Sigma Aldrich) were mixed together with 180 mg of dry CNTs using a mortar and pestle in a glove tent flushed with dry nitrogen. The mixture was transferred into a quartz ampoule. The ampoule was connected to a vacuum line and sealed. The sealed ampoule was transferred into a tubular furnace and submitted to the following heat treatment: heating from room temperature to 630°C at 5 °/min. A dwell of 24h was applied, after which the sample was first cooled down very slowly from 630°C down to 580°C at 0.1°C/min and then down to 480°C at 1°C/min and finally to room temperature at 5°C/min. The ampoule was cut using a glass knife and the sample recovered. It was washed with deionised water and then with concentrated HCl [6 mol/L] in order to dissolve gadolinium oxide which forms spontaneously during the washing with water. The products were washed until no excess Gd^{3+} could be determined by inductively coupled plasma atomic emission spectroscopy ICP-EOS [**12**]. Finally, the sample was freeze-dried.

3.5.   Device fabrication

Dielectrophoresis (DEP) was used to fabricate gadonanotube bundle devices. The gadonanotubes (Gd functionalized and Gd filled CNTs) are aligned by DEP using an alternating current of 1 MHz and ±5 V$_{pp}$ voltage. The gadonanotubes were dispersed in isopropylalcohol (IPA) and then sonicated for 6 hours. The resulting solution was drop cast on a prefabricated 6-gold-electrode system shown in figure 3-8 (a,b,c,d) with a separation distance of approximately 5 and 1.5 μm between the furthest and closest electrodes respectively as shown in figure 3-9 (c). The prefabricated electrodes are deposited on a silicon substrate with 300 nm oxide layer are zoomed in to show finer details. The outermost electrodes were used to contact a four-terminal device configuration using a wire bonder. Devices with 2- electrode and ground terminals were also fabricated as shown in figure 3-8(b). The resulting hybrid devices to be used for electronic transport consisted of a few bundles of CNTs aligned across the electrodes. Figure 3-9 (a,b,c,d) shows the hybrid devices resulting from the DEP alignment. The devices consist of bundles forming networks of CNTs horizontally aligned across the electrodes. Devices consisting of a few bundles are chosen for the electronic transport measurements.
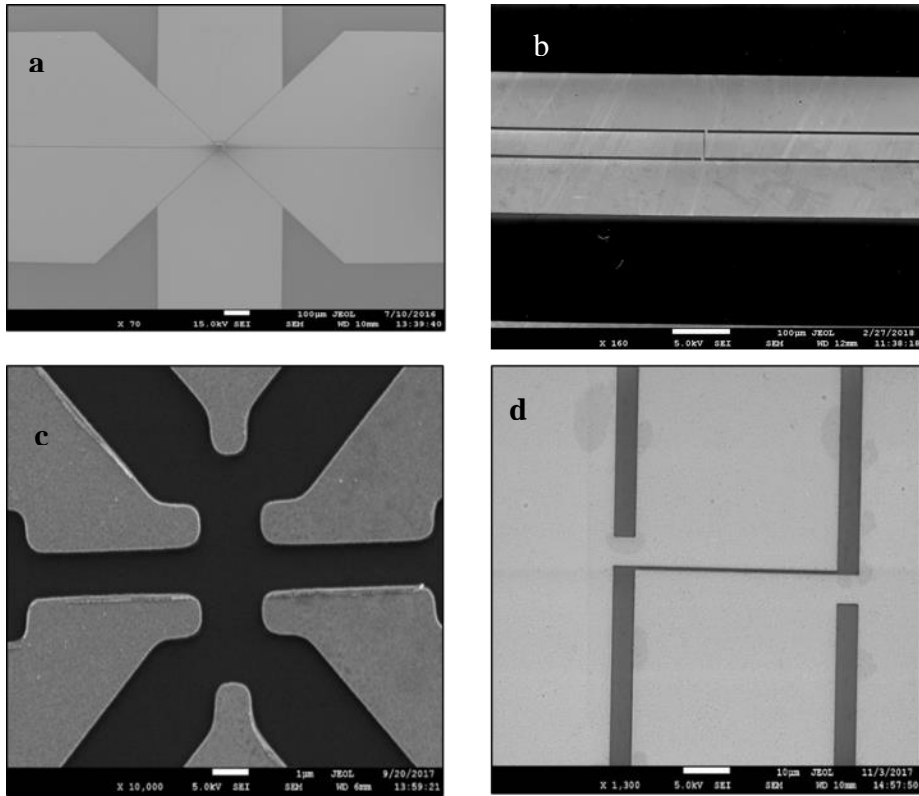
Figure 3-8 SEM images of the electrodes before the CNTs are dispersed on 6-terminal (a) and (c) and 2-terminal device configuration with ground electrodes (b) and (d). (c) shows the central region of (a) when zoomed in and (d) shows the central region of (b) when zoomed in.
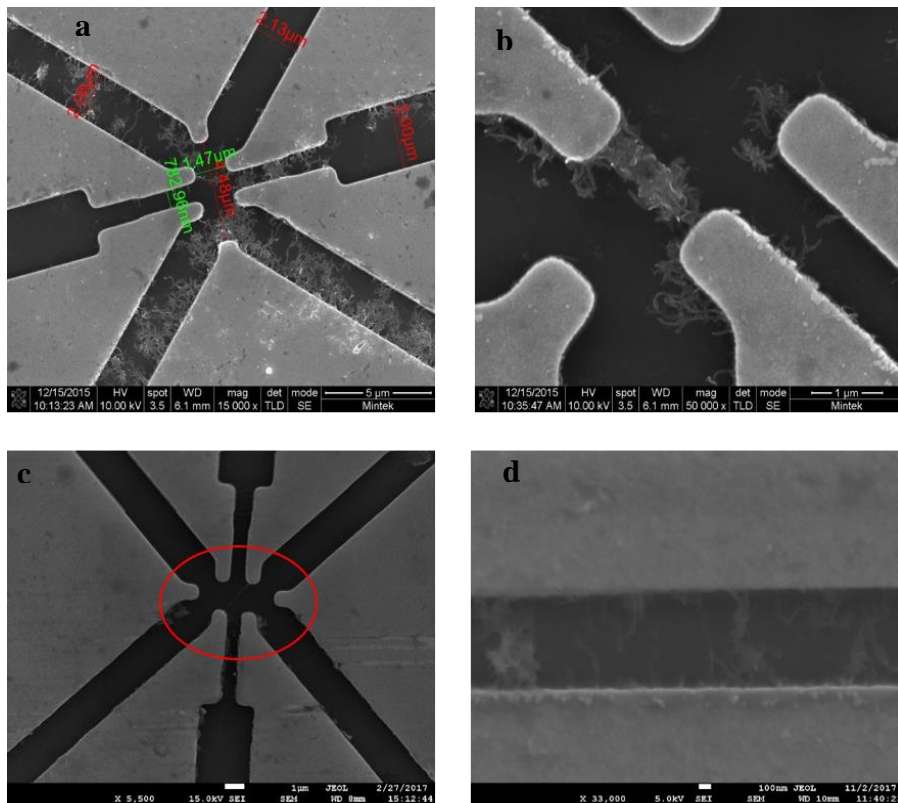
Figure 3-9 SEM images of prototype devices used in low temperature electronic transport studies showing multiple bundles aligned across a 6-terminal (a,b,c) and 2-terminal (d) gold electrodes

3.5.1. Device testing
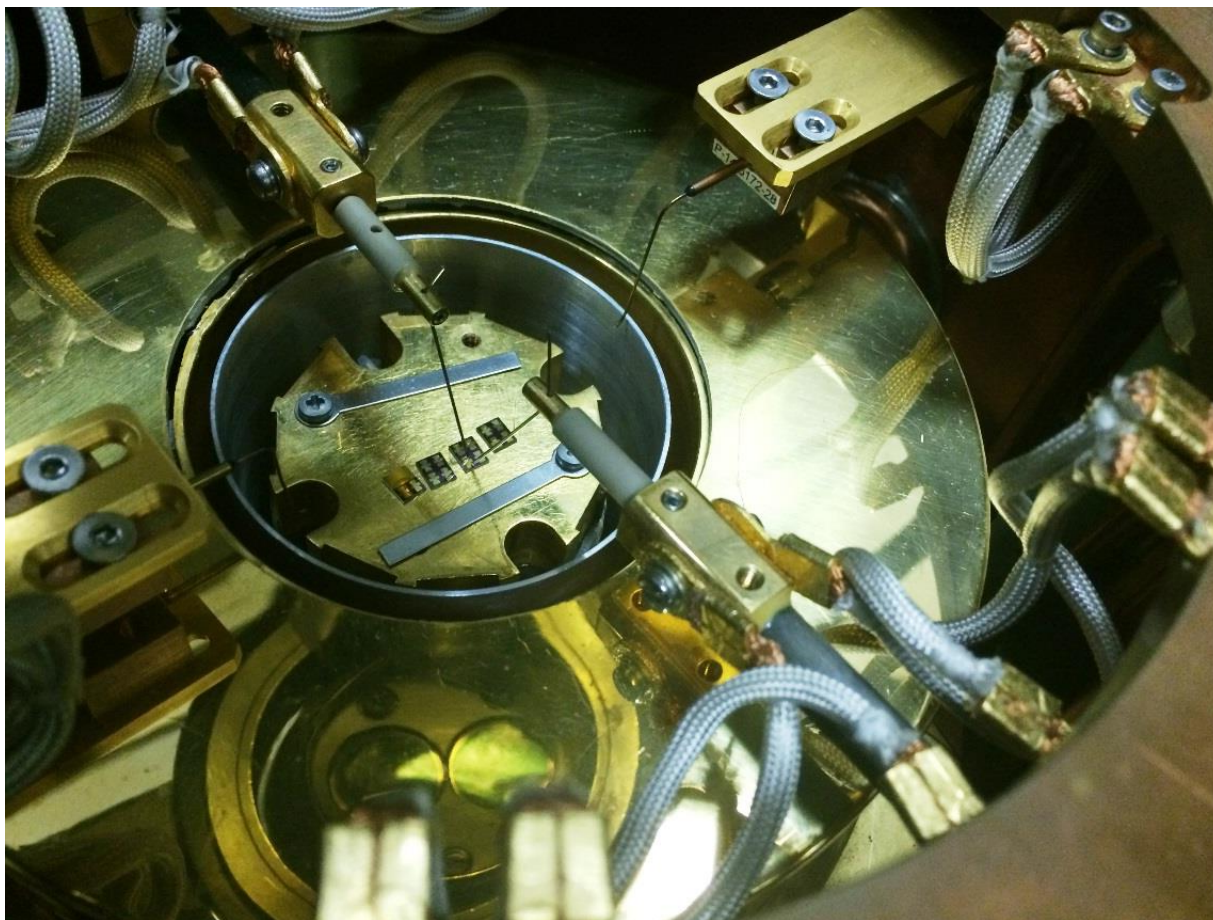
Figure 3-10 Device testing in the Janis Micro-Manipulated semiconductor device analyser probe station

All the devices fabricated by DEP were routinely tested in the Janis Micromanipulated Semiconductor Device Analyzer Probe Station under ambient conditions before wire bonding. Two-terminal measurements are conducted on each set of electrodes for the 6-terminal devices configuration. Devices with conductance in the nA to a few µA range are chosen for the electronic transport measurements. Figure 3-10 shows four chips each with 4 devices being tested.

3.5.2. Characterization techniques

Quantification of the Gd concentration in the nanocomposites was done by a microwave-assisted HNO_3/H_2SO_4 digestion (Ultra Wave Millestone) and analysis by ICP AES (ICAP 6500 Thermofischer Scientific). FTIR was used to obtain the infrared absorption spectra of the pristine and the Gd - functionalized MWNTs. SEM and TEM, Energy Dispersive X-Ray Spectroscopy (EDX) were used to determine if the functionalization was successful through

the detection of Gd in the nano composite. TEM was used for checking the surface of the CNT for successful functionalization with Gd. HRTEM was used for further analysis of the functionalization and the filling at higher magnification.

Electronic transport characterization was done in the Cryogenic high field measurement system on the hybrid gadonanotube devices. The resistance of the devices was tested at room temperature to check for contact quality. Ideal devices have resistances of 50 – few hundred kiloohms (kΩ) at room temperature. *I-V* measurements were done from room temperature to 300 mK. The Resistance vs Temperature measurements were carried out from 300 mK to 300 K using a Keithly 2400 to supply a current of 1 μA and a Keithly 2182A nano-voltmeter to measure the voltage across the sample. The magnetoresistance (MR) was measured as a function of applied field ramping at constant rate from -0.5 to 0.5T at different excitation currents, at 300 mK. The transport of electrons in the nanotube hybrids was investigated by measuring the differential conductance *G= dI/dV* as a function of source drain current.

Magnetization *(M(H))* and susceptibility *χ = M(T)/H*, (*H*=100 Oe) studies of the composite were carried out at room temperature using an ultra-sensitive superconducting quantum interference device MPMS-SQUID magnetometer from Quantum Design, San Diego. The sample was weighed and loaded in a plastic straw. Background subtraction was done before each measurement. The susceptibility from 350 - 2 K was measured as well as the magnetic hysteresis at room temperature. The susceptibility was measured at zero field cooled (ZFC) and field cooled (FC) conditions. In ZFC the sample is cooled without any applied magnetic field to the desired temperature. For FC curves, sample is cooled with an applied magnetic field to the desired temperature.

3.6.   Experimental facilities

3.6.1. Cryogenic high field measurement system

The cryogenic high field measurement system shown in figure 3-11 is a state of the art facility used for low temperature electronic transport measurements as well as vibrating sample magnetometer (VSM) capability. It consists of a closed helium condensation cycle controlled by a compressor that is used to cool a variable temperature insert (VTI) to 40 K in the first stage then further cooling through a pot to 4 K. The sample is systematically inserted into the VTI chamber using a special sample holder after a series of evacuation procedures to ensure that the cryogenic system is not contaminated. The sampler holder is a probe, two are available

one that cools directly to 2 K when the VTI is at its base temperature and a second one that cools to 300 mK through a pot(reservoir) of He^3 connected to the top of the sample holder which undergoes a cooling cycle through the sorption pumps.

The device is connected to the sample holder using wire bonding from the device's prefabricated electrodes to the sample holder contact pads. The sample holder consists of 6 contact pads with electrical connections to the long sample holder rod which is used to insert the sample into the VTI. The sample chamber is evacuated and flushed with helium gas before inserting the sample. The VTI and sample chamber are separated by a manually operated gate valve. The VTI pressure is controlled by a needle valve and controlled to ensure stability of the temperature during measurement. For this system the VTI pressure is set to 7 mbar during normal operation.

Before operation the system is warmed up to room temperature to prepare for evacuation. The VTI is evacuated for 24 hours with the needle valve opened to full capacity to remove any contaminations. Then the He insert is also evacuated for 12 hours. The dump (which is a cylinder that stores the He for closed loop circulation during operation) is emptied and refilled to the required level with He^{4+} gas and connected through the He^{4+} insert. Then the compressor

Figure 3-11 Experimental facilities showing the cryogenic high field measurement system

is switched on to circulate the He to cool the VTI, and the rest of the system to the recommended temperatures. The VTI must cool to a temperature of approximately 170 K. When the first stage and second stage reach 40 K and 4 K the Helium from the dump condenses into a pot and forces the VTI to cool further to a base temperature of 2 K.

The sample is connected to the measuring instruments through an electronic black box with different lines corresponding to how the device is wired. A Keithley 2400 is used as a source meter and a Keithly 2182A is used as a nano-voltmeter along with Stanford Research model SR830 DSP lock in amplifiers. Lakeshore temperature controllers are used to monitor the temperature in various parts of the instrument namely; VTI, sample stage, 1st stage, 2nd stage, inner magnet, outer magnet, He pot, magnet switch, sorption pumps. The magnet is controlled by a Cryogenic Ltd magnetic power supply.

3.6.2. JEOL 7001 Scanning electron microscope

The JEOL SEM 7001F shown in figure 3-12 is used for imaging of devices and device fabrication. It comes with a gas injection system with platinum, tungsten and Teos (Tetraethyl orthosilicate) sources, as well as a nanomanipulation capability using four different levers that can be controlled in the x,y and z direction. The SEM can also be used for Ebeam lithography patterning using RAITH software for fabrication of devices. It is pumped down to a vacuum pressure of 5 x 10 $^{-9}$ Pa for good operation. The acceleration voltage can go up to 30 kV. There is a chamber scope used to monitor the sample loading and the stage position.
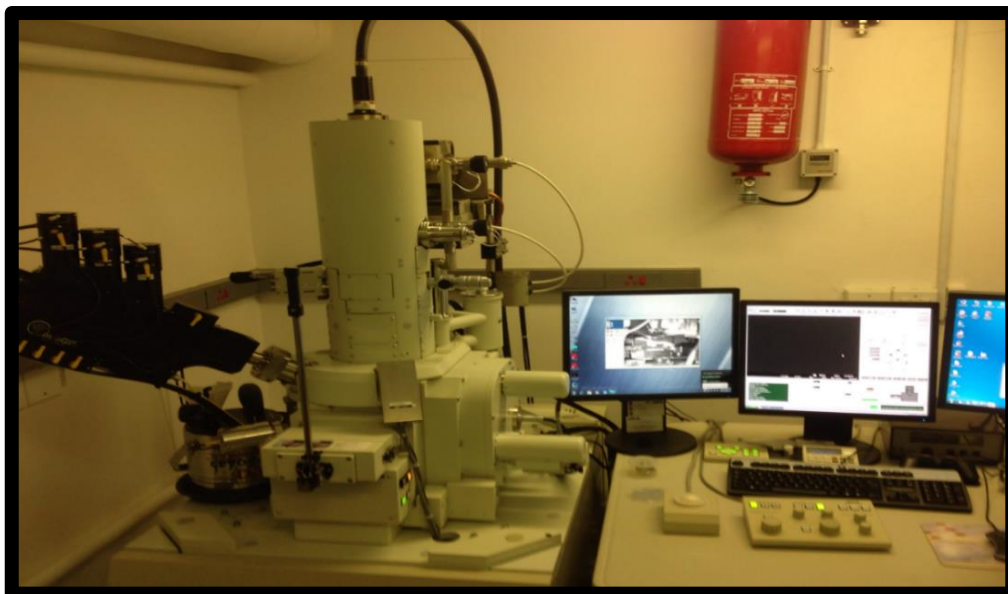
Figure 3-12 SEM with Ebeam lithography capability and gas injection system

3.6.3. Janis Micro-manipulated semiconductor device analyser probe

Figure 3-13 Janis micro manipulated semiconductor analyser probe station

station

The Janis micromanipulated probe station semiconductor device analyser shown in figure 3-13 is used to test devices prior to wire bonding. It consists of a two-terminal configuration with SMU connected to source and drain and one from ground. The sample chuck also acts as a gate connector so back gated devices can be characterised. The Janis micro-manipulated probe station consists of a sample stage housed in a small cryostat which can be cooled to 77 K using liquid nitrogen or 4 K if liquid helium is used. It also has high frequency capability.

3.6.4. Di-electrophoresis deposition probe station

Figure 3-14 shows the dielectrophoresis (DEP) alignment station used for the fabrication of bundle CNT devices at ambient conditions. A frequency generator is used to generate a frequency of 1 MHz which is controlled through an oscilloscope set at a ±5 Vpp. The chip with four sets of pre-patterned electrodes is positioned on the stage (shown in the inset of figure 3-14) under the metal pins connected to the frequency generator and oscilloscope. One set of electrodes is chosen, and contact is established with the pins. At this point the connection is open circuit. The alignment is achieved by carefully drop casting a small volume of solution of the sonicated CNTs onto the gap in between opposite electrodes to get devices shown in figure 3-9.
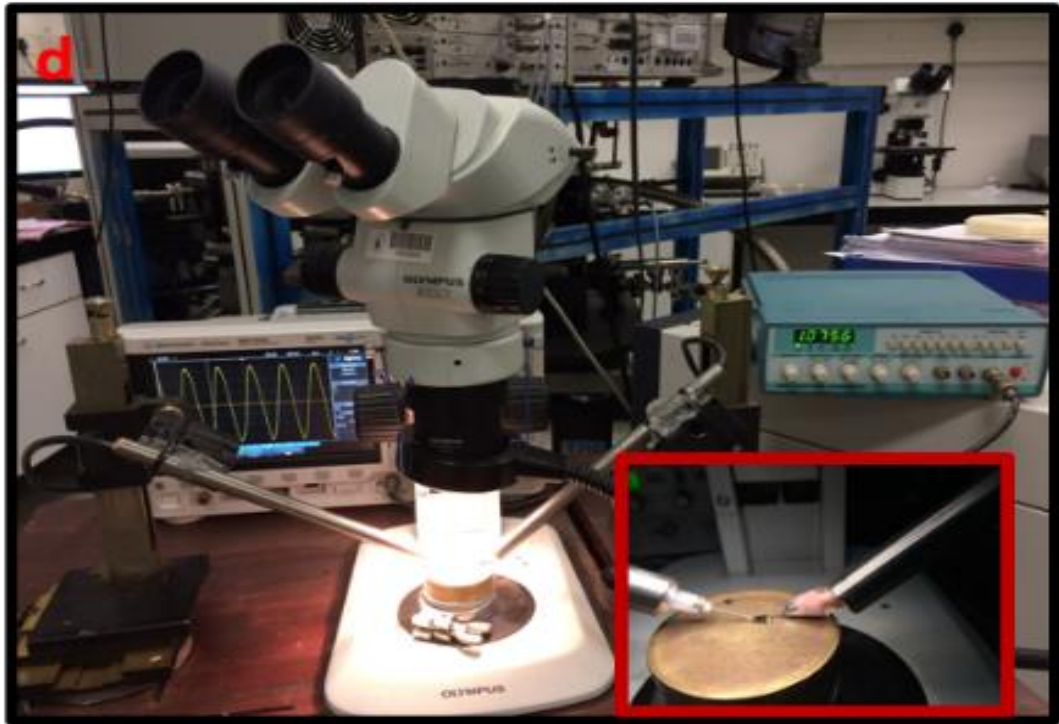
Figure 3-14 Di-electrophoresis probe station. Inset showing sample stage where the alignment is done.

3.6.5. E-beam lithography

E-beam lithography is used for the fabrication of electrodes shown in figure 3-8. The electrodes are fabricated on a silicon substrate with 300nm oxide layer. The steps followed are outlined below and a schematic representation is given in figure 3-15.

1. Spin coating with PMMA resist
2. Expose the resist to electron beam
3. Chemical development to remove the exposed PMMA
4. Deposit platinum 10nm as a seeding layer then gold 40nm in a metallization chamber
5. Dissolve the excess PMMA through a lift off process
6. Removal of the excess metal to remain with the patterned electrodes.
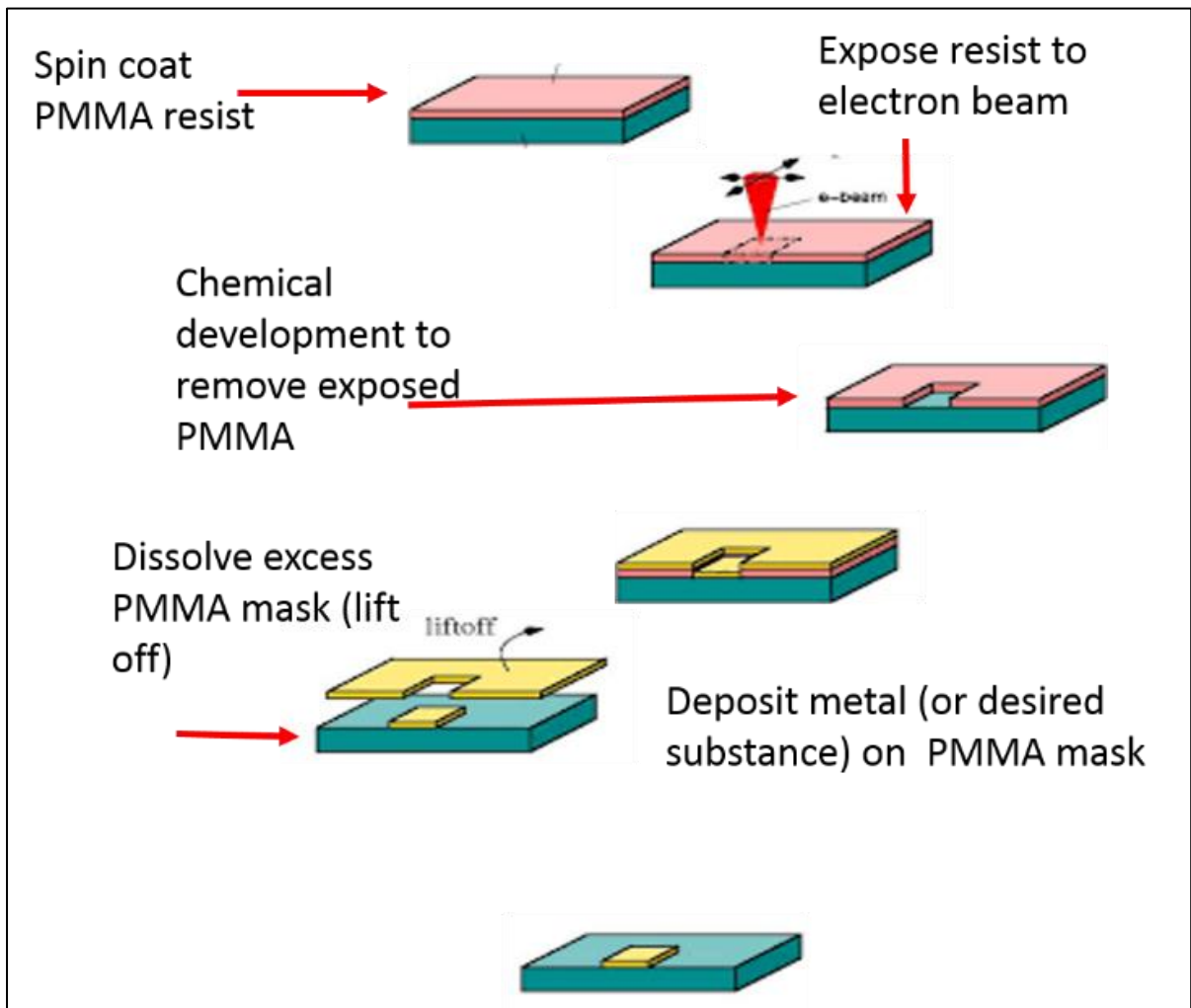
Figure 3-15 E-Beam lithography steps for fabrication of electrodes

References

1   K. Balasubramanian and M. Burghard. Small, **1**, 180 (2005).

2   A. Hirsch and O. Vostrowsky. Functionalization of carbon nanotubes. In *Functional molecular nanostructures*. Springer, 2005.

3   Y-P. Sun, K. Fu, Y. Lin and W. Huang. Acc. Chem. Res, **35,** 1096 (2002).

4   J. Blasco, V. Cuartero, G. Subías, M.V. Jiménez, J.J. Pérez-Torrente, L.A. Oro, M. Blanco, P. Álvarez, C. Blanco and R. Menéndez. Journal of Physics, Conference series. (2015).

5   B. Sitharaman and L.J Wilson. Int J Nanomedicine, **1**, 291 (2006).

6   R. Sethi, Y. Mackeyev and L.J. Wilson. Inorganica Chim. Acta, **393**, 165 (2012).

7   P. Caravan, J.J. Ellison, T.J. McMurry and R.B. Lauffer. Chem. Rev, **99**, 2293 (1999).

8   A.D. Sherry, P. Caravan and R.E. Lenkinski. J. Magn. Reson, **30**, 1240 (2009).

9   I. Marangon, C. Ménard-Moyon, J. Kolosnjaj-Tabi, M. L. Béoutis, L. Lartigue, D. Alloyeau, E. Pach, B. Ballesteros, G. Autret, T. Ninjbadgar, D. F. Brougham, A. Bianco and F. Gazeau. Adv. Funct. Mater, **73**, 7173 (2014).

10   H.J. Seifert, H. J. Therm. Anal. Calorim, **83**, 479 (2006).

11   P. Lukanov, C.-M. Tîlmaciu, A.M. Galibert, B. Soula and E. Flahaut. Filling of Carbon Nanotubes with Compounds in Solution or Melted Phase. In Carbon Nanotubes for Biomedical Applications. Carbon Nanostructures. Springer, 2011.

12   L. Ayouni-Derouiche, M. Mejean, P. Gay, M-L. Milliand, P. Lanteri, L. Gauthier and E. Flahaut. Carbon, **80**, 59 (2014).

4. Magnetotransport in Gadolinium Functionalized Multi Walled Carbon Nanotubes

4.1. Introduction

Over many years there have been various attempts to investigate the interaction between nanomagnets and conductors/semiconductors to develop spintronic devices based on ferromagnetic metal and carbon nanotubes [1]. Carbon nanotubes are ballistic conductors which exhibit exciting quantum transport phenomena such as Luttinger liquid behaviour [2] [3][4] and the Coulomb Blockade [5][6][7]. Yet this material suffers from weak spin orbit interaction which limits the observation of strongly correlated resonant transport features including the Kondo effect [8][9][10], Andreev reflection [11][12], and the Majorana zero modes [13] which have been reported in a range of other nanowires. Goldhaber-Gordon and co-workers pioneered the Kondo resonance study in CNT devices through the observation of the zero-bias anomaly peak which remains elusive in a CNT network [14]. Much work has been done to find a material that serves as a good electron conductor as well as spin mediation. It is well known that chirality of an individual CNT determines the successful spin transport which limits the spintronic application of this material. However, bundles of CNTs working as a multichannel system can overcome this problem if CNTs can be doped with a rare earth element and a link between the metal islands through the carbon backbone is established. Previous attempts in CNT based devices show that both localization and tunnelling effects can have dominant features in the transport [15]. Although SWNT networks and individual tubes can exhibit either semiconducting or metallic behaviour [15], bundles and MWNTs generally show an activated transport mechanism where fluctuation-assisted tunneling effects dominate the transport [15]. These cotunneling phenomena have also been shown to lead to spin accumulation [16] and can drastically enhance tunneling magnetoresistance (TMR) [17] and lead to enhanced spintronic device properties.

A new synthesis route of networking CNTs through the clusters of a gadolinium (Gd) based complex that effectively forms a multichannel system that results in exciting electronic transport features related to Kondo effect and effective enhancement of spin-orbit coupling is presented in this chapter. It is well known that due to weak spin orbit coupling the spin relaxation time of carbon systems, particularly CNTs, is relatively large (approximately 1 µs)

[18]. SWNTs and MWNTs are not intrinsically magnetic but do show diamagnetic susceptibility that increases linearly with diameter [19][20] when a magnetic field is applied. Interestingly, it has been demonstrated that the susceptibility of MWNT is highly anisotropic with regard to the orientation of the applied field and that the susceptibility is less diamagnetic with fields parallel to the CNT axis than in the perpendicular orientation [21][22]. Due to these favourable properties there have been many studies on the use of CNTs for spin valve devices, these typically involve the coupling of a CNT to ferromagnetic leads and injecting spin polarized current through the CNT and measuring the response [23-28]. There have also been investigations on supramolecular spin-valve devices based on individual SWNT non-covalently functionalized with molecular magnets along the surface of the CNT [29]. The advantage of using such supramolecular devices is that the specific magnetic molecules attached to the CNT can be tailored to exhibit the desired magnetic properties [30,31]. The non-covalent functionalization preserves the integrity of the structure of the CNT but spin interaction between localized magnetic moment and conduction electrons is weakened. There are however a range of possible routes for the attachment of molecules to CNTs, ranging from weakly attached grafting to strongly attached covalent bonding of the molecule onto the CNT [32]. A comparative study of the effect of method of the nanomagnet attachment on the magnetic response is yet to be made. Filling of CNTs is an alternative route to modifying their properties. There have been many reports on the filling of CNTs with a range of materials such as metals (Fe, Co, W), chalcogenides (Te, Se) and even other carbon structures such as buckyballs [33,34,35].

In this work the properties of a supramolecular complex synthesized using a chemical method of incorporating gadolinium magnetic nanoparticles onto a MWNT system via a DTPA molecular complex that has been widely studied as an MRI contrast agent [33] are investigated. The focus is on covalent attachment of a Gd-DTPA complex to the outer wall of the MWNTs. Gd^{3+} which is of particular interest due to its high effective paramagnetic moment = 7,94 μ_B that is expected to allow for spin correlations in the MWNTs [36]. The attachment of Gd^{3+} to CNTs has been explored before, yielding interesting features such as the observation of superparamagnetism as well as first order paramagnetic-ferromagnetic transitions [37]. In this work it is shown that the functionalized MWNTs exhibit a finite magnetic coercivity and remanence at room temperature. Structural characterization is used to establish the origins for the difference in magnetic behavior from previous reports. The unexpected properties observed for the functionalized sample prompted electronic transport studies on devices fabricated from

a network of the functionalized MWNTs. This was done to determine the effect of the magnetic Gd-DTPA complex on the quantum transport of the MWNTs which is useful for high speed electronics and is an extension of an earlier study [**38**]. A saturating resistance was found as the temperature is lowered below 10 K. These features are explained as a result of Kondo effect in a spin electron correlated carbon system where spin flipping events can lead to spin switching of the (tunnel) magnetoresistance.

4.2.   Structural Characterization

It was found that the Gd-Fctn-MWNTs contain less than 0.2 mass percent cobalt (catalyst material), with 14.57 % of the mass determined to be gadolinium obtained from the ICP OES technique referred to in chapter 3. Comparing the infrared spectrum of the MWNT to that of the Gd-Fctn-MWNT affords evidence for functionalization of the pristine MWNT surface (Fig 4-1). The spectrum of Gd-Fctn-MWNT (figure 4-1) displays peaks in the range 3008 - 3550 cm^{-1} arising from O-H and C-H vibrations; the former may include vibrations of water molecules residing in the MWNT. Stretching vibrations of the carboxylate functionalities are evident from peaks in the range 1100 – 1740 cm^{-1}. In particular the peaks at 1636 cm^{-1}, 1661 cm^{-1} and 1734 cm^{-1} confirm the existence of three different carbonyl environments.
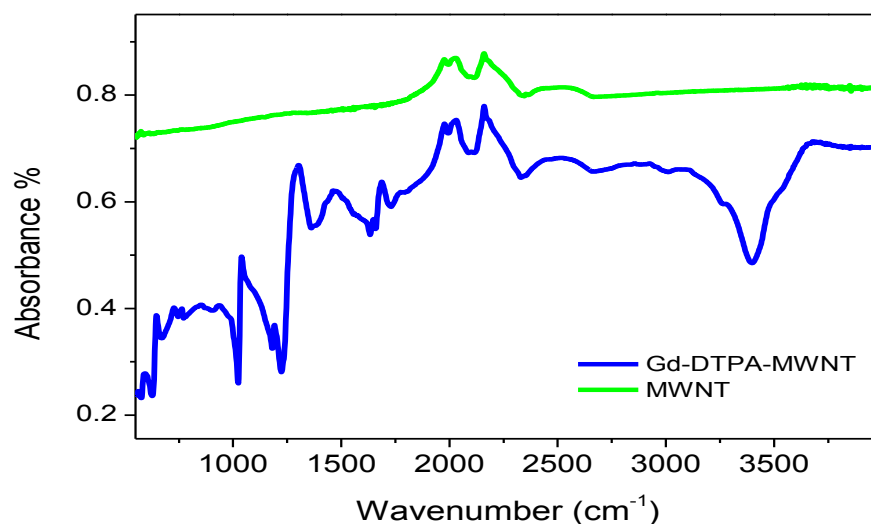
Figure 4-1 FTIR spectra of the pristine MWNT and the Gd-DTPA-MWNT after complexation

Table 4-1 is a complete compilation of the FTIR active vibrational modes observed in the functionalized material after the Gd-DTPA has been attached to the MWNTs. It is used to check the vibrational modes resulting from the functionalization of the Gd-DTPA onto MWNT.

Table 4-1 FTIR peak designation for the MWNT and the Gd-DTPA complex derivatives

Peak cm⁻¹	Designation
579	Gd-O vibrations
631	Gd-O vibrations
671	Gd-O vibrations
677	Gd-N vibrations
750	Gd-N vibrations
773	Gd-N vibrations
910	CH_2 deformation
1026	CH_2 bending vibration
1184	–C-O stretching vibration
1227	–C-O stretching vibration
1364	COO^- stretching vibration
1387	COO^- stretching vibration
1636	–C=O stretching vibration
1661	–C=O stretching vibration
1734	–C=O acyl stretching vibration on surface.
1998	**CNT**
2093	**CNT**
2120	**CNT**
2334	**CNT**
2344	**CNT**
2355	**CNT**
2668	**CNT**
3009	C–H stretching vibration
3017	C–H stretching vibration
3271	O–H stretching vibration
3402	O–H stretching vibration
3549	O–H stretching vibration
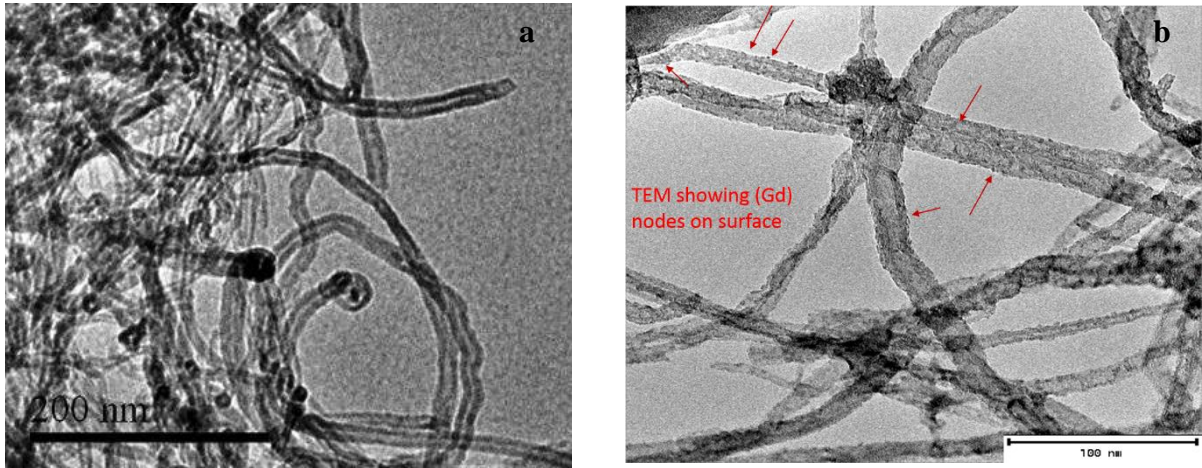
Figure 4-2 TEM image (a) Pristine MWNT showing smooth outer wall (b) Gd-DTPA functionalized MWNT showing nodes on the outer walls of the nanotubes
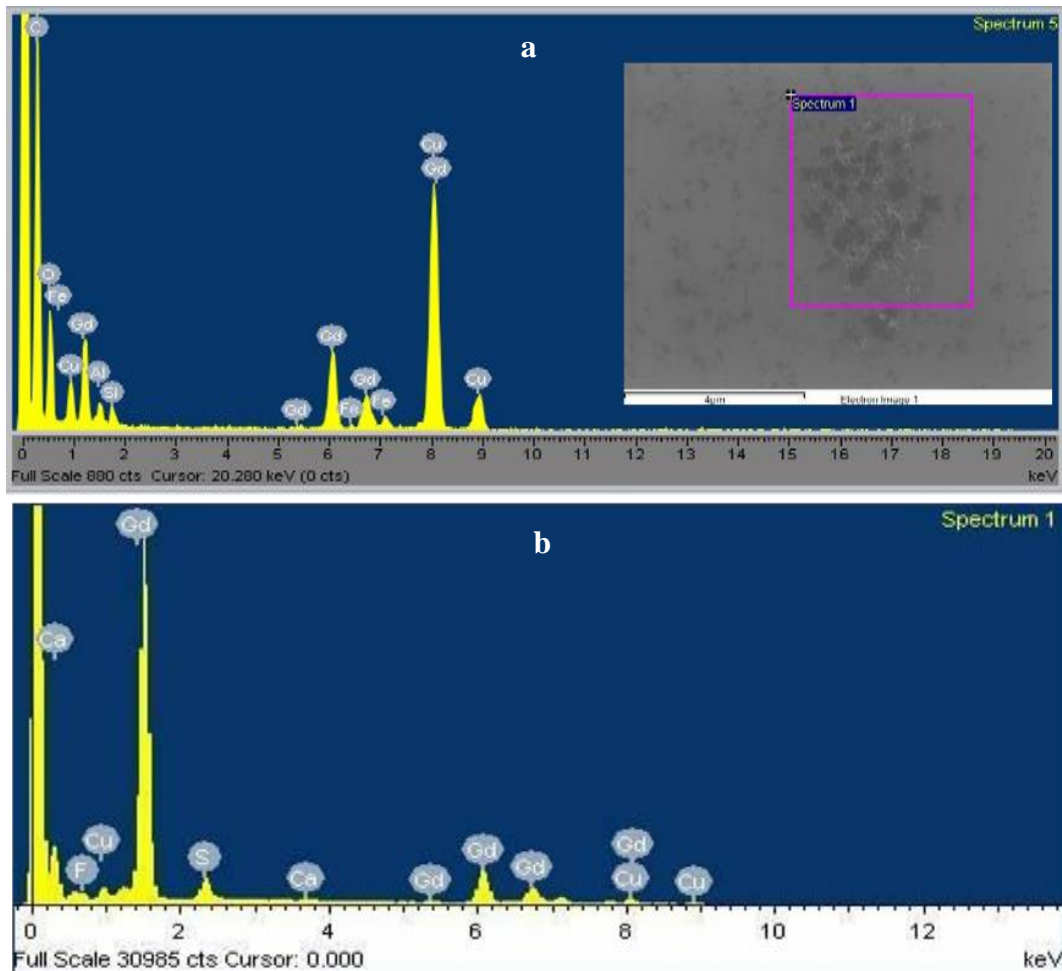
Figure 4-3 EDX elemental analysis done in the (a) SEM (inset shows area scanned) and TEM (b) showing the presence of Gd in the composite formed. Cu originates from the copper grid used.

Figure 4-2 (a) is a TEM image of the pristine MWNTs which shows featureless smooth walls. Figure 4-2 (b) is a TEM of the modified MWNTs which shows that are nodes on the outer walls but their morphology is not clear. EDX analysis data of the CNT nanocomposites are shown in figure 4-3. It was confirmed that Gd was present in the samples through the observation of the prominent peaks observed at 1.1, 6.05 and 8 keV; these are attributed to M, $L\alpha_1$ and $L\beta_1$ excitations specific to gadolinium.

A strategic approach towards covalently grafting a molecular paramagnetic species to MWNTs involves the use of DTPA molecules as suitable chelators covalently linked to the MWNT wall. Synthetic methodologies have exploited DTPA dianhydride as a starting reagent or have resorted to alternative bridging chains for covalent binding of the DTPA chelate to nanotubes. The former compromises chelation of the paramagnetic metal ion (Gd^{3+}) and inevitably is accompanied by a decrease in the ligand coordination number of the paramagnetic coordination polyhedron. In such instances the coordination polyhedron is completed by additional aqua ligands. The latter incorporates the chelate with increased flexibility affords higher rotational degrees of freedom to the Gd-O vector; affecting the possible transfer of magnetic information.
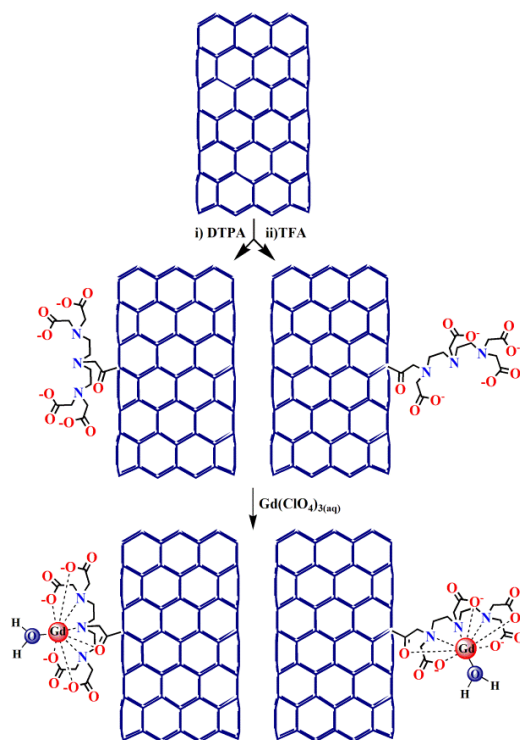
Figure 4-4 Schematic illustration of MWNT functionalization with subsequent DTPA chelation of paramagnetic ion (Gd^{3+}); varied attachment of the Gd-DTPA complex occurs through brachial carboxylate functionalities of the DTPA molecule.

An alternative approach described in the experimental section considers a more suitably rigid grafting of the Gd-complex to the CNT. In this work acylation of the nanotube surface using a polyaminocarboxylate chelate bearing several carboxylate functionalities is investigated as shown in figure 4-4. Grafting of DTPA chelates in this manner affords two possible binding modes in which the octadentate nature of the DTPA chelate is potentially retained. Octadenticity is closely associated with lower order (ML) Gd^{3+} complexes, while higher order $(M_xL_y)^{n+}$ complexes of decreased ligand denticity, enables completion of the coordination polyhedron by increased hydration or through proximal complex aggregation.

HRTEM was used to investigate the morphology of the Gd-Fctn-MWNT. The functionalized MWNTs (figure 4-5 (a)-(d) show that Gd^{3+} centers are accommodated by fibril and spherical shaped nanostructures of approximately 2 nm in diameter, with a relative uniform distribution in close proximity but not continuous coverage of the outermost surface of the MWNTs.Atomic resolution of the Gd-DTPA aggregate can be seen on the HRTEM image (figure 4-5.d).
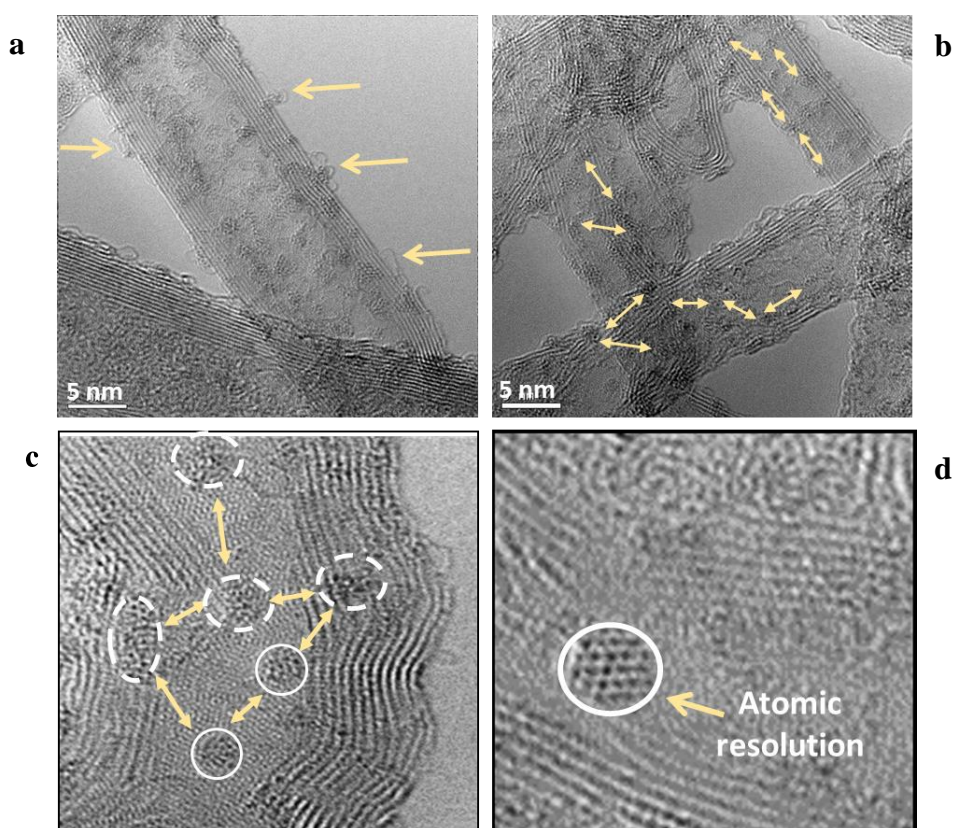
Figure 4-5 HRTEM image of MWNTs (a) the red arrows indicate regions along the nanotube that have strand like filament structures, believed to be a result of the DTPA ligand attachment. These strands are generally in close proximity to the multiple Gd^{3+} centers. (b) The MWNTs show a fairly homogenous distribution of the Gd-DTPA attachment throughout the sample, forming a network-like cover of the outer wall; distances between centres are indicated by the yellow arrows. (c) Multiple Gd-DTPA centres separated by a distance greater than 10 nm are indicated by the yellow arrows. (d) Morphology of aggregated centres viewed under higher magnification circled in red.

4.2.1. Magnetic domains on Gd-Fctn-MWNTs

Magnetic force microscopy (MFM) is used to investigate the existence of magnetic domains on the surface of the MWNTs after the functionalization. AFM image in the non-contact mode shows a bundles of MWNT (figure 4-6 a) and the corresponding MFM image showing bright spots on the surface of these bundles corresponding to magnetic domains. A line profile of the AFM and MFM scans corresponding height and phase profiling is shown in figure 4-6b. Zooming onto a single bundle, figure 4-6c shows bright islands on the CNT surface and the line profile, figure 4-6d shows peaks denoting a bundle of three tubes.
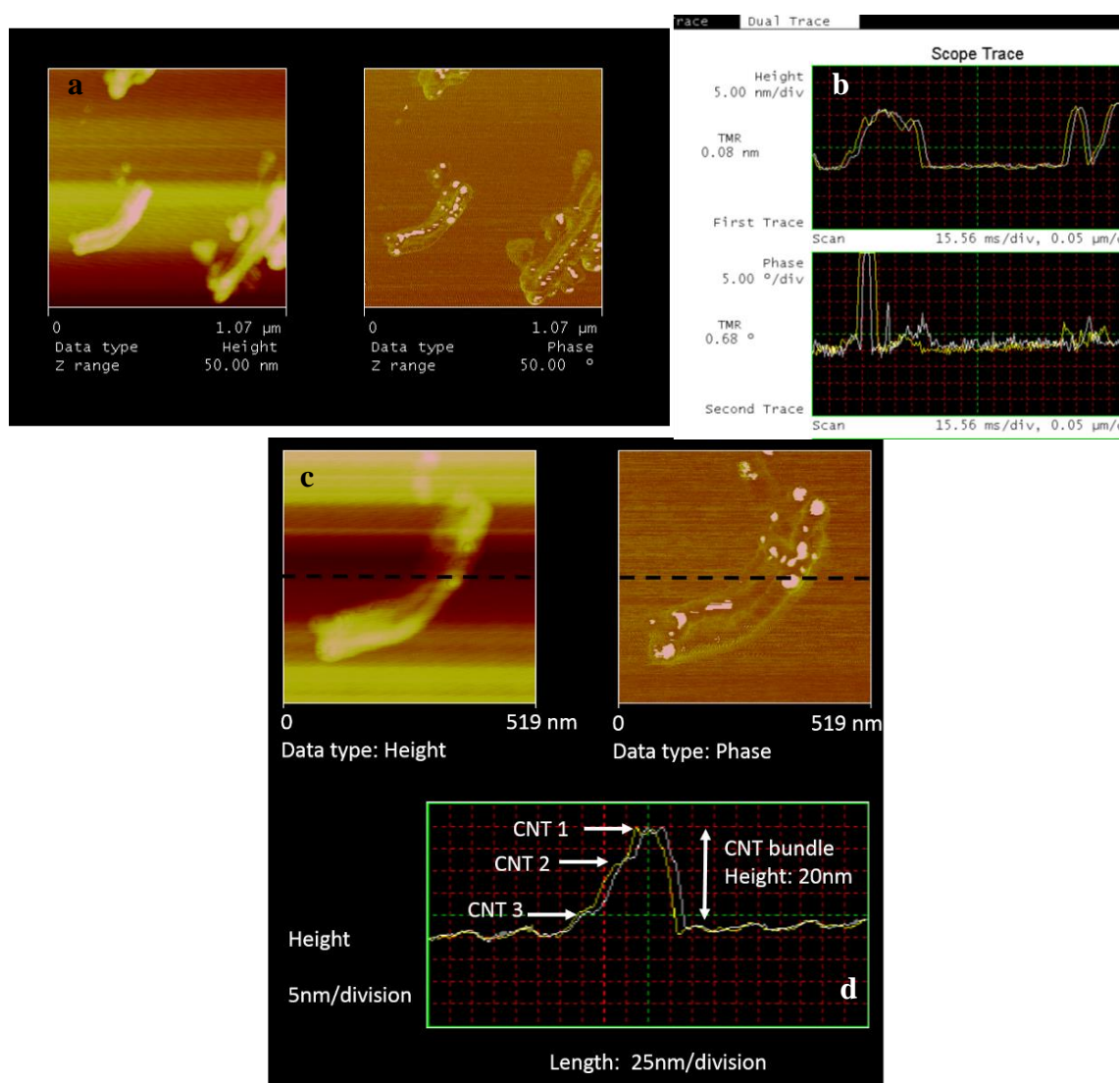
Figure 4-6 (a) AFM in non-contact mode showing a small bundle of MWNTs nanocomposite and corresponding MFM scan over the same area showing small bright features along the surface of the MWNT lengths, which indicates magnetic interaction with the probe tip due to existence of magnetic domains (b) Line profile of the AFM and MFM image. (c) AFM and MFM zoomed in to a single bundle (d) The height profile of a line scan dotted line in and across the MWNT bundle. Bundle consists of at least three nanotubes of diameters estimated to be 10 nm with a bundle height profile of approximately 20 nm

4.2.2. Raman Spectroscopy

Raman spectroscopy was performed with an excitation wavelength of 514 nm figure 4-7. The functionalized MWNTs exhibit well pronounced G and D-bands expected for MWNTs [**39**] with some disorder due to chemical treatment. The functionalized sample shows a large D-peak compared to the G-peak (I_D/I_G = 1.26), this is an indication of higher levels of disorder. The graphitic crystallite size between Raman active defects (L_a) in the samples is calculated using the Tuinstra Koenig relation [**39**] where $C(\lambda)$ is a constant that depends on the excitation wavelength. For λ= 514 nm, $C(\lambda) \sim 4.4$ nm.

$$\frac{I_D}{I_G} = \frac{C(\lambda)}{L_a}$$ (4-1)

It was found that the functionalized MWNTs have a crystallite size of 3.57 nm, in good agreement with Gd-DTPA functional group distribution observed in HRTEM. An upward shift of the Raman G-peak position is observed compared to the pristine MWNTs (1582 cm^{-1}). The shift in G-peak position of the Gd-functionalized sample is ($\Delta\omega_G$ = 7 cm^{-1}) and upon deconvolution it was determined that the asymmetry in the line width was due to the so-called

Figure 4-7 Raman spectrum for the functionalized composite material showing the deconvolution of the G and D peaks. The inset is an indication of the low wavenumber vibrational modes.

D′ peak situated at 1620 cm^{-1}. Like the D-peak, the D′ peak is an indication of disorder and commonly observed in functionalized MWNTs. The width of the G and D-peaks shows a broadening compared to the pristine spectrum, an increase in FWHM (G) is an indication of increased disorder [**39**]. As expected, the functi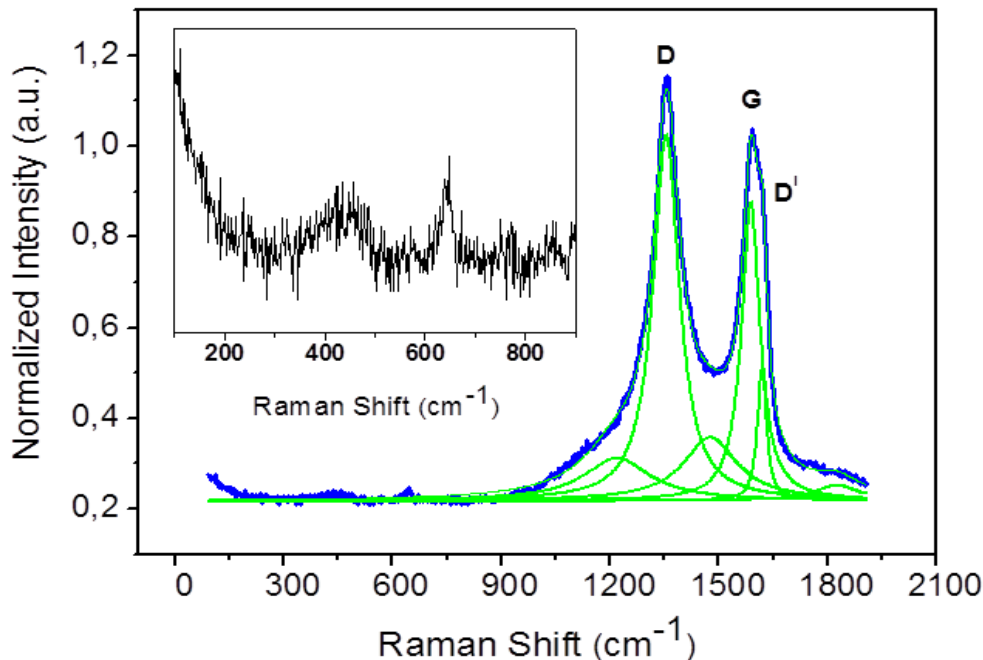onalized sample showing a high D-peak intensity also exhibits a high broadening of the G- and D-peaks. The deconvolution of the G and D-peaks of the functionalized sample also identified two broad low intensity bands situated at 1218 and 1476 cm^{-1}. The two features have been observed before in disordered graphite samples. The functionalized MWNT sample with the grafted Gd-DTPA complex on the outer tube wall also shows multiple peaks of small intensity between 200 and 1000 cm^{-1}. These peaks are expected to be a signature of the Gd complex attached to the tubes as they are not typical features of MWNT Raman spectrum. One notable low frequency feature observed is a small broad peak at around 400 cm^{-1}. It is possible that it is related to the gadolinium-carbon (Gd-C) coupling but will however require further investigation to determine its true origin.

4.3.   Magnetic Properties

Figure 4-8 shows the *M*(*H*) of Gd-DTPA-MWNTs. The nanocomposite exhibits a definite magnetic hysteretic behavior between forward and reverse field sweeps with a coercive field of 185 Oe and a magnetic remanence of approximately 0.013 emu/mol$_{Gd}$. The hysteresis area is often correlated with energy loss due to interactions between magnetic species or domains. The functionalized composite clearly demonstrates hysteresis closely related to a ferromagnet most likely due to the presence of the rare earth element

To further probe the nature of the magnetic behavior a study of the magnetic susceptibility was conducted between 300 and 1.7 K. Magnetization under field cooled (FC) and zero-field cooled (ZFC) procedures shows a difference in terms of curvature with decreasing temperature however the trend is qualitatively the same (figure 4-9). As mentioned in the introduction there are several reports on Gd incorporated carbon nanotubes, either through filling [**40**] or through chemical functionalization [**41,42**], which exhibit superparamagnetism. This is clearly not the case in this system as no blocking temperature can be identified in the susceptibility of the Gd-Fctn-MWNT composite shown in figure 4-9.

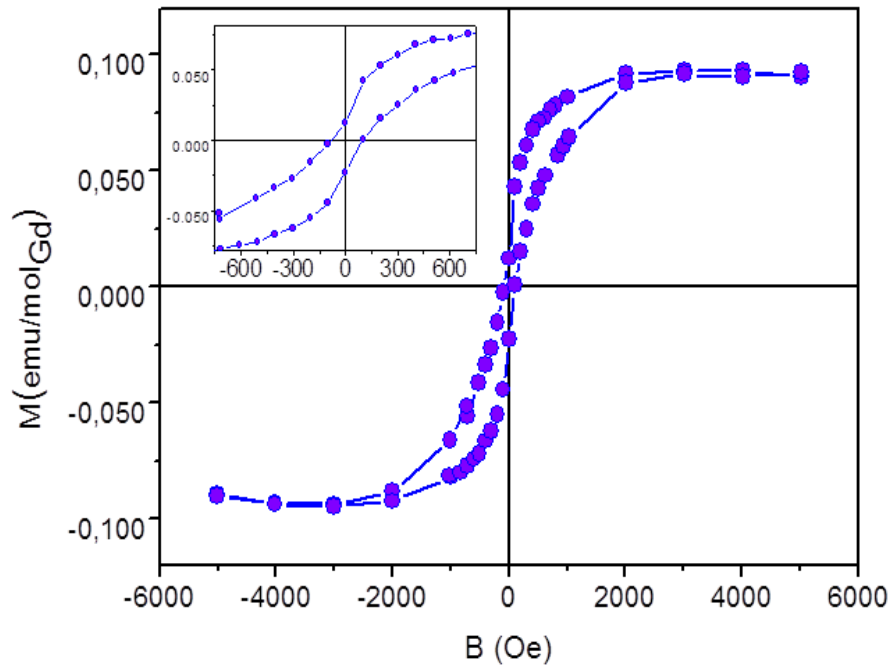Figure 4-8 Hysteretic behavior of Gd-Fctn-MWNT sample showing weakly ferromagnetic behavior. Inset: Magnified region demonstrating magnetic remanence and coercive field
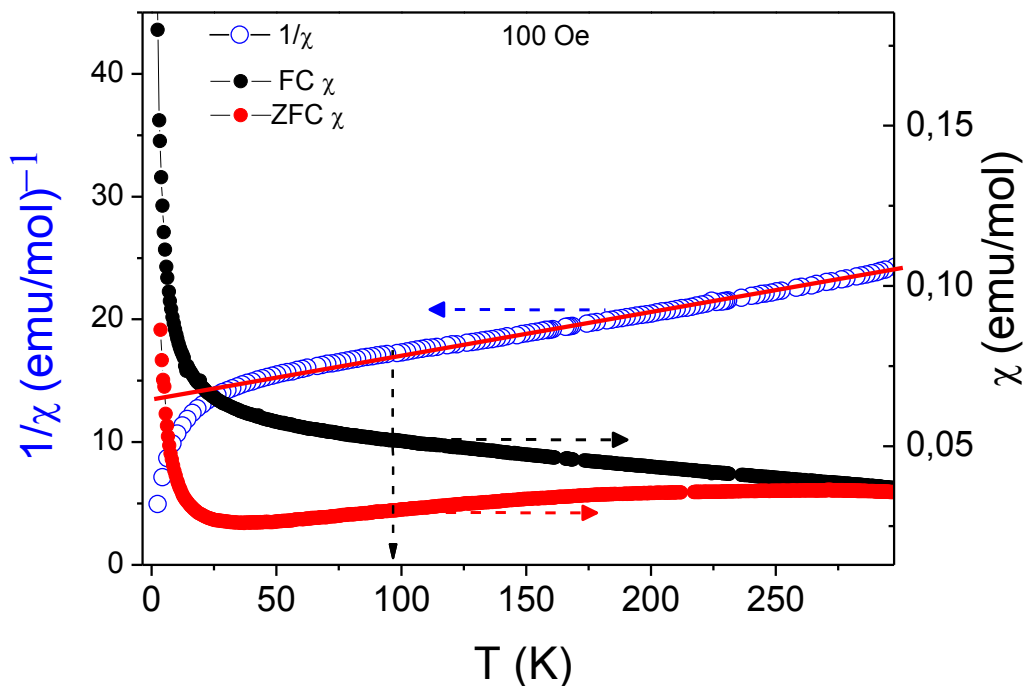

Figure 4-9 FC and ZFC susceptibility and inverse susceptibility plots for Gd-Ftcn-MWNT composite at 100 Oe showing paramagnetic behaviour and the corresponding inverse susceptibility for the FC data extrapolating to an antiferromagnetic exchange interaction.

.

The inverse susceptibility of the FC data set was plotted as a function of temperature to determine the coupling mechanism. The composite showed linearity down to 100 K after which the susceptibility increases (and inverse susceptibility decreases). By using the Curie-Weiss law (fitted to the linear part of the data in figure 4-9) a negative Weiss constant for the material was observed.

The functionalized MWNTs have a Weiss temperature of -413 K. In general (but not necessarily always) antiferromagnetic exchange (discussed in section 2.6.5) requires the existence of interaction between two spin sublattices of different spin orientation. In the system studied here the antiferromagnetic features are most likely due to interaction between the ferromagnetic Gd-DTPA complex and the diamagnetic MWNT. The conduction electrons of the nanotubes are likely candidates for mediating the antiferromagnetism via the RKKY interaction. When calculating the effective moment in terms of the molar concentration of the Gd^{3+}, which is determined from the elemental analysis, an enhanced effective moment of 15.79 μ_B was established. This value is much larger than the effective moment of the Gd-DTPA complex (8.7 μ_B see Appendix B). The large value reported here is a clear indication of interactions between the Gd-DTPA chelates along the MWNTs surface, this is likely a result from the close proximity of the $[Gd-DTPA]^{n+}$ entities which allows for complex aggregation with enhanced effective moment [40,41,42]. This aggregation is evident in the HRTEM as indicated in figure 4-5. Not surprisingly the effective moment calculated here is similar to that reported for supramolecular $Gd_3N@C_{80}$ (23 μ_B) where it was shown that Gd_3N clusters allow for ferromagnetic coupling and a largely enhanced moment [43]. It is believed a similar scenario is at play in the present study. These findings clearly demonstrate how the magnetic properties of a composite can be modified by controlling the chemical functionalization process.

4.4. Electronic Transport

Figure 4-10 shows the *I-V* characteristics of the Gd-DTPA-MWNT network device at various temperatures ranging from 300 mK to room temperature and the inset shows a typical device (6- electrode) used in this work; the Gd-Fctn-MWNT bundle deposited around the electrodes. *I-V* characteristics change progressively over the temperature range and a large deviation from

linearity is clearly seen at 300 mK. The strong nonlinearity is an indication of transport in the Coulomb blockade regime. The charging energy for a device with channel length of 1 µm is calculated to be 340 meV, which is roughly 10 times the value reported for single MWNT device and substantially larger than the thermal energy of the system at 300 mK (0.026 meV). The resistance of the device at this temperature was recorded to be approximately 300 kΩ (i.e. larger than the fundamental resistance quantum; 25.9 kΩ) and thus the requirements for the Coulomb blockade regime are met. The conductance was measured as a function of temperature for the same range and shows a steady increase to approximately 4 K and then saturates below this temperature, refer to figure 4-11. Analysis of the resistance vs. temperature data indicates that the Gd-DTPA-MWNT networks do not follow variable range hopping [16] (see Appendix A) which is the expected mechanism for thin CNT networks.

This was concluded after failure to linearize the logarithmic normalized conductance as a function of T^{β}, where β is a critical exponent representing the dimension scale of the hopping (Appendix A). The devices do however display similar trends to those reported for thicker SWNT networks [14] and conducting polymers [44.45] that suggests interrupted metallic conduction mediated by fluctuation induced tunnelling (FIT). A nonlinear fit to the data set gives a relation similar to that presented in ref 14.

$$\sigma(T) = \sigma_1 T + \sigma_2 e^{-\frac{T_1}{T+T_0}} \qquad (4\text{-}2)$$
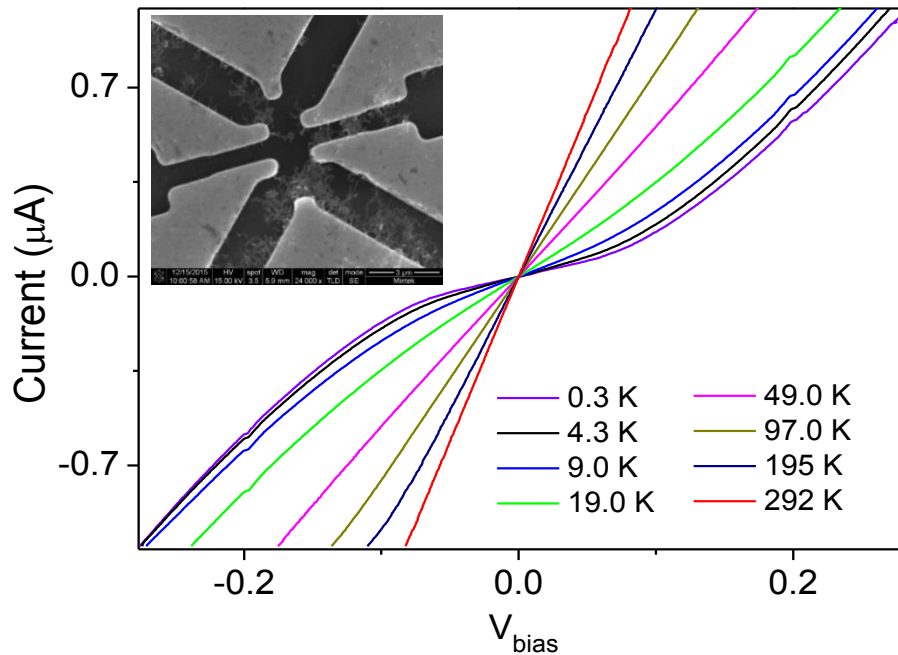
Figure 4-10 I-V sweeps from a temperature range of 300 mK up to 300 K. The inset is an SEM image of the device used

In this model the conductance is separated into two terms, the first term scales linearly with temperature whilst the second term takes into account the fluctuation assisted tunnelling [46]. Here σ_1 and σ_2 are temperature independent constants and T_1 represents the activation energy required to tunnel through the barriers and T_0 is the temperature at which the crossover from the saturating to activated transport occurs. This model has been successfully utilized in a range of disordered carbon networks. It should also be noted that there exist some reports [47] on a combined FIT/VRH model which introduces a VRH term instead of the linear term in equation 2, as presented in the Appendix A this does not fit as well to our data set. It should also be noted that some studies have linked the saturation in the resistance at low temperature to tunnelling between outer and secondary shells of the MWNT [14], however, due to the strong magnetic response and *I-V* analysis it is believed in this system that the low temperature behavior is due to electron and spin correlations.
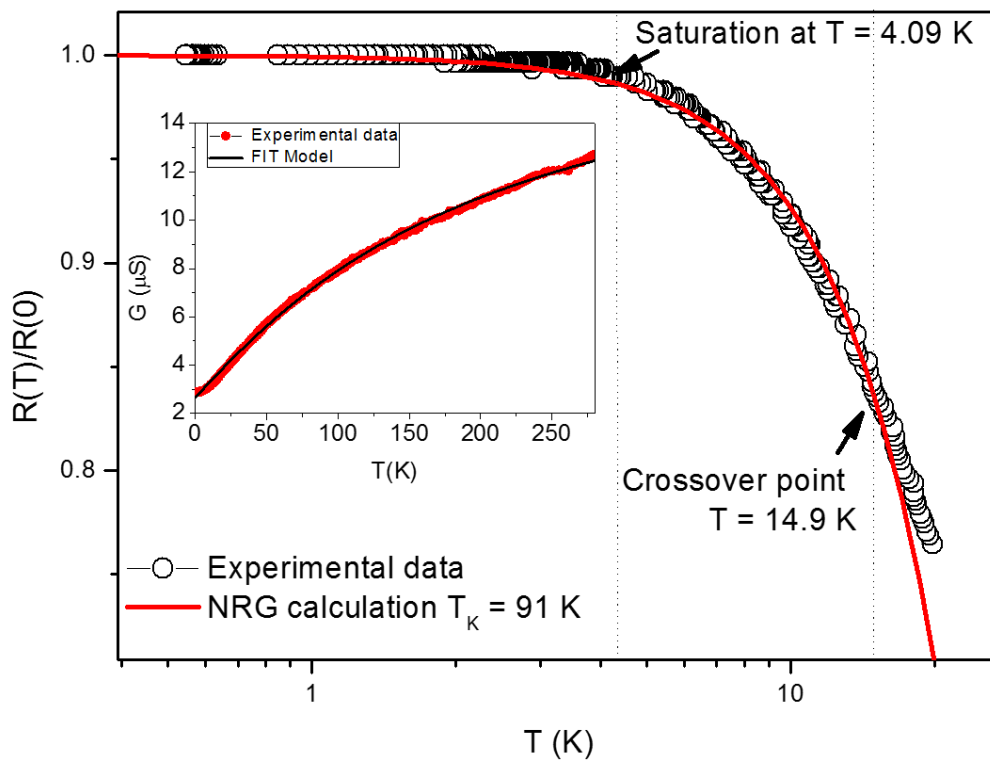
Figure 4-11 Temperature dependent normalized resistance showing a steady increase as temperature decreases and eventual saturation from 4 K, the red line is a fit to equation 3. The inset shows the conductance as function of temperature up to 300 K, the red line is a fit to equation 2 which deviates at low temperatures.

This led to probing the saturating resistance considering the numerical renormalized group (NRG) calculation as presented in figure 4-11 which shows the normalized resistance (with respect to the saturation resistance) as a function of temperature. A clear saturation is observed below approximately 4 K. The solid red line is a fit to the numerical renormalization group equation where $c = 6.088$ and T_K is the Kondo temperature.

$$\frac{R(T)}{R(0)} = \left(1 - c\left(\frac{T}{T_K}\right)^2\right)$$

(4-3)

From the fitting $T_K = 91$ K is extracted, although surprisingly high this value is very similar to what has recently been observed in disordered graphene using the same fitting. Additionally, it is observed that the equation fits the data set best in the region below 10 K, signifying the crossover from thermally activated transport mechanism (FIT fitting) at higher temperatures. The crossover temperature is significant due to observations in the differential conductance as shown in Figure 4-12.
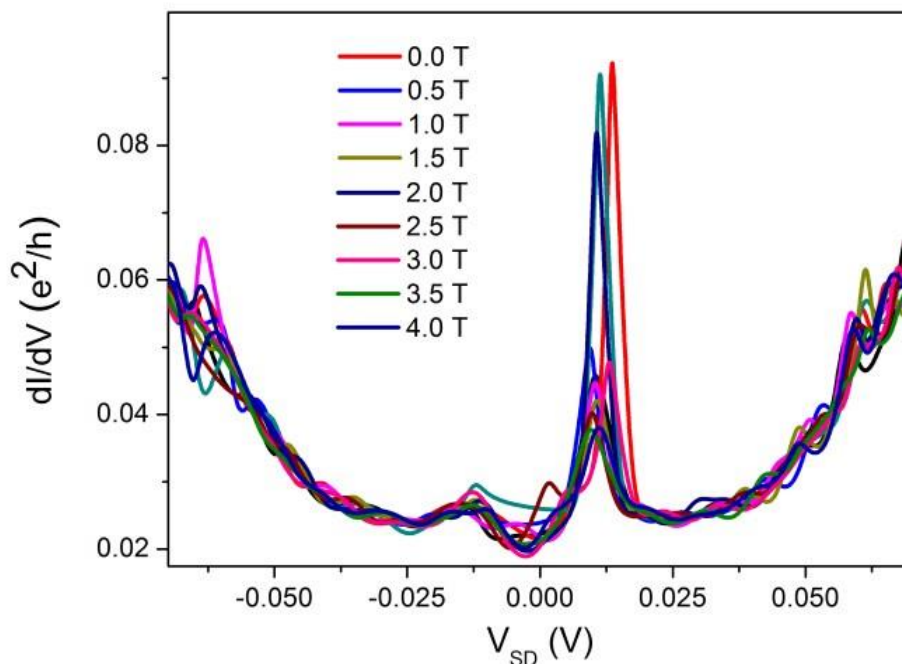
Figure 4-14 dI/dV for the device at various magnetic fields showing non zero resonance peaks near the zero bias at 300 mK

The *dI/dV* vs V_{SD} (source-drain voltage) shows a gapped region from between -0.05 to 0.05 eV shown in figure 4-12. Near the zero-bias point resonance like features are observed which have not been reported in previous studies on pristine MWNTs. These resonance peaks are strongly
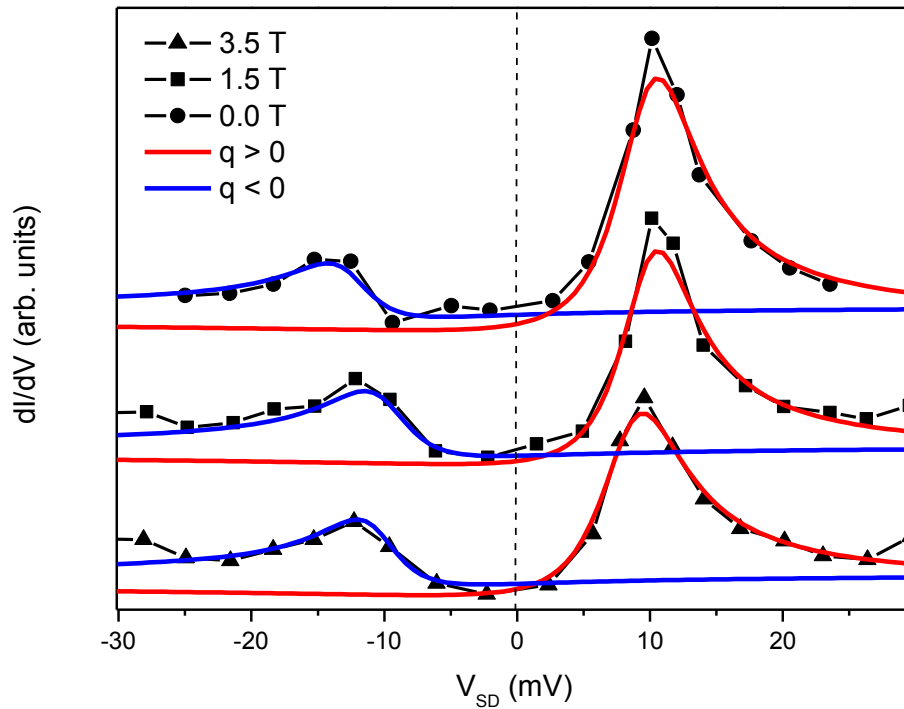
Figure 4-15 The dI/dV peaks fitted to the Fano formula (red and blue lines) for different Fano parameters (q values) at 300 mK.

temperature dependent and only appear in the temperature region below 15 K. The peaks are located at approximately +/-30 mV and are asymmetric and robust, these peaks are observed at all temperatures below 15 K. Additionally the asymmetry in the resonant peaks have lead to investigate the possibility of Fano-Kondo resonance in this system. Figure 4-13 shows a fitting of the Fano formula ref:

$$\frac{dI}{dV} \sim \frac{(\varepsilon+q)^2}{\varepsilon^2+1}$$

(4-4)

In equation 4, ε is related to the width and energy of the resonance, q is the Fano parameter which is related to the asymmetry of the peaks. The Fano formula is a good fit to the 10 mV peaks and have tracked these peaks as a function of applied field. The position and width of

the peaks are fairly constant as field is increased up to 3.5 T but notice a decrease in dI/dV peak height. From the width of the FWHM resonance T_K = 81 - 90 K (range of values obtained for data shown in Fig 4-13 see Appendix C for detailed analysis) is calculated, in close agreement to the value arrived at through the NRG fitting. Such features are most commonly attributed to Kondo resonances [48] which arise due to the interaction between localized spins ([Gd-DTPA]$^{n+}$) and the electrons of the surrounding host (MWNT). It was also observed that the peaks are strongly affected by the strength of the field, some of which increase in intensity whilst others diminish with increasing magnetic field.

As the conduction is weakened at lower temperatures, probably due to the Coulomb blockade effect, the RKKY exchange interaction will be suppressed [49] essentially freezing the spin on the Gd-DTPA molecule and thus lead to more stable magnetic tunnel barriers which may lead to the observed resonance states. The RKKY is a fundamental exchange that persists at all temperatures It becomes less visible due to other prevailing energies of interaction like the Coulomb blockade effect in this case. It should be noted that such resonance peaks are commonly observed only with STM measurements [50] over single magnetic impurities, or for

Figure 4-16 Magneto-resistance switching for the Gd-functionalized MWNT device passing a current of 10 μA at 300 mK. The switching is asymmetric with respect to forward and reverse field sweeps and multiple switching events occur; similar to non-local spin valve behavior

.

.

quantum dot devices, their presence in this network device is thus one of the first demonstrations of Kondo effect in a mesoscopic carbon network system and are thus rather significant.

In order to further probe the magnetic properties of the composite material the dependence of the resistance on the magnetic field is investigated as shown in figure 4-14. The spin switching effect is clearly observed at 300 mK showing symmetry about the zero bias, observed as the same values for the increase in resistance at different values of the of the magnetic field for forward and reverse bias for 2-terminal devices. Similar results have been reported for CNT devices fabricated with multiple nonlocal ferromagnetic contacts [26], where it was shown that
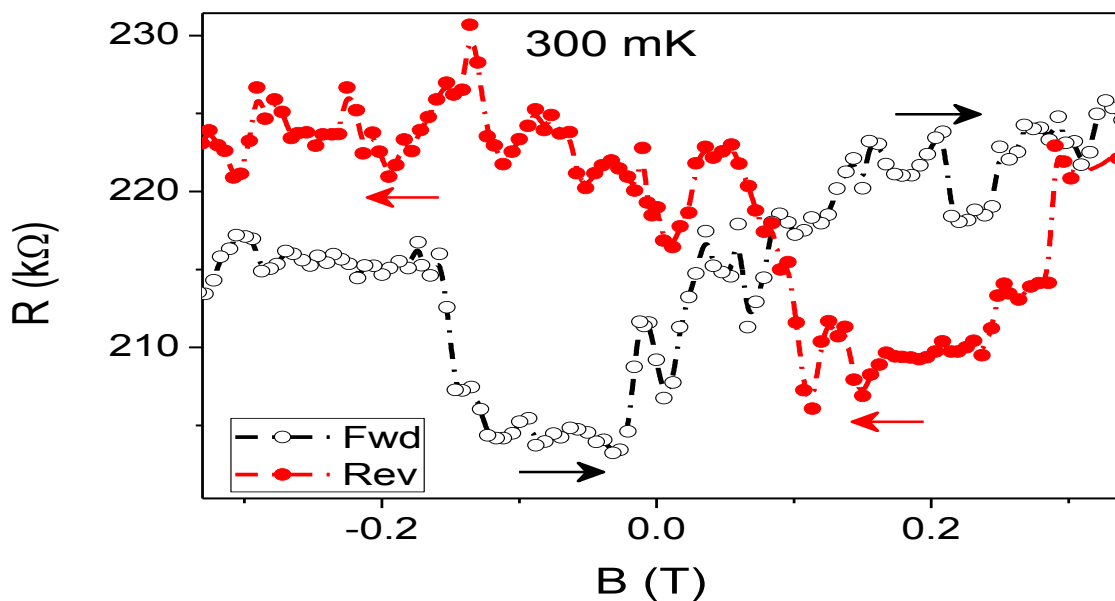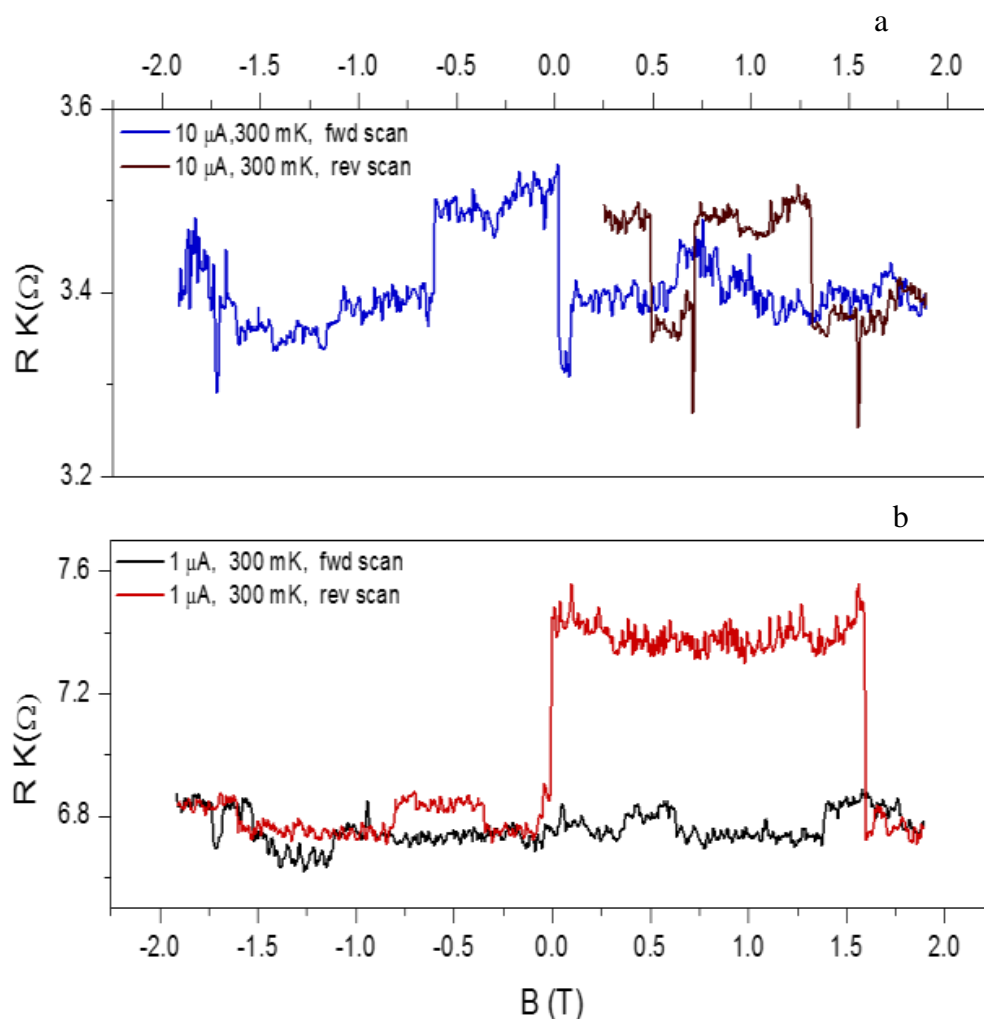

Figure 4-17 Magnetoresistance switching for the Gd-functionalized MWNT device passing a current of 10 µA. The switching is asymmetric with respect to forward and reverse field sweeps and multiple switching events occur; similar to non-local spin valve behavior. (b) There is a large increase in switching effect, roughly 7%, when current is lowered to 1 µA.

the orientation of the different ferromagnetic contacts can change the switching fields and magnetoresistance difference quite drastically. In order to further probe the nature of the spin switching effect the influence of current strength was considered as shown in figure 4-15. There are a few noteworthy features such as: multiple switching at various field strengths and asymmetry in the forward and reverse sweeps. As the Gd-functionalized MWNTs have many magnetic domains along the length of the tubes, it is not surprising that the multiple switching effect is observed, this indicates that interaction and alignment between adjacent magnetic domains are important when analysing the observed jumps in the resistance. It was found that when passing a current of 10 µA, the largest magnetoresistance jump was around 3%, also notable were the step like features in some of the jumps which have been observed before and are attributed to sequential tunneling (figure 4-15). When the current is lowered to 1 µA a large increase in the TMR to about 7.5% (figure 4-15) was observed.

At the lower current it is expected that the Coulomb blockade effect is stronger due to lower electron temperature. This ensures the system is more resistive than at higher currents due to stronger Coulomb repulsion. In this state, it is expected that co-tunneling effects dominate over ground state sequential tunneling [15,16,17]; this second order co-tunneling process takes place through a virtual intermediate state and is known to enhance TMR [16,17] as observed in the device.

Figure 4-19 A schematic representing how neighboring Gd-DTPA complexes can act as spin valve barriers effectively preventing or promoting transport of conduction electrons depending on local spin densities coupled to the Gd-DTPA complex in conjuction with the TMR effect shown in Figure 10.

The enhancement of TMR due to co-tunneling is a result of spin accumulation, whereby an imbalance in the densities of states in the antiferromagnetic configurat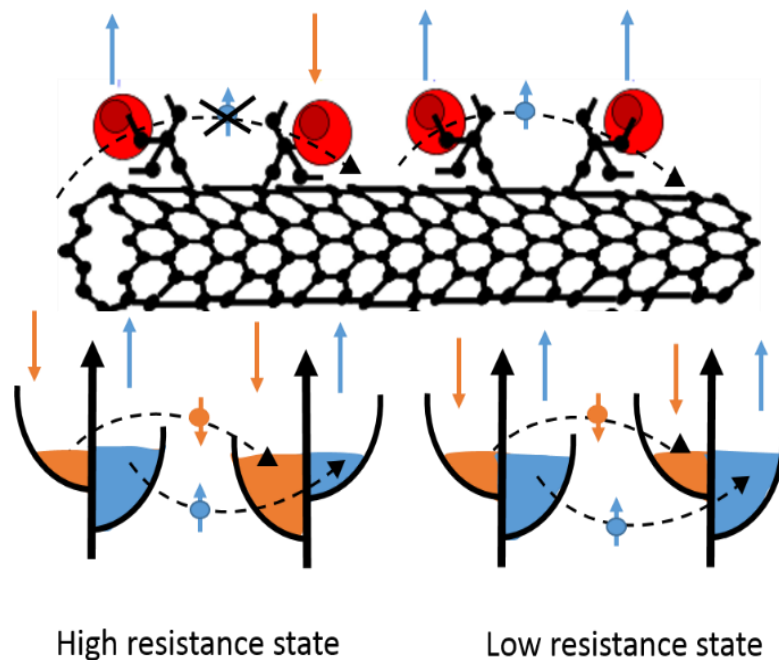ion occurs due to preferred tunneling of one spin state over the other. When a field is applied to the system, the densities of state for the two regions will shift, this results in spin flipping of states above the chemical potential [16] as shown schematically in figure 4-16. However, nonlocal measurements must be performed on such spin systems to separate features relating to the Magneto-Coulomb effect and spin accumulation [51, 52] as both show similar features. Such measurements are yet to be conducted on the samples studied in this work. Another seemingly anomalous observation in the magnetoresistance is the shifting of switching fields; as indicated by the susceptibility analysis there is antiferromagnetic coupling in the system. It is well known that exchange bias can cause the shifting of switching fields in spin valves and again this hints at inter-domain interaction, this coupled to possible spin accumulation from the cotunneling events leads to changes in the local magnetic moment and field of single domains, further tunneling into or out of a domain can have a cascading effect and lead to spin flipping which can enhance or reduce the resistance. This work has been published in the Scientific reports journal titled 'Kondo effect and enhanced magnetic properties in gadolinium functionalized carbon nanotube supramolecular complex.'

References

1   M. Bockrath, D.H. Cobden, J. Lu, A.G. Rinzler, R.E. Smalley, L. Balents and P.L. McEuen. Nature, **397**, 598 (1999).

2   S. Ncube, G. Chimowa, Z. Chiguvare and S. Bhattacharyya. J. Appl. Phys, **116**, 024306 (2014).

3   G. Chimowa, S. Ncube and S, Bhattacharyya. Euro. Phys. Lett, **111**, 3 (2015).

4   R. Leturcq, C. Stampfer, K. Inderbitzin, L. Durrer, C. Hierold, E. Mariani, M.G. Schultz, F. von Oppen and K. Ensslin. Nat. Phys, **5**, 327 (2009).

5   H.W. Ch. Postma, T. Teepen, Z. Yao, M. Grifoni and C. Dekker. Science, **6**, 293 (2001).

6   Z. Yao, H.W. Ch. Postma, L. Balents, and C. Dekker. Nature, **402**, 273-276 (1999).

7   P. Jarillo-Herrero, J. Kong, H.S.J. van der Zant, C. Dekker, L.P. Kouwenhoven and S. De Franceschi. Nature, **434**, 484 (2005).

8   J. Nygård, D.H. Cobden and P.E. Lindelof.   Nature, **408**, 342(2000).

9   J. Paaske, A. Rosch, P. Wölfle, N. Mason, C. M. Marcus, and J. Nygård. Nat. Phys, **2**, 460 (2006).

10   J-D. Pillet, C.H.L. Quay, P. Morfin, C. Bena, A. Levy Yeyati and P. Joyez. Nat. Phys, **6**, 965 (2010).

11   J.-P. Cleuziou, W. Wernsdorfer, V. Bouchiat, T. Ondarçuhu, and M. Monthioux. Nat. Nanotechnol., **1**, 53 (2006).

12   R.M. Potok, I.G. Rau, H. Shtrikman, Y. Oreg and D. Goldhaber-Gordon. Nature, **446**, 167 (2007).

13   V. Mourik, K. Zuo, S.M. Frolov, S.R Plissard, E.P. Bakkers, and L.P. Kouwenhoven. Science, **336**, 1003(2012).

14   C. Gómez-Navarro, P.J. De Pablo, J. Gómez-Herrero, B. Biel, F.J. Garcia-Vidal, A. Rubio and F. Flores. Nature Materials, **4**, 534 (2005); A. Bachtold, C. Strunk, J.-P. Salvetat, J.-M. Bonard, L. Forró, T. Nussbaumer, and C. Schönenberger. Nature, **397**, 673-675 (1999); V. Skakalova, A.B Kaiser, Y.-S. Woo and S. Roth. Phys. Rev. B, **74**, 085403 (2006).

15   R. Schleser, T. Ihn, E. Ruh, K. Ensslin, M. Tews, D. Pfannkuche, D.C. Driscoll and A. C. Gossard. Phys. Rev. Lett, **94**, 206805 (2005).

16   H. Imamura, S. Takahashi and S. Maekawa. Phys. Rev. B, **59**, 6017 (1999).

17   S. Takahashi and S. Maekawa. Phys. Rev. Lett, **80**, 1758 (1998).

18   T. Ida, K. Ishibashi, K. Tsukagoshi, Y. Aoyagi and B.W. Alphenaar. Superlattices Microstruct, **27**, 551-554 (2000).

19   Y. Nakai, R. Tsukada, Y. Miyata, T. Saito, K. Hata, and Y. Maniwa. Phys. Rev. B, **92**, 1 (2015).

20   A.A. Ovchinnikov and V.V. Atrazhev. Phys. Solid State, **40**, 1769 (1998).

21   F. Tsui, L. Jin and O. Zhou. Appl. Phys. Lett, **76**, 1452 (2000).

22   S. Zaric, G.N. Ostojic, J. Kono, J. Shaver, V.C. Moore, R.H. Hauge, R.E. Smalley and X. Wei. Nano Lett, **4**, 2219 (2004).

23   K. Tsukagoshi, B.W. Alphenaar, and H. Ago. Nature, **401**, 572 (1999).

24   J. Li and Y. Zhang. Phys. E Low-Dimensional Syst. Nanostructures, **28**, 309 (2005).

25   C. Meyer, C. Morgan, and C.M. Schneider. Phys. Status Solidi Basic Res, **248**, 2680 (2011).

26   H. Yang, M.E. Itkis, R. Moriya, C. Rettner, J.-S. Jeong, D.S. Pickard, R.C. Haddon and S.P. Parkin. Phys. Rev. B, **85**, 052401 (2012).

27   B. Zhao, I. Monch, H. Vinzelberg, T. Muhl and C. M. Schneider. App. Phys. Lett., **80**, 3114 (2002).

28   R. M. Langford, M. J. Thornton, T. X. Wang, W. Blau, B. Lassagne and B. Raquet. Microelectronic Engineering, **84**, 1593 (2007).

29   M. Urdampilleta, S. Klyatskaya, J.-P. Cleuziou, M. Ruben, and W. Wernsdorfer. Nat. Mater., **10**, 502 (2011).

30   M. Ganzhorn, S. Klyatskaya, M. Ruben, and W. Wernsdorfer. Nat. Nanotechnol, **8**, 165 (2013).

31   L. Bogani and W. Wernsdorfer. Nat. Mater., **7**, 179 (2008).

32   I. Marangon, C. Ménard-Moyon, J. Kolosnjaj-Tabi, M. L. Béoutis, L. Lartigue, D. Alloyeau, E. Pach, B. Ballesteros, G. Autret, T. Ninjbadgar, D. F. Brougham, A. Bianco and F. Gazeau. Adv. Funct. Mater, **24**, 7173 (2014).

33   G. Che, B. B. Lakshmi, E. R. Fisher and C. R. Martin. Langmuir, **15**, 750758 (1999).

34   A. Leonhardt, M. Ritschel, R. Kozhuharova, A. Graff, T. Mühl, R. Huhle, I. Mönch, D. Elefant and C. M. Schneider. Diam. Relat. Mater., **12**, 790 (2003).

35   E. C. Linganiso, G. Chimowa, P. J. Franklyn, S. Bhattacharyya and N. J. Coville. Mater. Chem. Phys., **132**, 300 (2012).

36   B. Sitharaman, K. R. Kissell, K. B. Hartman, L. A. Tran, A. Baikalov, I. Rusakova, Y. Sun, H. A. Khant, S. J. Ludtke, W. Chiu, S. Laus, E. Toth, L. Helm, A. E. Merbach and L. J. Wilson. Chem. Commun. (Cambridge), **31**, 3915 (2005).

37   A. Quetz, I. Dubenko, T. Samanta, H. Vinson, S. Talapatra, N. Ali, and S. Stadler. J. Appl. Phys., **113**, 17B512 (2013).

38   C. Schönenberger, A. Bachtold, C. Strunk, J. P. Salvetat, and L. Forró. Appl. Phys. A Mater. Sci. Process, **69**, 283 (1999).

39   F. Tuinstra and J. L. Koenig. J. Phys. Chem., **53**, 1126 (1970).

40   J. S. Ananta, M. L. Matson, A. M. Tang, T. Mandal, S. Lin, K. Wong, S. T. Wong and L. J. Wilson. J. Phys. Chem. C, **113**, 19365 (2009).

41   A. Servant, I. Jacobs, C. Bussy, C. Fabbro, T. da Ros, E. Pach, B. Ballesteros, M. Prato, K. Nicolay and K. Kostarelos. Carbon, **97**, 126(2016).

42   B. Sitharaman, B. D. Jacobson, Y. Z. Wadghiri, H. Bryant and J. Frank. J. Appl. Phys., **113**, 134308 (2013).

43   B. Nafradi, A. Antal, A. Pasztor, L. Forro, L. F. Kiss, T. Feher, E. Kovats, S. Pekker and A. Janossy. J. Phys. Chem. Lett., **3**, 3291(2012).

44   P.Sheng, E. K. Sichel and J. I. Gittleman. Phys. Rev. Lett., **40**, 18 (1978).

45   P. Sheng. Phys. Rev. B, **21**, 2180(1980).

46   M. Salvato, M. Cirillo, M. Lucci, S. Orlanducci, I. Ottaviani, M. L. Terranova and F. Toschi. Phys. Rev. Lett., **101**, 246804 (2008).

47   R. Kamalakannan, , K. Ganesan, S. Ilango, N. Thirumurugan, V. N. Singh, M. Kamruddin, B. R. Mehta and A. K. Tyagi. Appl. Phys. Lett., **98**, 192105 (2011).

48   F. Simmel, R. H. Blick, J. P. Kotthaus, W. Wegscheider, and M. Bichler. Phys. Rev. Lett., **83**, 2636(1999).

49   A. Allerdt, A. E. Feiguin and S. Das Sarma. Phys. Rev. B, **95**, 104402 (2017).

50   Lam H. Yu and Douglas Natelson. Nano Lett., **4**, 79(2004).

51   N. Tombros, S. J. van der Molen and B. J. van Wees. Phys. Rev. B, **73**, 233403 (2006).

52   S. J. van der Molen, N. Tombros and B. J. van Wees. Phys. Rev. B, **73**, 220406 (R) (2006).

5. Magnetotransport in Gadolinium Chloride Filled Multi Walled Carbon Nanotubes

5.1.   Introduction

Filling of CNTs with ferromagnetic materials has been attempted over a long time in order to improve their magnetic properties which has been largely unsucessful for nanoelectronic applications due to the lack of observation of Kondo effect and cotunnelling. Various efforts have been made to invesigate the competition between the many-body Kondo effect and other co existing phenomena like cotunnelling, RKKY interaction and superconductivity [1,2,3,4] in strongly interacting correlated electron systems. The co-existence of these phenomena gives rise to new device functionalities and a prospect to explore the atypical physics [5,6,7,8]. A material which possesses the quantum charge transfer properties, magnetic and semiconducting in nature can be explored. Modified CNTs are ideal platforms for this study as they have already been extensively researched as quantum dots for quantum computing and spintronic applications [9,10,11]. The rich chemistry of carbon has allowed for the chemical modification and tailoring of CNT properties by attaching desired supramolecular complexes through either a covalent or pi-pi stacking mechanisms [12,13] and filling with nanomagnets [14]. Conventional spintronic devices are fabricated using such modified materials or with pristine MWNTs contacted to ferromagnetic leads [13,15,16]. There is however another modification route that has to date not been thoroughly investigated for spintronic application; filling of MWNTs with magnetic materials. Filling of MWNTs has been shown to preserve the magnetic nanoparticles from oxidation hence the magnetic properties are retained ensuring long term stability. It has been shown that upon modification with magnetic materials the magnetotransport properties of CNT are considerably affected and become sensitive to the magnetic state of the modifying elements [17]. Due to their low dimensional nature and high aspect ratio the combination of CNTs and magnetic entities can give rise to exotic features like enhanced transport features known as the Luttinger liquid behaviour, Kondo effect [4] which is known to arise when a localized magnetic impurity interacts with the spin of the conduction electrons of a non-magnetic metallic host. In this chapter the study of devices fabricated from networks of $GdCl_3$ filled MWNTs is presented. At nanoscale the Kondo effect has been observed in individual CNTs, quantum dots, individual molecules and quantum point contacts by direct probing of the local density of states using scanning tunnelling microscopy (STM) [19,20,21]. SWNTs decorated with cobalt nanoclusters exhibit Kondo resonances observed as

a narrow peak in the differential conductance near the Fermi level [**22**]. Emergence of Kondo resonances in the conductance and cotunelling effects in devices fabricated from a bundle of $GdCl_3$ MWNTs is shown in this chapter. This is explained by the device architecture employed and multichannel effect dominant in bundles. The $GdCl_3$ MWNTs exhibit a superparamagnetic transition at low temperatures and the Kondo to cotunelling transition is related to the blocking temperature.

5.2.   Raman analysis and Sructural Characterization

HRTEM of the filled MWNTs (figure 5-1) reveals the presence of discontinuous rod-like nanostructures in the core of the innermost tube with an approximate length of 10-30 nm. The $GdCl_3$-filled MWNTs contain approximately 0.26% mass cobalt with a concentration of 1.08 % gadolinium from ICP-OES analysis. Pristine MWNTs from the synthesis mentioned above were also analyzed and found to contain 0.54 % Co and 1.66 % Mo mass, this was measured to establish the concentration of catalyst impurities before filling.
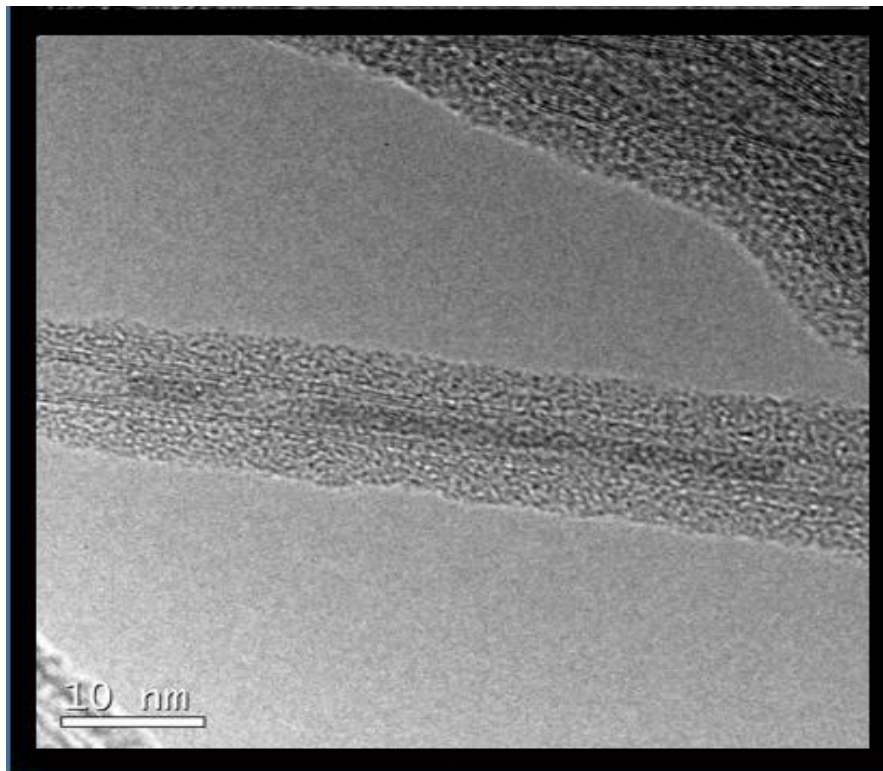

Figure 5-1 HRTEM image of $GdCl_3$ filled MWNTs showing rod like structures inside the innermost tube

The Tuinstra Koenig equation as indicated in the previous chapter [**23**] was used to calculate the crystalite size of 13.33 nm from the Raman studies (figure 5-2) for the 20 nm diameter. An upward shift of the Raman G-peak position when compared to the pristine MWNTs (1582 cm^{-1}) of 5 cm^{-1} is similar to what has been reported for SWNT filled with CoBr$_2$ [**24,25**] hence the shift in G-peak was believed to be a result of acceptor doping. Upon deconvolution it was established that the G-peak could be split into two components identified as G$^+$ and G$^-$ which correspond to vibrational modes along nanotube axis and around circumferential direction respectivly. The increased width of the Raman G and D-peaks was taken as an indication of increased disorder [**14**]. In addition to the expected D and G-band, the Raman spectrum of the filled tubes show multiple small sharp peaks at low Raman wavenumbers, although peaks in this range have been observed in SWNTs, DWNTs [**26,27**] and MWNTs prepared using arc discharge synthesis route [**28**]. These peaks are generally attributed to the radial breathing modes (RBM) of CNTs and are not expected in CVD synthesized MWNTs due to confinement effects of the multiple walls of the CNTs. The observation of peaks
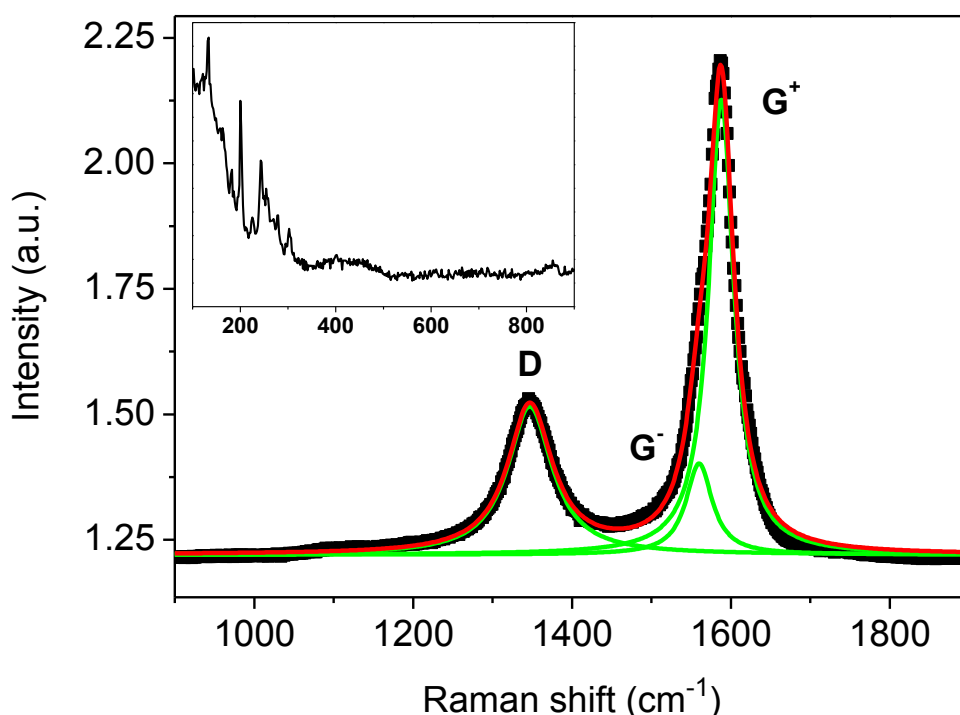

Figure 5 2 Raman spectra of GdCl$_3$-filled MWNTs, exhibits spectrum for low disordered CNTs with pronounced G-band and small ID/IG ratio. Convolution shows the G-band can be split into two sub-peaks. D band intensity remains low.

in the range 50–200 cm^{-1} are thus believed to be related to the four vibrational modes of GdCl$_3$ which are expected to occur at 93, 185, 199 and 230 cm^{-1} which have been observed for other lanthanide-trichloride samples [29,30,31,32,].

5.3.   Superparamagnetism in GdCl$_3$ filled MWNTs

The GdCl$_3$-filled MWNTs showed magnetic remanence and coercive field that is almost zero as shown in figure 5-3, where the inset shows the weak ferromagnetism from Gd-Fctn-MWNT. The hysteresis is an indication of a long range magnetic dipole-dipole interaction among the assemblies of superparamagnetic nanoparticles. From literature Gd modified CNTs, filled or functionalization, exhibit superparamagnetism [33,34]. The hallmark of this effect is the bifurcation observed FC susceptibility as shown in figure 5-4. This is observed only in the filled tubes indicating the non-interaction of magnetic centres leading to superparamagnetism. The bifurcation starts at just above 100 K and upon decreasing the temperature the gap broadens to 30 K where a sudden downward turn is observed. Two significant temperatures were identified; the higher one is the bifurcation temperature that signifies the onset of the superparamagnetic phase and the second lower temperature is the blocking temperature. The broad transition is a result of inhomogeneity in the magnetic particle size and corresponds to different size particles having a range of blocking temperatures. The inverse of the ZFC susceptibility was plotted as a function of temperature to determine the coupling mechanism. The susceptibility of the filled MWNTs showed linearity down to near the determined blocking temperature and then decreases steeply.

By using the Curie-Weiss law (fitted to the linear part of the data) a negative Weiss constant of -90 K was obtained, indicating antiferromagnetic exchange interaction. Antiferromagnetic exchange interaction features, are most likely due to interaction between the paramagnetic, GdCl$_3$ and the diamagnetic MWNTs. The delocalized electrons of the nanotubes are likely candidates for mediating the antiferromagnetism via the RKKY interaction. There is a screening effect from outer walls which lowers the effective spin-electron interaction. This along with the fewer mediating conduction electrons is likely to be the cause of the smaller Weiss temperature observed in filled CNTs in comparison to Gd-Fctn MWNTs.
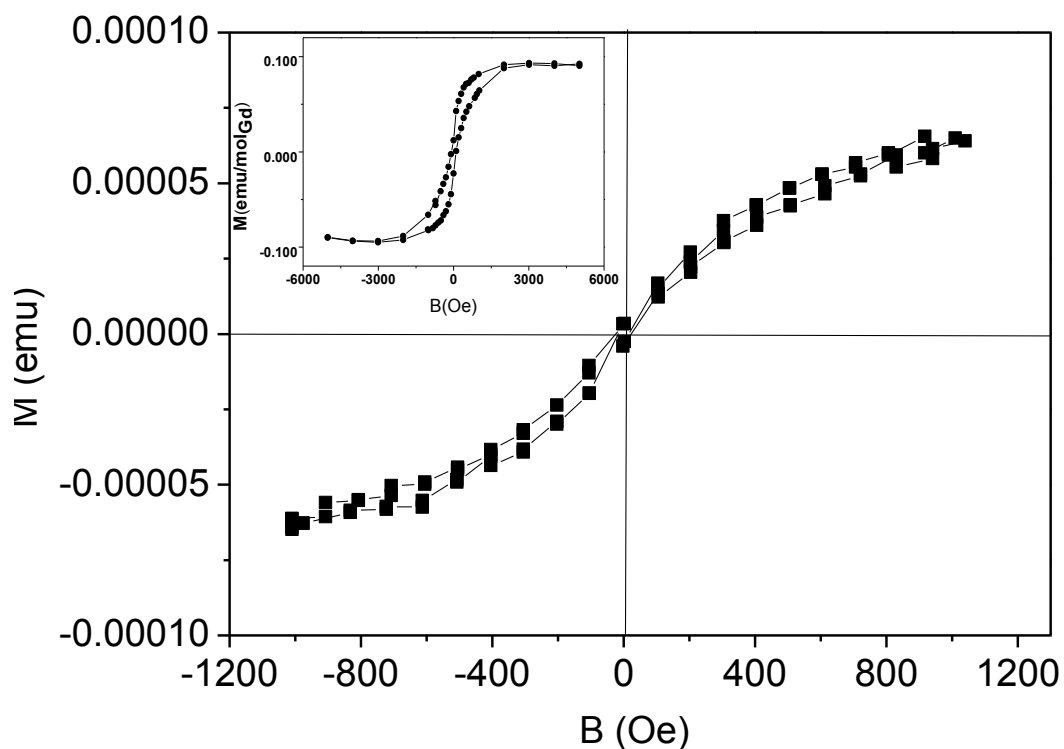
Figure 5-3 Hysteresis for the GdCl$_3$-filled MWNTs showing coercive field or remanence close to zero. The inset for the Gd-Fctn-MWNT for comparison.
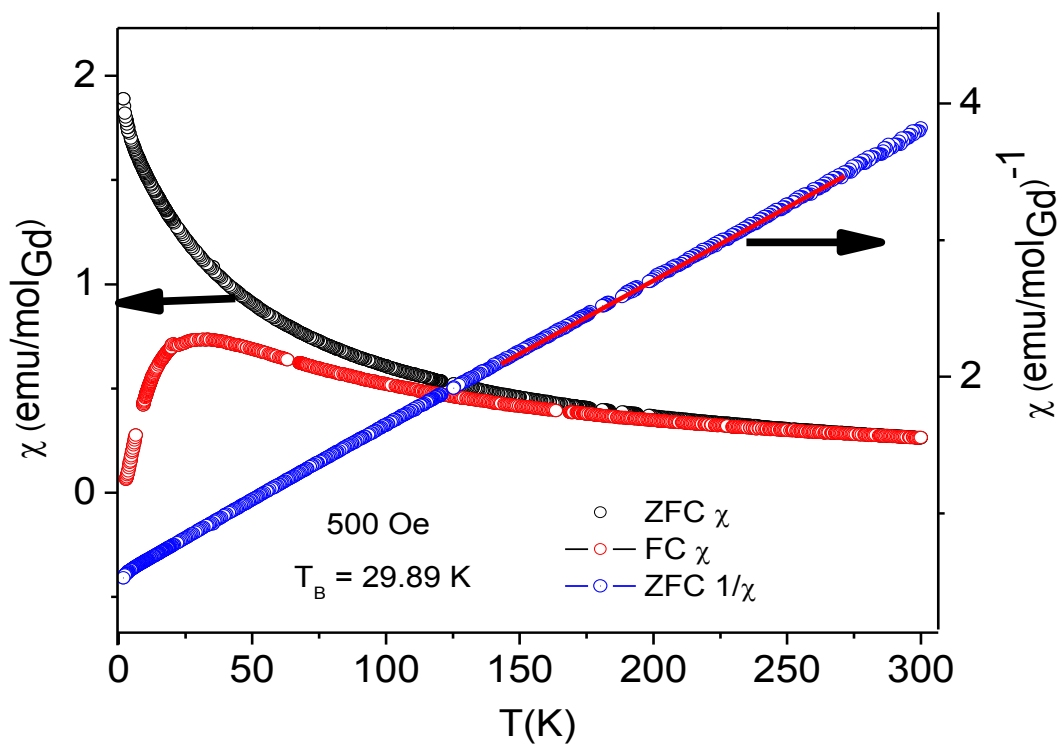

Figure 5-4 Molar susceptibility and inverse susceptibility plots for Gd -filled MWNTs showing a superparamagnetic transition at low temperatures in the ZFC data

Figure 5-4 shows the molar susceptibility plots used to determine the Weiss temperature and Curie constant, when calculating the effective moment in terms of the molar concentration of the Gd, this is determined from the elemental analysis. The effective moment is calculated to 20.9 μ_B showing an enhancement in comparison to the value free Gd^{3+} ion of 7.94 μ_B. The large values reported here are a clear indication of interactions between the $GdCl_3$ and electronic environment of the MWNTs.

A control study of pre-filled MWNTs was conducted, in order to establish any contribution resulting from catalyst impurities such as the Co which was determined to be present from the elemental analysis. Although the control does show a slight paramagnetic signature, the response is orders of magnitude weaker than the response of the modified MWNTs indicating that the dominant magnetic effects are a result of the filling of gadolinium species and not from catalyst impurities. Details on the pristine MWNT magnetic behaviour are presented in Appendix B.

5.4.   Electronic Transport

The increase in resistance down to 40 K has been analysed in light of Kondo scattering utilising the Fermi liquid description [35,36] which has recently been successfully used for graphene devices [37];

$$\rho(T) = \rho_{c1} + \rho_0 \left(1 - \left(\frac{T}{T_K} \right)^2 \right) \tag{5-1}$$

$$\rho(T) = \rho_{c2} + \frac{\rho_0}{2} \left(1 - 0.47 \ln \left(\frac{1.2T}{T_k} \right)^2 \right) \tag{5-2}$$

Equation 1 is valid for temperatures between resistance maxima up to approximately 150 K, where there is a change in transport mechanism that is described by equation 2. Both equations give a best fit to the data with a Kondo temperature of 137 K. The values of ρ_{c1} and ρ_{c2} have a discrepancy of within 12%, indicating self-consistency between the two equations. This model does not however explain the turning point in the *R-T* curve indicating that additional mechanisms are at play. Thus the Kondo temperature T_{K1} determined above is considered to be the temperature where Kondo scattering becomes significant (related to the bifurcation temperature observed in the susceptibility) or the onset Kondo effect.
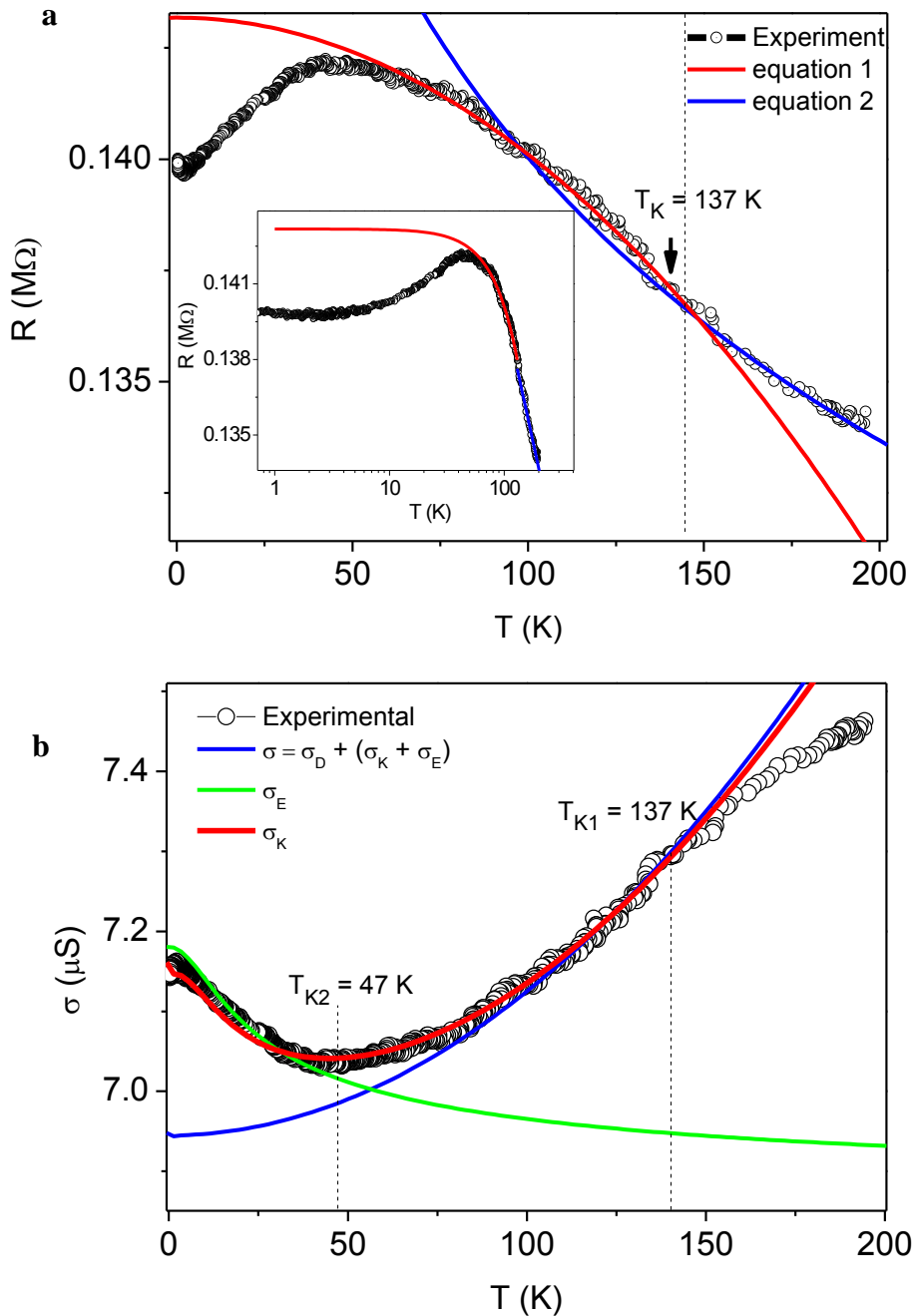
Figure 5-5 (a) The resistance as a function of temperature. (a) The red and blue lines are a fit to Eqs. (5-1) and (5-2), which yields a Kondo temperature of 137 K. The inset shows the same data plotted on a log T scale to highlight the various transport crossover regimes. (b) The conductance as a function of temperature for the GdCl$_3$-filled MWNT sample. Here, the conductance shows a minimum at around 40K and then increases sharply. The fitted curve is the interpolation formula given by equation 5-3. T_{K1} is the onset of the Kondo effect and T_{K2} is the actual Kondo temperature where the Kondo effect becomes dominant in electronic transport.

To establish the nature of decreasing low temperature resistance the conductivity data of the GdCl$_3$-filled MWNTs is analysed in light of interpolation scheme taking into account competition between the Kondo effect and co-tunnelling [38] which has been successfully used to describe MTJ with superparamagnetic particles embedded within the dielectric layer. As seen in Figure 5-5 (b), the red curve is a combination of the two interpolation formulae used to indicate the cross over from a co-tunnelling dominated to Kondo dominated regime this is given by;

$$\sigma = a\sigma_D + b(\sigma_E + \sigma_K)$$ (5-3)

with a + b = 1. In equation 3 σ_D is the direct tunnelling conductivity between the electrodes and has previously been neglected when using this model. In order to have a more realistic fit this study has related σ_D to a conductance offset determined from the fitting to be $\sigma_D = 6.6$ µS. This effectively sets the coefficients *a* and *b* as 0.75 and 0.25 respectively. σ_K represents a conductivity term involving the Kondo effect and σ_E is the elastic conductivity not including spin-flip events. According to Ref [39] the conductivity term associated with the Kondo effect takes the form:

$$\sigma_K = \sigma_0 \left(\frac{T_{K2}^2}{T^2 + T_{K2}^2}\right)^S ,$$ (5-4)

where

$$T_{K2}^2 = \frac{T_K}{\sqrt{2^{1/S}-1}}.$$ (5-5)

S ~ 0.2 and σ_0 is related to the occupancy of electron clusters near the magnetic particles within the tubes, for perfectly symmetric barriers it will have a value of $\sigma_0 \leq (2e^2)/h$. For these devices and σ_0 has a value of approximately 7×10^{-9} well within the expected range demonstrated by other magnetic tunnel junction devices is obtained. The elastic conductivity is given by a combination of sequential and co-tunneling conductance terms, which take the form:

$$\sigma_{cot} = \frac{2h}{3e^2}\frac{1}{R_T^2}\left(\frac{k_BT}{E_C}\right)^2 ; \text{(5-6a)} \qquad \sigma_{seq} = \frac{1}{2R_T^2}\left(1 + \frac{E_C}{k_BT}\right)^{-1} \text{(5-6b)}$$

Here R$_T$ is the tunnelling resistance between electrodes and MWNT network, this quantity is determined from equation (6b) to be R$_T$ = 5.3 kΩ which is slightly higher but of the same order
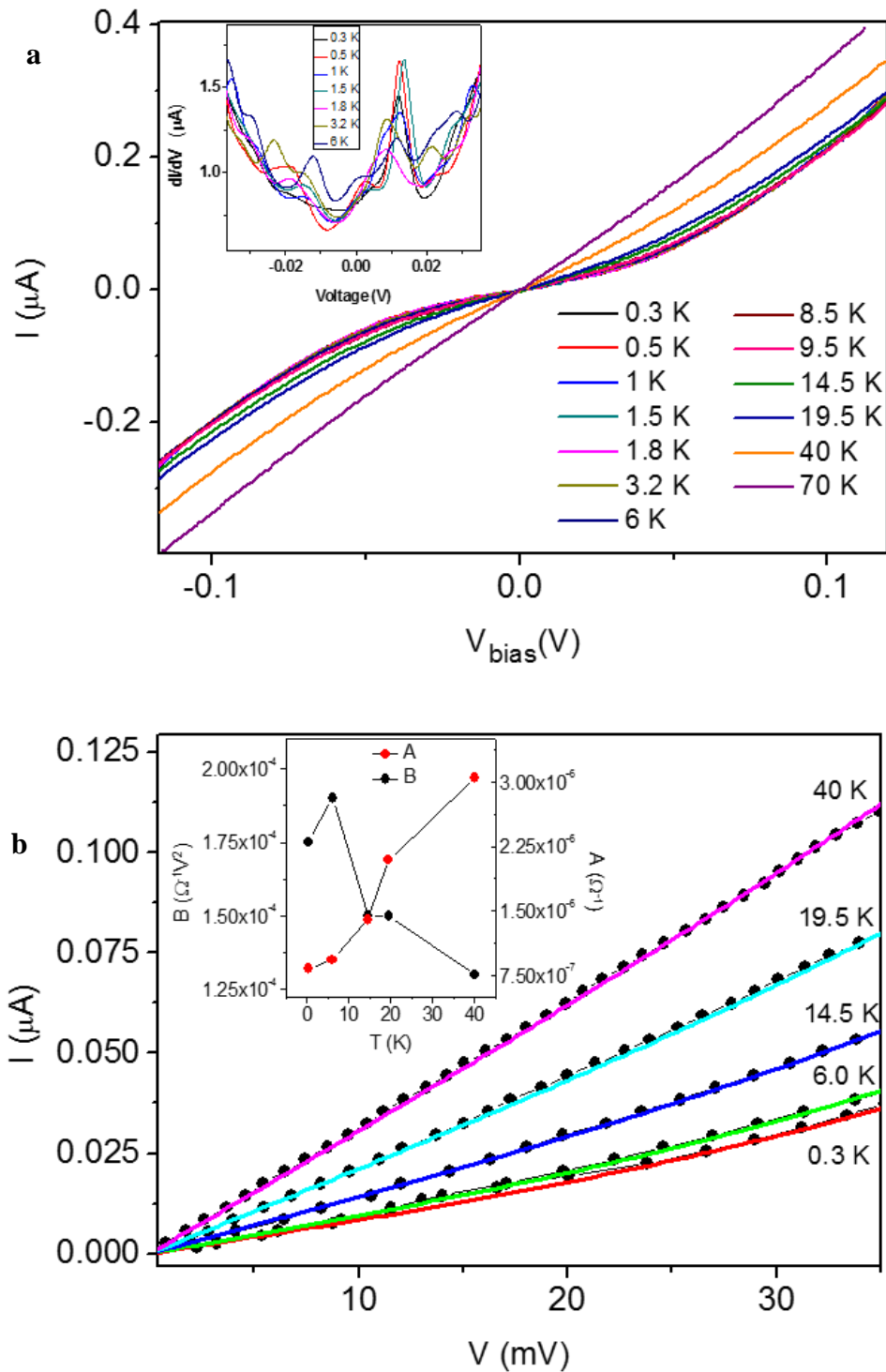
Figure 5-6 (a) The current voltage characteristics of the GdCl$_3$-filled MWNTs network device. There is a clear band gap opening at temperatures below 40 K compared to linear behaviour above that. Differential conductance (inset) shows the formation of temperature dependent resonance peaks. (b) The current voltage plots fitted to equation 5-7. The inset shows the evolution of the coefficients A(co-tunnelling) and B(sequential tunelling) with increasing temperature fitted to equation 5-8.

magnitude as what has been reported for double magnetic tunnel junctions with embedded

superparamagnetic NiFe nanoparticles [39]. E_c is the charging energy which is related to the size and shape and hence the capacitance of the magnetic nanoparticles and can as a first approximation be expressed as $C = 2\pi\varepsilon_0 d$, where ε is the relative permittivity of the tunnelling barriers and d is the diameter of the nanoparticle rod. The Kondo temperature from this fitting is 47 K which is in agreement with the point of inflection in the conductivity temperature curve (figure 5-5(b)) of the GdCl$_3$-filled MWNTs. Thus the *R-T* behaviour is explained as a competition between tunnelling events and the strengthening of the Kondo effect as temperature is lowered, at some point the Kondo effect dominates over the tunnelling (47 K) and change in curvature is observed. In order to verify the co-existence of co-tunneling conductivity in the system an analysis of the current voltage characteristics is undertaken as shown in figure 5-6. The slope of the *I-V* sweeps changes markedly upon lowering temperature and the formation of a gap at temperature below 40 K is observed. As shown in the inset of figure 5-6 (a), the differential conductance exhibits resonance peak features which are temperature dependent (figure 5-7(a)). In order to probe the interaction of sequential and co-tunneling conductivity this work relied on the theory developed for Coulomb gap inelastic co-tunneling [40; 41]:

$$I(V) = \left(\frac{\hbar}{3\pi e^2 R_T^2 E_C^2}\right)\left[(2\pi k_B T)^2 V + e^2 V^3, \right. \tag{5-7}$$

which describes the current as a sum of two terms, one linear and the other cubic in voltage. The *I-V* curves were thus fitted at different temperatures to the phenomenological expression:

$$I(V) = AV + BV^3 \tag{5-8}$$

Here the ratio between the coefficients A and B are related to the strength of contribution, either sequential or co-tunneling, to the current. The fit is shown in figure 5-6 (b) and the trend of the coefficients A and B are shown in the inset as a function of temperature. The change in coefficient A increases at a faster rate than B, this was taken to explain the dominance of co-tunneling over sequential tunnelling in this low current regime [41].
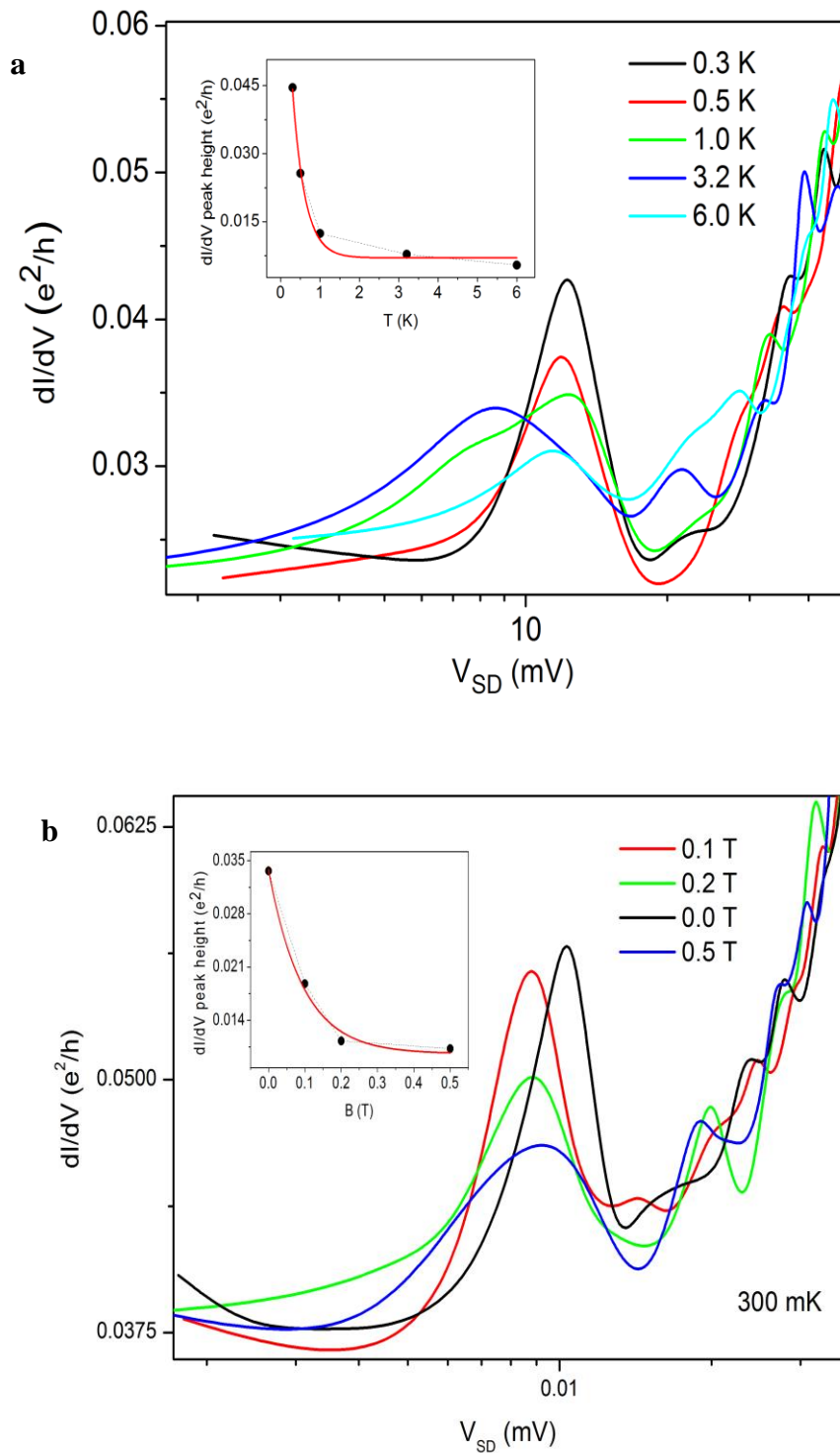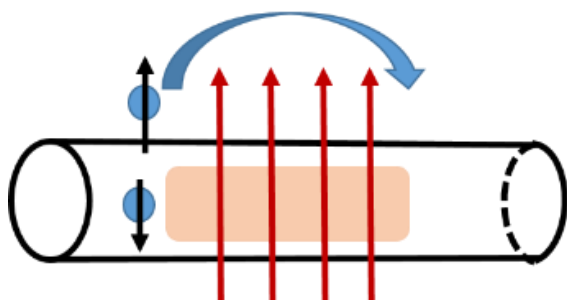
Figure 5-7 Temperature dependence of the differential conductance. The peak heights decrease exponentially as temperature increases and co-tunneling step features are observed along with a spectral shift as temperature increases. (b) magnetic field dependence of the d*I*/d*V* peaks, magnetic field is seen to exponentially suppress the peak intensity.

Sequential tunnelling dominant regime:

T_{K1} Kondo effect between GdCl₃ nanoparticle and incident electron signified by onset of blocking temperature (spin coherence and electron magnetic particle match
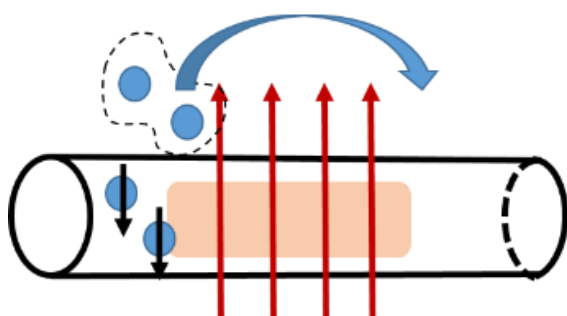
Cotunnelling regime:

As the temperature is lowered co-tunnelling events through formation of virtual states dominates over sequential tunnelling related to collective quasiparticles with preferred combined spin state, Due to spin accumulation from longer spin coherence times of nanomagnet
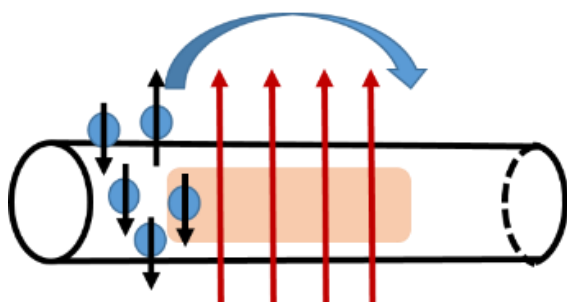
Electron-electron Kondo correlation regime:

As spin accumulation increases Kondo effect between localized electrons can lead to preferential spin configuration for tunnelling

conduction electrons   GdCl₃ nanomagnet

Figure 5-8 A schematic showing the possible mechanisms for the changes observed in the temperature dependent resistance. T_{K1} as determined from the fitting given in figure 5-5 a as well as the onset blocking temperature observed in the susceptibility indicates the Kondo spin-flip event between GdCl₃ and electrons. The middle panel indicates that at lower temperature it is possible to have co-tunneling events which occur through the formation of virtual states. As the switching of the nanoparticles decreases at lower temperatures a stage of maximum spin coherence and thus spin accumulation of electrons is reached. This regime is dominated by electron-electron interactions whereby the Kondo effect allows the correct spin polarization for tunneling to occur also observed as the sharp downturn in susceptibility

Figure 5-9 Log T plot of the RT data showing a change in the conductance mechanism in accordance to what is corresponding to Figure 5-8 and the values calculated in Figure 5-5.
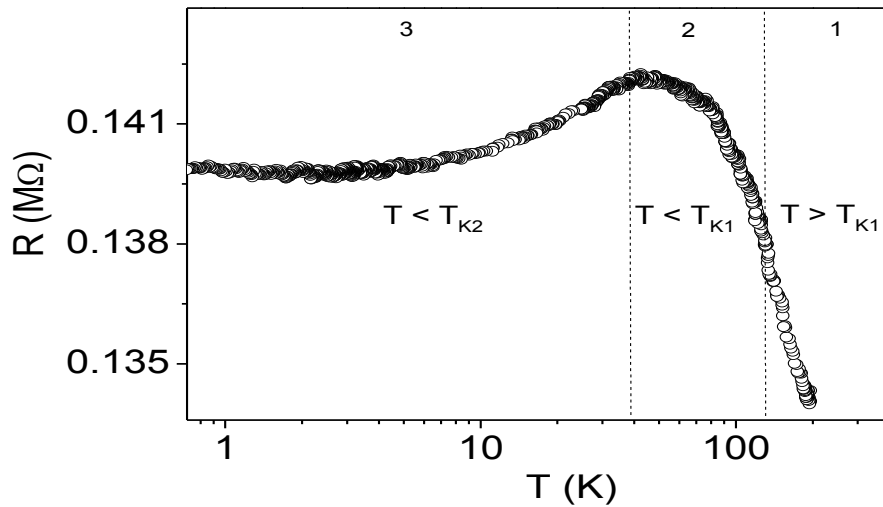
As mentioned previously the differential conductance sweeps exhibit strong resonance peaks at around 10 mV. These peaks are temperature and magnetic field dependent and exponentially decrease in height when increasing either parameter as shown in figure 5-7 (a,b). Upon examining the temperature dependent dI/dV an apparent shifting and broadening of the peaks is observed.

These features can be related back to the competition between co-tunneling and the Kondo effect. As the temperature is increased the Kondo effect is suppressed and co-tunneling is favoured, analogous to the conductance vs temperature. This leads to the formation of co-tunneling peaks at a slightly lower voltage indicated as a shoulder and eventual spectral shift of the Kondo peak. Similar features are observed in the magnetic field dependence (figure 5-7(b). Following conventional analysis the Kondo temperature at zero field and 300 mK is 40 K, determined from the FWHM of the Fano resonance peaks. This value is in excellent agreement with the value obtained from the conductivity fitting and is a significant temperature point as indicated by the susceptibility blocking temperature indicating that spin coherence becomes important for electron correlations.

Figure 5-8 is a schematic showing the possible mechanisms for the changes observed in the temperature dependent resistance. Figure 5-9 is a log T scale plot of the RT data of the GdCl$_3$ filled MWNTs. It can be clearly seen from figure 5-9 that there are diffrrent regimes of

electronic transport governed by the tempertures calculated in figure 5-5. T_{K1} as determined from the fitting given in figure 5-5. as onset of the blocking temperature where sequential tunnelling is dominant. Cotunnelling regime is dominant when, $T_{K2} < T < T_{K1}$ which occurs through the formation of virtual states. At $T < T_{K2}$, where T_{K2} is the Kondo temperature, this regime is dominated by electron-electron interactions whereby the Kondo effect allows the correct spin polarization for tunneling to occur also observed as the sharp downturn in susceptibility.

The magnetic properties of MWNTs filled with $GdCl_3$ are substantially modified which clearly shows the co-existence of Kondo and co-tunnelling effects. The susceptibility measurements indicate an antiferromagnetic exchange interaction, with a bifurcation in susceptibility depending on whether magnetic field is applied or not during cooling, a signature of superparamagnetism. Analysis of the *R-T* data which shows a transition in light of the Kondo effect gives a Kondo temperature of this composite at 40 K. Co-tunneling of conduction electrons interfering with a Kondo type interaction has been verified from the exponential decay of the intensity of the zero bias anomalies conductance peaks which also show strong resonant features observed only in $GdCl_3$ filled MWNT devices as shown in figure 5-7, hence these features are explained in terms of magnetic coherence and spin-flip effects and the competition between the Kondo effect and co-tunneling.

References

1. K. J. Franke, G. Schulze and J. I. Pascual. Science, **332**, 940 (2011).

2. A. Allerdt and A. E. Feiguin. Phys. Rev. B, **95**, 104402 (2017).

3. D. Ciudad, Z.-C. We, A. T. Hindmarch, E. Negusse, D. A. Arena, X.-F. Han and C. H. Marrows. Phys. Rev. B, **85**, 214408 (2012).

4. L. Kouwenhoven and L. Glazman. Physics World, **14**, 33 (2001).

5. G. Falci, D. Feinberg and F. W. J. Hekking. Europhys. Lett., **54,** 255 (2001).

6. J. Barański and T. Domański. Phys. Rev. B, **84**, 195424 (2011).

7. J. S. Lim, R. López and R Aguado. Phys Rev B, **91**, 045441 (2015).

8. A. Mugarza, C. Krull, R. Robles and S. Stepanow. Nat. Commun., **2**, 490 (2011).

9. F. Kuemmeth, H. O. H. Churchill, P. K.Herring and C. M. Marcus. Materials Today, **13**, 18 (2010).

10. L. E. Hueso, J. M. Pruneda, V. Ferrari and G Burnell. arXiv preprint cond-mat/. 0511697 (2005).

11. A. R Rocha, V. M. Garcia-Suarez and S. W. Bailey. Nat. Mater., **4**, 335 (2005).

12. I. Marangon, C. Ménard-Moyon, J. Kolosnjaj-Tabi, M. L. Béoutis, L. Lartigue, D. Alloyeau, E. Pach, B. Ballesteros, G. Autret, T. Ninjbadgar, D. F. Brougham, A. Bianco and F. Gazeau. Adv. Funct. Mater., **73**, 7173 (2014).

13. M. Urdampilleta, S. Klyatskaya, J.-P. Cleuziou, M. Ruben, and W. Wernsdorfer. Nat. Mater., **10**, 502 (2011).

14. R. Kumari. A. Singh, B. S.Yadav, D. R. Mohapatra A. Ghosh, P. Guha, P.V. Satyam, M. K. Singh and P. K. Tyagi. Carbon, **119**, 464 (2017).

15. C. Meyer, C. Morgan and C. M. Schneider. Phys. Status Solidi Basic Res, **248**, 2680 (2011).

16. K. Tsukagoshi, B. W. Alphenaar, and H. Ago. Nature, **401**, 572 (1999).

17. R. Thamankar, S. Niyogi, B. Y. Yoo, Y. W. Rheem, N. V. Myung, R. C. Haddon, and R. K. Kawakamia. Appl. Phys. Lett., **89**, 033119 (2006)

18. P. J-. Herrero, J. Kong, H. S. J. van der Zant, C. Dekker, L. P. Kouwenhoven and S. De Franceschi. Nature, **434**, 484 (2005).

19. T. Inoshita. Science, **281**, 526 (1998).

20. L. Liu, K. Yang, Y. Jiang, B. Song, W. Xiao, L. Li, H. Zhou, Y. Wang, S. Du, M. Ouyang, W. A. Hofer, A. H. C. Neto and H. -J Gao. Sci. Rep., **3**, 1210 (2013).

21. S. Xiang, S. Xiao, K. Fuji, K. Shibuya, T. Endo, N. Yumoto, T. Morimoto, N. Aoki, J. P. Bird and Y. Ochiai. J. Phys: Condens. Matter, **26**, 125304 (2014).

22. T. W Odom, J. L- Huang, C. L. Cheung and C. M. Lieber. Science, **290**, 1549 (2000).

23. F. Tuinstra and J. L. Koenig. J. Chem. Phys, **53**, 1126 (1970).

24. M. V. Kharlamova, A. A. EliseevL. V. Yashina, D. I. Petukhov, C. -P. Liu, C. -Y. Wang, D. A. Semenenko and A. I. Belogorokhov. JETP Letters, **196**, 91 (2010).

25. M. V. Kharlamova, L. V. Yashina, A. A. Eliseev, A. A. Volykhov,V. S. Neudachina, M. M. Brzhezinskaya, T. S. Zyubina, A. V. Lukashin and Yu. D. Tretyakov, Physica Status Solidi B, **249**, 2328 (2012).

26. M. S. Dresselhaus, A. Jorio, M. Hofmann, G. Dresselhaus and R. Saito. Nano Lett., **10**, 751 (2010).

27. F. Tuinstra and J. L. Koenig. J. Chem. Phys., **53**, 1126 (1970).

28. X. Zhao, Y. Ando, L.-C. Qin, H. Kataura, Y. Maniwa and R. Saito. Physica B: Condensed Matter, **323**, 265 (2002).

29. T. Bortolamiol, P. Lukanov, A. -M. Galibert, B. Soula, P. Lonchambon, L. Datas, and E. Flahaut. Carbon, **78**, 79 (2014)

30. A. Jaiswal, R. Das, K. Vivekanand, T. Maity, P. M. Abraham, S. Adyanthaya and P. Poddar. J. Appl. Phys., **107**, 013912 (2010).

31. I. D. Zakir'yanova, A. B. Salyulev and V. a. Khokhlov. Russ. Metall., **83**, 754 (2011).

32. J. F. Daniel, W. R. Wilmarth, G. M. Begun and J. R. Peterson. J. Crystallogr. Spectrosc. Res., **19**, 39 (1989).

33. A. A. Ovchinnikov, V. V. Atrazhev. Phys. Solid State, **40**, 1769 (1998).

34. A. Quetz, I. Dubenko, T. Samanta, H. Vinson, S. Talapatra, N. Ali and S. Stadler, J. Appl. Phys., **13**, 17B512 (2013).

35. P. Nozières. J. Low Temp. Phys., **17**, 31 (1974).

36. J. H. Chen, L. Li, W. G. Cullen, E. D. Williams and M. S. Fuhrer. Nature Phys., **7**, 535 (2011).

37. S. Bhattacharyya and R. McIntosh. Rapid Research Letters, **6,** 56 (2012).

38. D. Ciudad, Z.-C. Wen, A. T. Hindmarch, E. Negusse, D. A. Arena, X-F. Han and C. H. Marrows. Phys. Rev. B, **85**, 214408 (2012).

39. K. J. Dempsey, A. T. Hindmarch, H.-X. Wei, Q.-H. Qin, Z.-C. Wen, W.-X. Wang, G. Vallejo-Fernandez, D. A. Arena, X.-F. Han and C. H. Marrows. Phys. Rev. B, **82**, 214415 (2010).

40. A. Crippa, M. L. V. Tagliaferri, D. Rotta, M. De Michielis, G. Mazzeo, M. Fanciulli, R. Wacquez, M. Vinet and E. Prati. Phys. Rev. B, **92**, 035424 (2015).

41. J. T. Lee, D.-H. Chae, Z. Yao and J. Sessler. Chem. Comm., **48**, 4420 (2012).

6. Transport Gadolinium Chloride Filled Doublewalled Carbon Nanotubes

6.1. Introduction

Double walled carbon nanotubes (DWNTs) consist of two layers of the seamless molecular cylindrical honeycomb graphene structure [1]. They can be regarded as two SWNTs nested one in the other. This unique structure offers the advantages over, SWNT; the outer shell act as protective layer to the inner shell whilst the retaining most of its exceptional properties of MWNT; the fewer number of walls minimizes the effects of defects which are dominant in the multi layers of MWNTs [2]. Hence it is worthwhile to explore the unique properties of these coaxial nanostructures as they offer the possibility to extend the applications of CNTs.

Due to their coaxial nature the resulting electronic properties are complicated as they are influenced by the inter-wall coupling [3] giving rise to non-trivial electronic properties. Generally their electronic transport properties are in the quasi-ballistic regime. Since they consist of two layers of SWNTs which themselves are either semiconducting or metallic [4], hence their inherent electronic properties depend on the chirality selection of the combination of the layers [5, 6]. It has been predicted that poly-chiral DWNTs exhibit metal to semiconductor behaviour due to enhanced inter-tube coupling which determines the long range interaction between the CNTs [7, 8]. Well-aligned DWNTs show diffusive to ballistic electronic transport at low temperatures in contrast to imperfectly aligned DWNTs which show 3D VRH due to enhancement of the intertube interactions [9, 10].

It has been reported that chemical modification of DWNT barely affects its quasi-ballistic charge transport [11] with possibilities of extending their applications. Filled CNTs have demonstrated that these coaxial nanostructures possess unique 1D features due to the protective layer of the outer wall provided to the inner wall [12, 13]. It is therefore very interesting to investigate the transport of modified DWNTs. A brief study on the properties of Gd-filled DWNTs is presented in this chapter. Earlier studies have been done on the electronic transport properties of pristine SWNT [14] and filled MWNTs as well with some shortcomings observed by the author. DWNTs are of interest due to their coaxial nature which make them better candidates for nanoscale engineering. Introducing nanomagnets into their interior is expected to alter their magnetic and electronic properties significantly. The Gd^{3+} ion is known as a key component for the design of paramagnetic complexes as it has the largest number of unpaired

electrons within the rare earth elements [**15**]. Its presence in the CNT is expected to have a direct effect on interwall interaction due to the close proximity of the inner and outer wall. The structural and complimentary magnetic and electronic properties are presented in the subsection that follow. This work is novel as the magnetic and electronic transport properties of DWNTs modified with gadolinium has not been reported before, most studies have focused on either SWNTs or MWNTs [**16**,**17**].
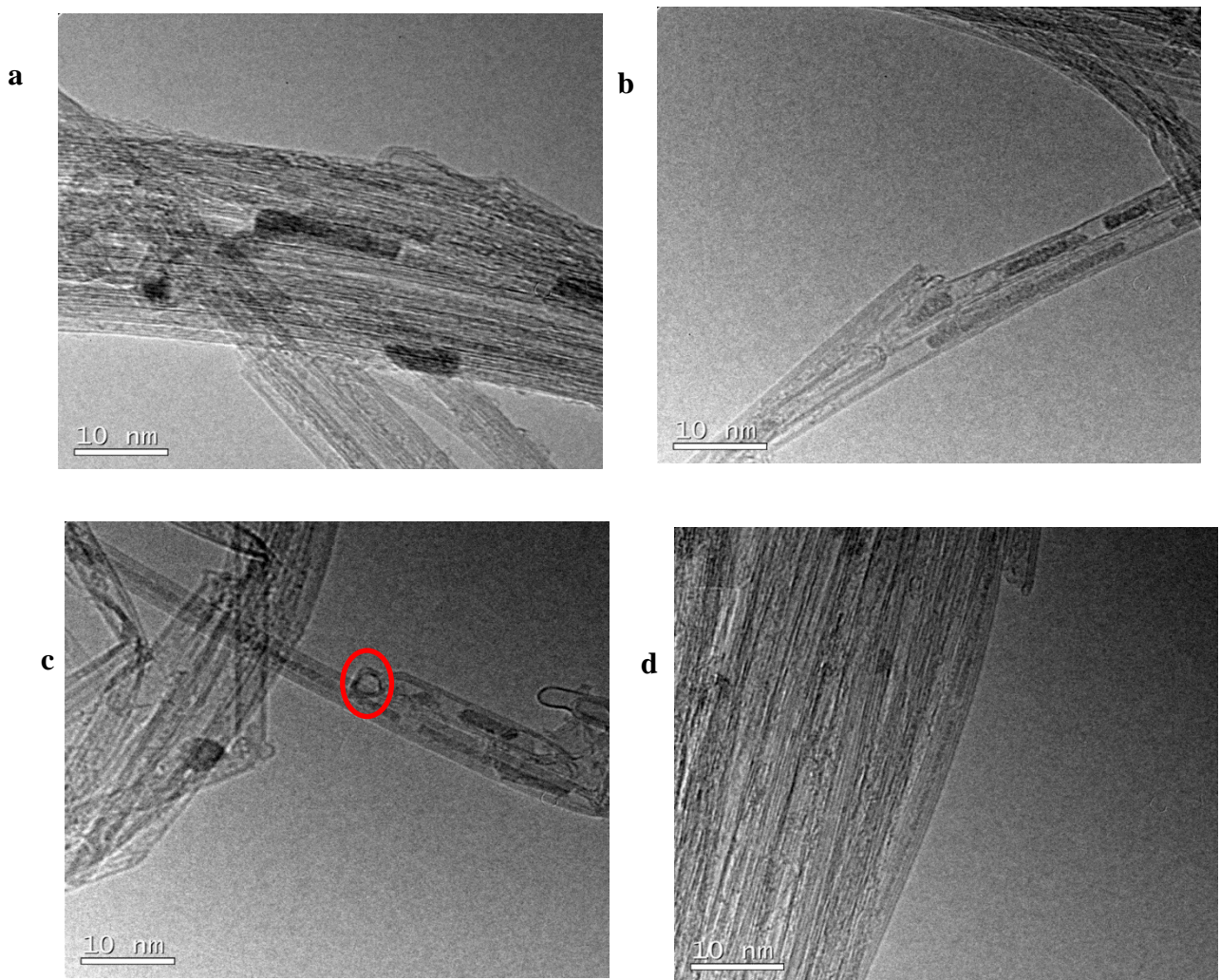
6.2. Structural Characterisation

Figure 6-2 (a)(b)(c)(d) HRTEM images of $GdCl_3$ filled DWNTs showing uniform diameter of randomly filled bundles

The Gd-filled DWNTs were prepared using the method described in section 3.4. The devices were fabricated by DEP, which will be referred to as Gd-filled DWNTs in the subsequent sections, as described in section 3.5 and tested accordingly. HRTEM images in figure 6-1 show bundles gadolinium filled DWNTs. The CNTs are randomly filled with GdCl$_3$ nanorods, figure 6-1(c) & (d) and have discontinuous nanorods along the inner tube (figure 6-1 (a & b)). The coaxial nature of the DWNT can be seen in the HRTEM images, figure 6-1 (c) where there the open end in circled in red. It is also shown that impurities are absent on the exterior of individual CNTs and bundles. ICP-OES indicates the nanocomposite contains 6 weight % of the Gd.

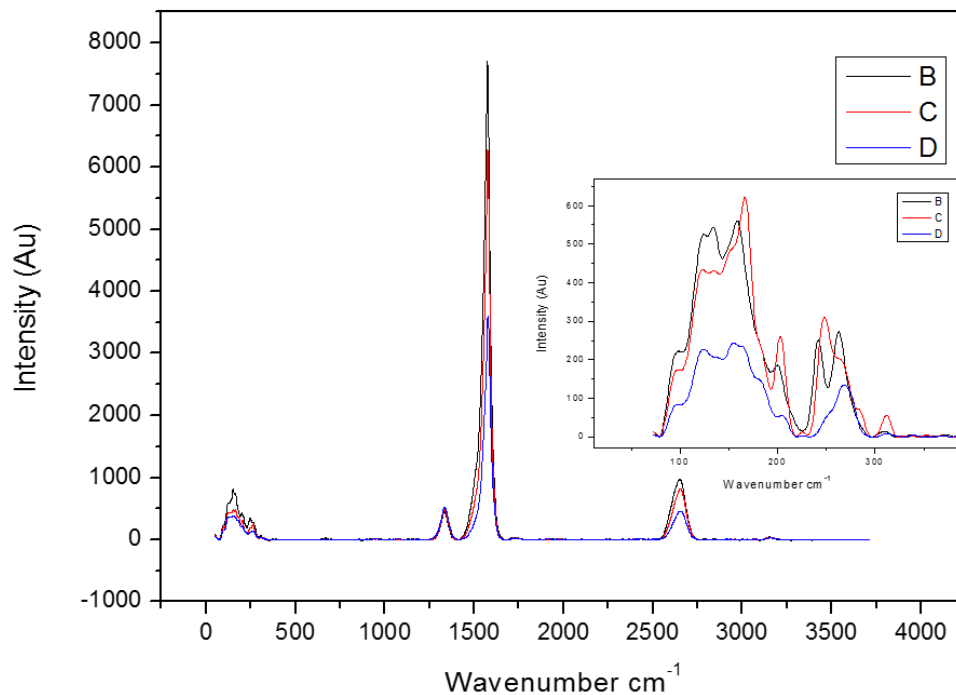## 6.3.   Raman characterization

Figure 6-3 Raman analysis of Gd-filled DWNTs taken from 3 spots B.C.D showing the D and G bands and the D´ and   G´ bands introduced by the disorder. Inset shows the RBM modes

The Raman data for Gd-filled DWNTs are shown in figure 6-2. It is characterized by a low I_D/I_G ratio implying a low level of defects on outer walls. The radial breathing modes (RBM}

resonances shown in the inset within 3 different spots are almost at the same wavenumbers relating to a small diameter distribution. The filling is evident from the HRTEM, but not readily observable in the Raman data. This is mainly due to the fact that generally the peaks for lanthanide chlorides are found within the low wavenumbers and for the DWNTs based composite, this poses a challenge due the presence of RBMs which is an intrinsic property of the material. Hence further investigation is required using a more powerful laser to probe the vibrational modes of this nanocomposite to differentiate the RBM from the vibrational modes of the lanthanide chlorides. Using different excitation wavelengths (a form of Raman Resonance) should give different Raman RBM peak intensity ratios depending on the diameter distribution.

6.4.   Magnetic Properties

The Gd-filled DWNTs show no hysteresis at room temperature with zero remanence and coercivity as shown in figure 6-3. The graph saturates at 5000 Oe. This mainly due the $GdCl_3$ which is known to be paramagnetic as the pristine DWNT are diamagnetic in nature. Temperature dependence studies have to be done as the susceptibility demonstrates there is a superparamagnetic transition at low temperatures.

The molar susceptibility of the Gd-filled DWNTs is measured at 500 Oe from 350 - 2 K and plotted in figure 6-4. The ZFC data shows a gradual increase in the molar susceptibility down to 2 K. The FC data shows a dramatic change in the molar susceptibility. It shows a superparamagnetic transition characteristic of non-interacting magnetic domains. This is a consequence of the filling as previous reports on DWNTs have not observed this effect. The transition to superparamagnetic state occurs at T_B, 30 K with the bifurcation starting at approximately 60 K. This is a result of non-uniform magnetic particle distribution resulting from the filling. The inverse susceptibility, figure 6-4, is also plotted to deduce the exchange mechanism. Using the Curie Weiss law, the effective moment $\mu_{eff} = 18.4 \mu_B$. The Curie Weiss constant, is found by fitting a line on the linear part of the inverse susceptibility curve is 48 K.
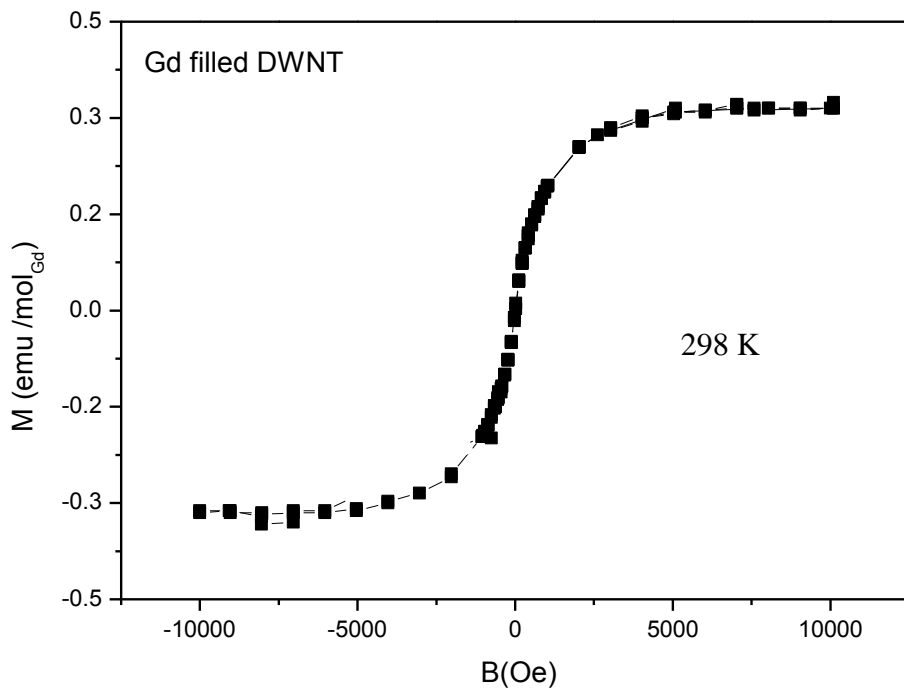
Figure 6-3 Hysteresis of Gd-filled DWNT showing zero remanence and coercivity
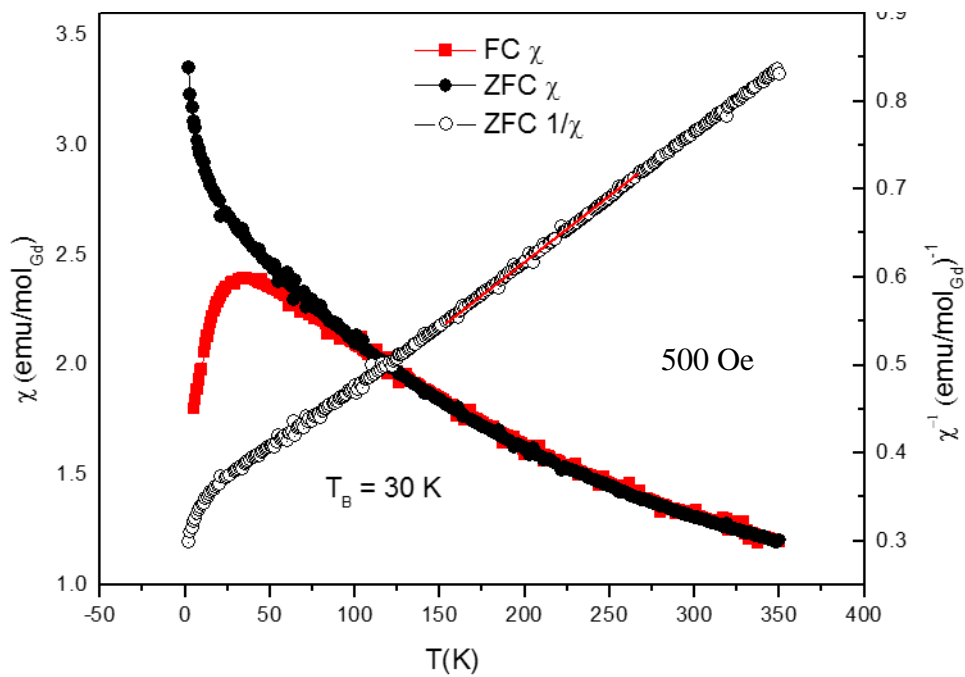

Figure 6-4 Susceptibility and inverse susceptibility plots at 500 Oe for the Gd- filled DWNT showing a superparamagnetic transition in the field cooled data. Inverse susceptibility extrapolates to a negative Weiss temperature typical of antiferromagnetic exchange interaction

6.5. Electronic Transport
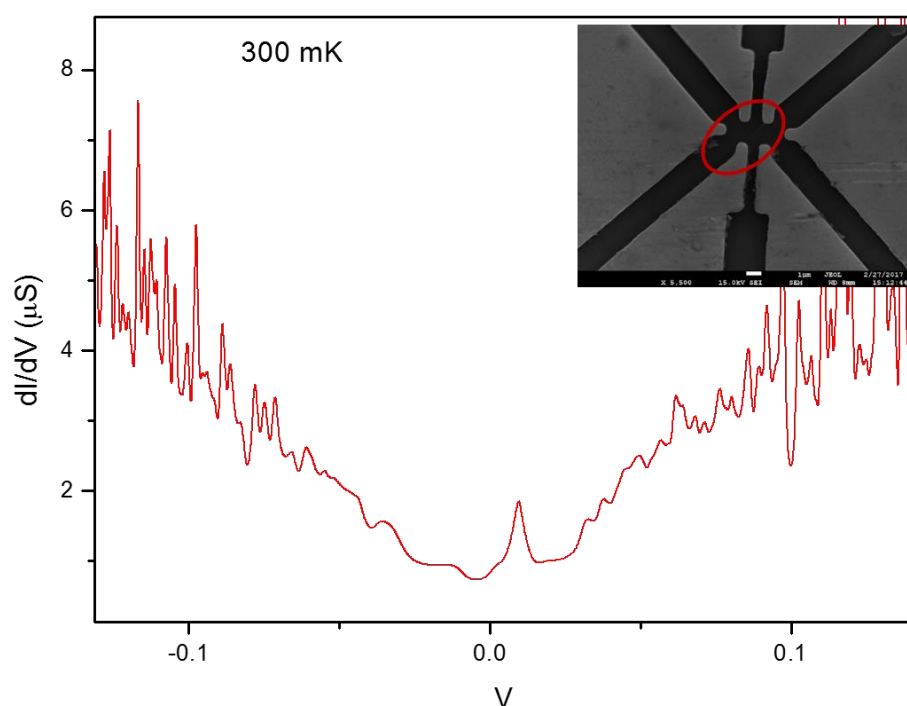
Figure 6-4 dI/dV of Gd-Filled DWNT at 300 mK showing the non-zero bias anomalies which were earlier observed in Gd modified MWNTs

Aligned Gd-filled DWNTs exhibit non-zero bias Kondo like anomalies at 300 mK which have been observed in other Gd-modified CNTs measurements presented in the preceding chapters. Further analysis is required to probe the origin of these resonances in the material. At this point it can be inferred that they are a result of the Gd^{3+} in the nanocomposite. Temperature and magnetic field dependant measurements of the differential conductance have to be performed to probe the mechanism at play in this nanocomposite. It will be very interesting to see what the effect of the fewer walls is in comparison to Gd-filled MWNTs whose transport properties has already been presented in this thesis.

6.6. Future work

The work presented on the GdCl$_3$ filled DWNTs has shown that the nanorods encapsulated in the coaxial nanostructures have very interesting properties. They exhibit superparamagnetism at low temperatures related to the discontinuous filling and they also show Kondo like

resonances around the zero bias anomalies. The features observed are similar to what has been seen for Gd-filled MWNT hence they can be attributed to the modification of the CNT through filling with $GdCl_3$.

Hence it is encouraging to pursue further detailed analysis on this nanocomposite. It should give more superior properties of the nanocomposite as they are "special in a way" due to their coaxial nature. They afford an opportunity to study a system with less defect levels but still possessing quantum transport properties. The introduction of the nanomagnet probably enhances the interwall interaction as well as the inherent electronic properties.

References

1 E. T. Thostenson, Z. Ren and T. W. Chou. Composites science and technology, **61**, 1899 (2001).

2 C. Shen, A. H. Brozenaa and Y. Wang. Nanoscale, **3**, 503 (2011).

3 V. Zolyomi, J. Koltai, A. Rusznyak, J. Kuerti, A. Gali, F. Simon, H. Kuzmany, A. Szabados and R. Surjan. Phys. Rev. B, **77**, 245403 (2008).

4 P. L McEuen, M. S Fuhrer and H. Park. IEEE transactions on nanotechnology, **99**, 78 (2002).

5 S. D. Liang. Phys. B, **352**, 305 (2004).

6 M. Koshino, P. Moon, and Y.-W. Son. Phys. Rev. B, **91**, 035405 (2015).

7 P. Lambin, V. Meunier, and A. Rubio. Phys. Rev. B, **62**, 5129 (2000).

8 M. Koshino, P. Moon. and Y. -W. Son. Phys. Rev. B, **91**, 035405 (2015).

9 C. L. Pint, Y. Q. Xu, E. Morosan and R. H. Hauge. Appl. Phys. Lett., **94**, 182107 (2009).

10 G. Chimowa, E. Flahaut and S. Bhattacharyya. Appl. Phys. Lett., **105**, 173511 (2014).

11 A. Lopez-Bezanilla. J. Phys. Chem. C., **117**, 15266 (2013).

12 G. Chimowa, M. Sendova, E. Flahaut, D. Churochkin and S. Bhattacharyya. J. Appl. Phys., **110**, 123708 (2011).

13 S. Krishnan, H. Yilmaz. R. Vadapoo and C. Marin. Appl. Phys. Lett., **97**, 163107 (2010).

14 S. Ncube, G.Chimowa, Z.Chiguvare, and S. Bhattacharyya. J. Appl. Phys., **116**, 024306 (2014).

15 B. Raduchel, H. Weinmann and A. Muhler. Safety, & Behavior". Encyclopedia of Nuclear Magnetic Resonance, **4**, 216 (2006).

16 B. Sitharaman and L. J Wilson. Int J Nanomedicine, **1**, 291 (2006).

17 B. Sitharaman, B. D. Jacobson, Y. Z. Wadghiri. H. Bryant and J. Frank. J Appl Phys., **113**, 134308 (2013).

7. Discussion

The magnetotransport properties of devices fabricated from carbon nanotubes modified with Gd based complexes are presented in this work. This is the first account of spin transport studies in a mesoscopic bundle of CNTs without ferromagnetic electrodes. The electronic transport is characterized through the measurement of the differential conductance *dI/dV* as function of source drain voltage from devices fabricated from a few bundles of the nanocomposite. The magnetic properties are characterized through susceptibility and hysteresis from SQUID magnetometry measurements. The complementary structural properties resulting from the modification are also characterized using a combination of techniques namely HRTEM, Raman spectroscopy and elemental analysis. This is done to get a statistical average (statistical average since a network was characterised) of the magnetotransport properties of the material which exhibits very interesting behaviour that has not been reported before. It has been demonstrated through the data and analysis presented in this thesis that the electronic transport and magnetic properties of the 1D conductors are influenced by the presence of the Gd nanomagnets introduced either inside or outside a CNT. Hence the 1D hollow nanocylinders present unique model for coupling with nanoscale magnets through functionalization or encapsulation.

Due to the high effective magnetic moment of Gd^{3+}, it is expected that its influence on the CNT electronic properties will be evident. It is noteworthy that in both $GdCl_3$ and Gd-DTPA the gadolinium is in the state Gd^{3+} state, hence the influence of both complexes is comparable for the system studied in this work. In the filled CNT the Gd^{3+} ions are protected from the external environment and hence its magnetic properties are retained. Additionally, in the functionalized sample, the Gd^{3+} would be exposed to the environment if it was just direct functionalization but the presence of the DTPA ligand protects the Gd^{3+}. The only difference is in one system the Gd^{3+} is on the outer walls in the other it's inside the CNT which impacts on the interaction with the conduction electrons, but the overall transport data on these systems is comparable. The difference in behaviour is only seen in the magnetic properties of the nanocomposites and the R-T behaviour which saturates for the Gd functionalized MWNTs at 4 K and shows a maxima at 40 K then decreases as the temperature is lowered. This is probably due to the fact that Gd is on the outer surface on the functionalized and inside the core of the filled. Hence its the interaction with conduction electrons is different as MWNTs are known to conduct through the outermost walls.

This work has successfully demonstrated that covalently functionalizing Gd-DTPA onto MWNT yields a system with a stable interaction between the host material and magnetic nanoclusters. The low temperature electronic transport of the Gd-Fctn-MWNT is characterised by a saturating resistance which can be fitted by the Numerical Renormalization Group formula for a quantum dot. It saturates at low temperatures characteristic of Kondo systems. We have observed an enhanced effective moment and non-superparamagnetic behaviour for the Gd-Fctn MWNTs indicating strong spin interactions. Transport studies indicate a Kondo resonance with Kondo temperature of 91 K. Furthermore, the resonance peaks are asymmetric which have been fitted to the Fano formula indicating interference between discrete states and the conduction continuum. The low field magnetoresistance shows clear switching spin valve behaviour that can be enhanced by applying a lower current. The electronic transport of the nanotubes is controlled by the magnetic states of the aggregated complex grafted onto the surface of the MWNTs. The covalent interactions allow for the effective transfer of the spin states from the magnetic complex to the CNT providing an alternative pathway for the relaxation of the Gd cluster magnetization.

The filling of CNTs have also demonstrated the modification of magnetic properties of MWNTs and DWNTs filled with gadolinium chloride. We observe that the filled MWNTs show signatures of superparamagnetism in the susceptibility measurements with a broad transition from superparamagnetic to blocked state. Transport measurements conducted on network devices showed interesting electron-spin correlations around and below the blocking temperature. The electronic transport was analysed considering a competition between the Kondo effect and co-tunneling following what has been reported for double magnetic tunnel junctions. Resonance peaks were observed in the differential conductance which indicate the crossover between the competing phenomena. This study highlights the potential of carbon based spintronic devices fabricated from MWNTs filled with magnetic material, an avenue that has not yet been investigated in conventional spintronic research.

The elusive Kondo effect is observed in these nanocomposites due to the presence of nanoscale magnetic impurities in a metallic system and the fact that this is not just an ordinary metallic system but a 1D quantum conductor. Hence, we observe spin polarized currents at Fermi level of the metallic conductor that possesses ID quantum transport features. Hence the direct coupling of a nanomagnet to a 1D conductor and the device architecture play a significant role

in the observations reported in this thesis. The network which consists of a few bundles of the modified CNTs gives a statistical average of the electronic transport properties and the associated phenomena. An individual CNT would give an accurate estimation of the electronic properties which can be compromised by sensitivity of the technique employed. Hence within a bundle the Kondo like features are observable which might not be readily accessible for single CNTs using the same device architecture. In a single CNT it requires a more sensitive probing technique like STM to observe the same features. Additionally, for a single CNT in the same device architecture contact resistance overcomes the properties of the material and such distinct features will be obscured and unobservable. The coexistence of the Traditional Kondo and Quantum dot is quite controversial and requires further investigation. It is however worthy to note that these distinct features cannot be ignored and are very intriguing indeed.

In conclusion CNTs were successfully modified with a rare earth element nanomagnets and characterized for their low temperature electronic behaviour and magnetic behaviour as well as their complimentary structural properties. Functionalization and filling with gadolinium derivatives were used as the modification routes. Different techniques were used to characterize the resulting nanocomposites. A detailed functionalization technique has been presented. This work highlights a modification of a quasi-one-dimensional conductor in which carriers cannot circumvent defects or other barriers of conduction. Currently 1-dimensional semiconductors are at the forefront of many interesting scientific developments, most notably topological quantum computing. This works highlights the possibility of tailoring carbon nanotube quantum transport in ways that may find application in this emergent field. The work shows promise for spintronic applications. Spintronics may also enable the leap to quantum computing where units of quantum information known as "qubits" can occupy spin-up and spin-down states simultaneously, and so allow for massive increases in computational power. This study raises a new possibility of tailoring magnetic interactions for quantum transport in carbon nanotube systems that may find application in quantum computing.

.

Appendix A: failure to fit transport data to the variable range hopping model

There are many reports (as referenced in Chapter 4) reporting on variable range hopping being the expected transport mechanism in carbon nanotube films. However, these networks do not fit the VRH mechanism for 1,2 or 3-dimensions as shown in the three figures below. This deviation from expected behavior is most likely due to the functionalization and in the main text we have shown a fit at higher temperatures to the thermal assisted tunneling mechanism and a fit to the numerical renormalized group theory at low temperatures and the saturation point. This highlights the electron correlation effects observed in the material.
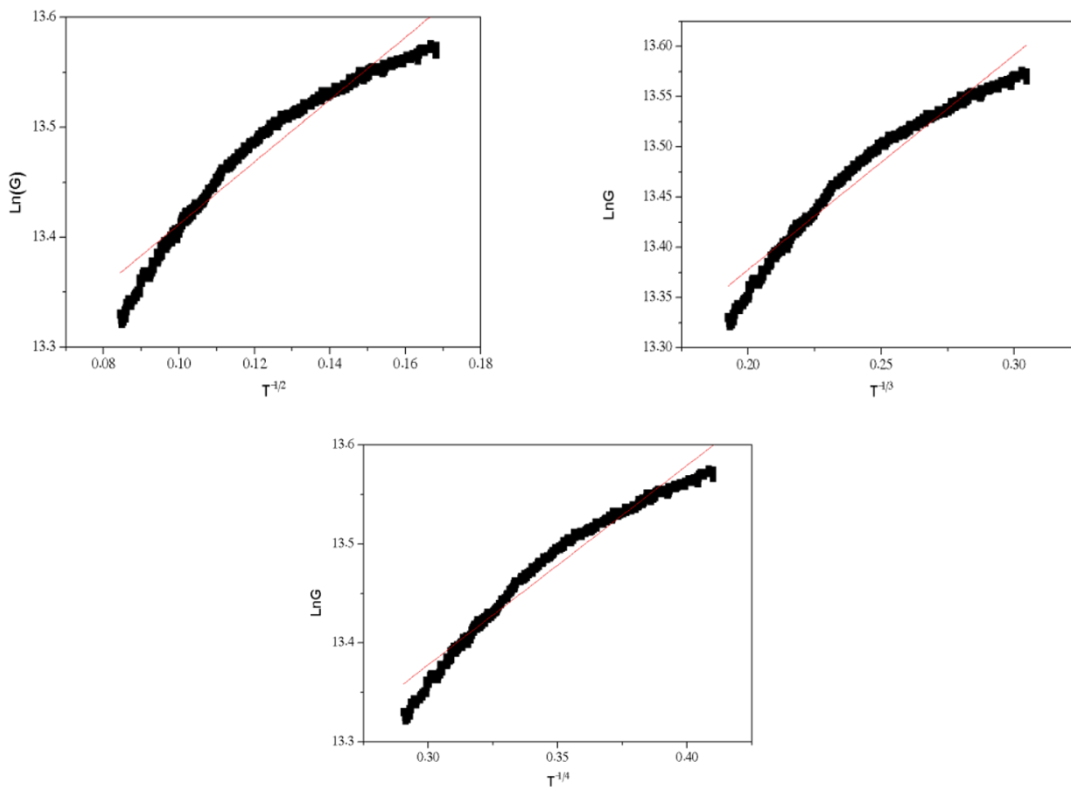
(a) Conductance vs. temperature data for the Gd-Fctn-MWNTs (black line) with variable range hopping model (red line). The data is clearly not a good match to the VRH model for 1-dimensional, (b) 2-dimensional or (c) or 3-dimensional transport.

Appendix B: Susceptibility Plots for pristine MWNTs and Gd-DTPA complex
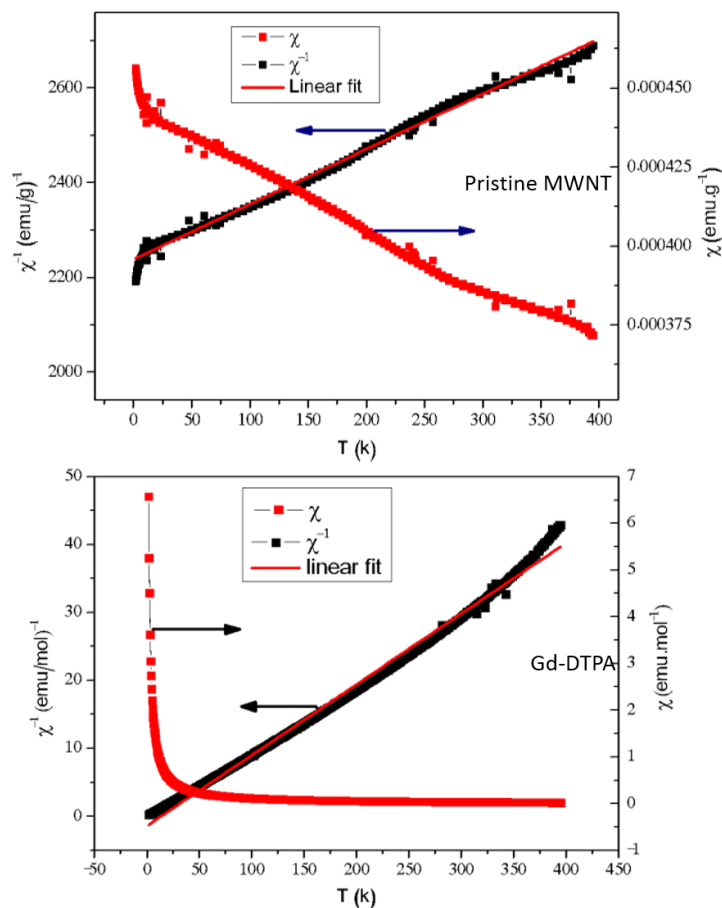
By comparing the results of SQUID magnetometry for the various samples the origin and type of magnetic interaction can be established. As can be seen in figure above, the pristine MWNTs show a very small paramagnetic response as reported in other studies. The effect of these particles are however small when compared to the magnetic response of the Gd functionalized and filled MWNT. In the study the molar susceptibility was used along with the Curie-Weiss law to determine the properties such as the Curie constant and Weiss temperature presented in the thesis. This was done to allow for calculation of the effective moment which requires knowledge of molar concentration of the magnetic species. The Gd-DTPA control clearly showed paramagnetic susceptibility. The effective moment calculated from the inverse susceptibility of the Gd-DTPA was found to be 8.7 μB which is roughly 10 % larger than that of the bare Gd^{3+} ion expected theoretical values. Modification of the Gd effective moment,

both enhancement and reduction, has been observed in Gd-carbon systems. The Increase in moment signifies a ferromagnetic coupling between Gd and DTPA molecule. The Gd-DTPA which is paramagnetic differs significantly from the functionalized Gd-Fctn-MWNT complex as presented in the thesis, this is a strong indication that the resultant interaction observed is due to MWNT-Gd correlations and not dominated exclusively by the Gd-DTPA. This does present some difficulty in determining the effective moment of the respective samples as the susceptibility is presented in terms of number of moles of only the Gd found in each sample. The concentration was determined from the elemental analysis. This means, as stated in the thesis, that the effective moment calculated in this way will lead to an over estimation as it does not take into account the CNT contribution.

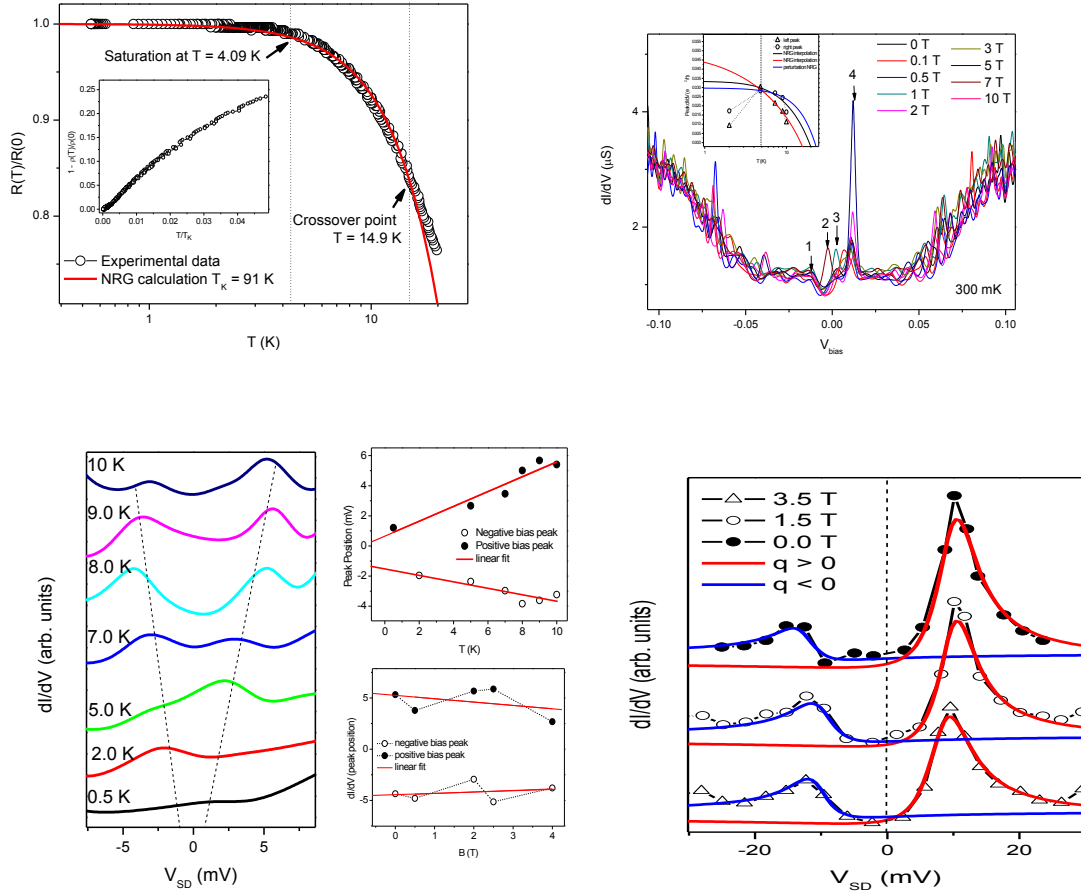# Appendix C: Numerical Renormalization group Fitting

Figure (a) shows the normalized resistance (with respect to the saturation resistance) as a function of temperature. A clear saturation is observed below approximately 4 K. The solid red line is a fit to the numerical renormalization group equation $\frac{R(T)}{R(0)} = \left(1 - c\left(\frac{T}{T_K}\right)^2\right)$, where c =6.088 and T_K is the Kondo temperature. From the fitting T_K= 90 K is extracted although surprisingly high this value is very similar to what has recently been observed in disordered graphene using the same fitting. The inset is a plot to the same data set represented as $(1 - R(T)/R(0))$ $vs.(T/T\_K)^{\wedge}2$ showing the expected fermi liquid behaviour. Additionally it is observed that the equation fits the data set best in the region below 10 K. It was determined that the resistance above 10 follows a thermally activated transport mechanism that broke down below 10 K. This feature is significant due to observation in the differential conductance as shown in figure (b). The dI/dV vs V_{SD} show a gapped region from between -0.05 to 0.05 V. Near the zero bias point resonance like features are observed which have not been observed in

our previous study on pristine MWNTs. These resonance peaks are strongly temperature dependent and only appear in the temperature region below 15 K. The observed peaks fall into two categories based on applied bias. Firstly the peaks located at approximately +/-10 mV are asymmetric and more robust, these peaks are observed at all temperatures below 15 K. Additionally there are two smaller peaks located closer to the zero bias point (+/- 3 mV). These two peaks are fairly symmetric about the zero bias point and do not change position much with application of magnetic field. However, these two peaks shift closer to the zero bias point when lowering temperature and at around 4 K (the saturation point in the resistance temperature curve) only one peak is observed that moves about the zero point (as indicated by figure (c)). At the lowest accessible temperature these two inner peaks are suppressed when compared to the peaks at higher bias. Additionally, as a magnetic field is applied further suppression is possible and arrive at only the two asymmetric peaks at +/-10 mV. The dI/dV peaks heights were traced as temperature is decreased and find that they can be fit (to some degree) by the perturbative renormalized group theory. Here two fittings; were attempted, one that is a $1/Ln(\sqrt{(T^2 + \Gamma)/T_K})$ where the Γ is related to spin relaxation rate. This type of fitting has been used before in single CNT devices showing intrinsic Kondo scattering at very low temperatures. The saturation in dI/dV peak height was reported to be a result of $\Gamma >> T_K$, this is however not observed in the fitting for the Gd-Fctn MWNTs due to much larger Kondo temperature.

The blue line is a fitting to the differential conductance peak height formula given by a term proportional to $[1 - a(\frac{T}{T_K})^2]$ where a is a fitting parameter. The latter model was developed specifically for non-equilibrium Kondo scattering for applied bias that moves the system out of equilibrium. In the fitting the T_K obtained from the resistance temperature NRG fitting was used, finding that both models can be used to explain the result, at least up to some point close to the resistance saturation temperature, this is further verification of Kondo effect causing the resonant features observed. Additionally, the asymmetry in the resonant peaks have lead to investigate the possibility of Fano resonance in this system. Figure d shows the fitting of the Fano formula $\frac{dI}{dV} \sim \frac{(\varepsilon+q)^2}{\varepsilon^2+1}$. Here ε is related to the width and energy of the resonance, q is the Fano parameter which is related to the asymmetry of the peaks. It is found that the Fano formula is a good fit to the 10 mV peaks and have tracked these peaks as a function of applied field. The position and width of the peaks are fairly constant as field is increased up to 3.5 T

but there is a decrease in dI/dV peak height. From the width of the resonance $T_K = 81 - 90$ K, is calculated, in close agreement to the value arrived at through the NRG fitting.

Phenomenology:

There are two mechanisms both a result of the Kondo effect at play here. These two competing phenomena are manifested in the four resonance peaks observed near zero bias in the dI/dV. Firstly there is a robust Fano resonance at +/- 10 mV, the width of these peaks validate the T_K found using the NRG formula. This Fano resonance is likely to be a result of spin polarized, charged islands near the Gd-DTPA complex located on the outer wall of the MWNTs, this discrete state would then interfere with conduction electrons that are propagating along the outer tube or within the first few layers which forms the continuum. The secondary peaks located closer to the zero-bias point are believed to be a split zero bias peak, supported by the temperature dependence. The splitting of the zero-bias peak is related to the singlet-triplet conversion which occurs spontaneously in the material due to the localized spin induced by Gd-DTPA. Differential conductance is strongly related to the DOS, and the four peaks are related through the conduction electrons, when some of the peaks are suppressed by either temperature or field the find the remaining peaks are more robust.

References:

Numerical RG fitting

- T. A. Costi, and A. C. Hewson, J. Phys.: Condens. Matter 5 (1993)

- J.-H. Chen, Liang Li, W. G. Cullen, E. D. Williams, and M. Fuhrer, Nature Phys. 7, 2011

Perturbative RG fitting

- A. Rosch, J. Paaske, J. Kroha, P. Wolfle, J. Phys. Soc. Jpn. 74, 118 (2005)

- A. Kaminski, Y. V. Nazarov, L. I. Glazman, Phys. Rev. B. 62, 12 (2000)

- J. Paaske, A. Rosch, P. Wolfle, N. Mason, C. M. Marcus, and J. Nygard, Nature Phys. (2006)

Fano resonance

- K. Hong, and W. Y. Kim, Angewandte chemie, 125, (2013)

- B. Babic, and C. Shonenberger, Phys. Rev. B. 70, 195408 (2004)

- T. W. Odom, J.-L. Haung, C. L. Cheung, C. M. Lieber, Science, 290, (2000)

Appendix D: Additional characterization for Gd Filled MWNT
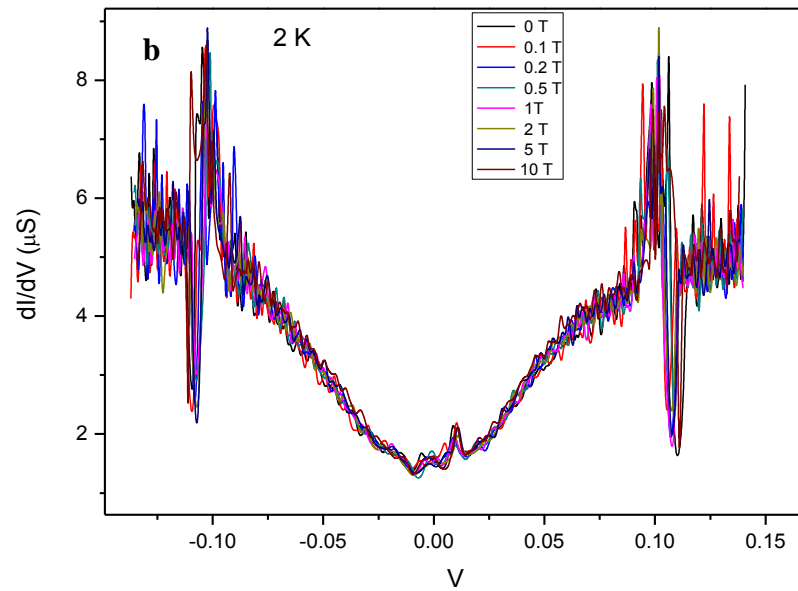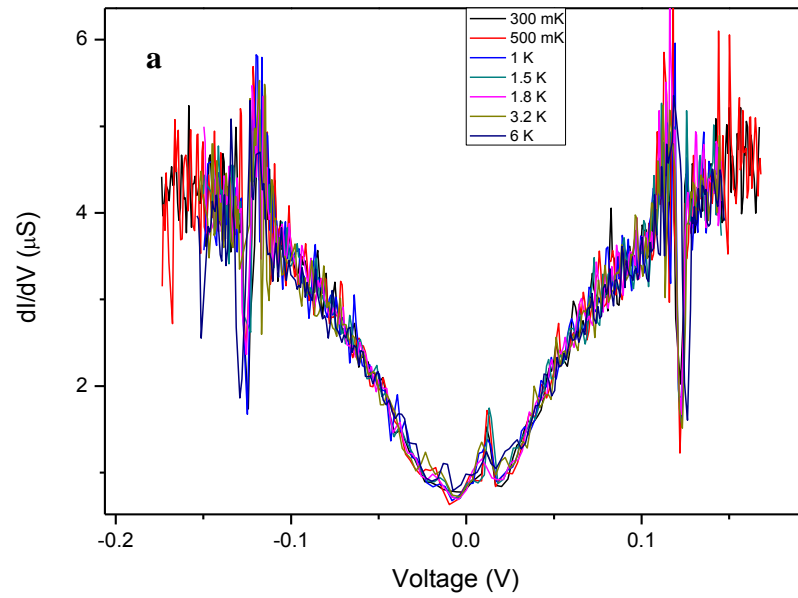
At different temperatures ranging from 300 mK to 6 K the Kondo and like resonances are visible and become indistinct (noisy) as the temperature is increased as shown in (a). At 2 K and different magnetic field the Kondo like resonances are clearly visible which shows that this temperature is within the Kondo regime before the thermal effects become too strong.

7.1. Contributions

Conference Presentations and workshops

- Oral Presentation at the SAIP 57th conference 2012, University of Pretoria, Pretoria, South Africa.

- Poster presentation at the DST-NRF Centre of Excellence in Strong Materials workshop 2012, University of the Witwatersrand, Johannesburg, South Africa.

- Poster Presentation 3rd Cross Faculty Graduate Symposium, University of the Witwatersrand 2013, Johannesburg, South Africa

- Oral Presentation at the SAIP 58th conference 2013, University of Zululand, Richards Bay, South Africa.

- Poster presentation at the DST-NRF Centre of Excellence in Strong Materials workshop 2013, University of the Witwatersrand, Johannesburg, South Africa.

- Oral presentation 1st International Workshop in NanoCarbon 2013, University of the Witwatersrand, Johannesburg, South Africa

- Poster Presentation 4th Cross Faculty Graduate Symposium, University of the Witwatersrand 2014, Johannesburg, South Africa

- Poster presentation at the DST-NRF Centre of Excellence in Strong Materials workshop 2015, University of the Witwatersrand, Johannesburg, South Africa

- Oral Presentation 3rd International Workshop in NanoCarbon 2016, University of the Witwatersrand, Johannesburg, South Africa

- Poster presentation at the DST-NRF Centre of Excellence in Strong Materials workshop 2016, University of the Witwatersrand, Johannesburg, South Africa

- Fourth Conference on Sensors, MEMS, and Electro-Optic Systems, 2016, Skukuza, Kruger National Park, South Africa

- Poster presentation, DST-NRF Nanotechnology Symposium 2016, CSIR Convention Centre, Pretoria, South Africa

- Poster presentation at the DST-NRF Centre of Excellence in Strong Materials workshop 2017, University of the Witwatersrand, Johannesburg, South Africa

- Oral presentation, Low-dimensional nanomaterials Workshop, 2017, River Club, Liesbeek Parkway, Observatory, Cape Town South Africa

- Oral Presentation at the SAIP 62nd conference 2017, Stellenbosch University Stellenbosch, South Africa

Publication List

- <u>Siphephile Ncube</u>, George Chimowa, Zivayi Chiguvare, and Somnath Bhattacharyya, **Realizing one-dimensional quantum and high-frequency transport features in aligned single-walled carbon nanotube ropes**, Journal of Applied Physics **116**, 024306 (2014)

- George Chimowa, <u>Siphephile Ncube,</u> Somnath Bhattacharyya. (2015) **Observation of impedance oscillations in single-walled carbon nanotube bundles excited by high-frequency signals.** EPL (Europhysics Letters) **111**:3, 36001 (2015)

- Davie Mtsuko, Tahir Aslan, <u>Siphephile Ncube</u>, Christopher Coleman, Daniel Wamwangi and Somnath Bhattacharyya **Observation of Aharonov-Bohm and Al'tshuler-Aronov-Spivak oscillations in the background of universal conductance fluctuations in silicon nanowires** EPL (Europhysics Letters), Volume **113**, 4 (2016)

- <u>Siphephile Ncube</u>, Amy Naicker, Christopher Coleman, Alvaro de Sousa, Emmanuel Flahaut, Andre Strydom and Somnath Bhattacharyya; **Low temperature magneto transport features of rare earth element functionalized carbon nanotube network devices for spintronic applications** Proceedings Volume 10036, Fourth Conference on Sensors, MEMS, and Electro-Optic Systems;1003607 (2017); doi: 10.1117/12.2245405

- C. Coleman, S. Khorasani, <u>S. Ncube</u>, D. Mtsuko, C. Botha, C. Sandrock, M. Fernandes, D. Levendis and S. Bhattacharyya **Nanomanipulation device fabrication: multilayerd graphene and OFET devices** Proceedings Volume 10036, Fourth Conference on Sensors, MEMS, and Electro-Optic Systems;1003608 (2017); doi: 10.1117/12.2245446

- <u>S. Ncube</u>, C. Coleman, A. Strydom, E. Flahaut, A. de Sousa, S. Bhattacharyya **Kondo effect and enhanced magnetic properties in gadolinium functionalized carbon nanotube supramolecular complex**. Scientific Reports **8**, 8057 (2018) doi:10.1038/s41598-018-26428-y

- <u>S. Ncube,</u> C. Coleman, C. Nie, P. Lonchambon, A. Strydom, E. Flahaut, A. de Sousa, S. Bhattacharyya **Observation of strong Kondo like features and co-tunnelling in superparamagnetic GdCl$_3$ filled 1D nanomagnets**. Journal of Applied Physics **123**, 213901 (2018) doi.org/10.1063/1.5024346.